ABSTRACT

Title of Document:
KELVIN PROBE MICROSCOPY STUDIES OF EPITAXIAL GRAPHENE ON SiC(0001).

Alexandra Elizabeth Curtin, PhD., 2011

Directed By:
Professor Michael S. Fuhrer, Department of Physics, Center for Nanophysics and Advanced Materials (Director) and the Materials Research Science and Engineering Center.

Epitaxial graphene on SiC(0001) presents a promising platform for device applications and fundamental investigations. Graphene growth on SiC(0001) can produce consistent monolayer thickness on terraces and good electronic properties. In exfoliated graphene on SiO_2, random charged impurities in the SiO_2 surface are thought to be the dominant scatterers, explaining the observed transport properties as well as the spatial charge inhomogeneity seen in scanned-probe experiments. In contrast, the scattering mechanisms and charge distribution in epitaxial graphene remain relatively unexplored.

Here I use Kelvin probe microscopy (KPM) in ambient and UHV conditions to directly measure the surface potential of epitaxial graphene on SiC(0001). Ambient-environment KPM on graphene/SiC(0001) shows surface potential variations of only 12 meV. Taken together with transport measurements, the data

suggest that the graphene samples in ambient are in the low-doped regime, near the minimum conductivity of $\approx 4e^2/h$.

I am also able to use UHV KPM of graphene/ SiC(0001) to identify the discrete surface potentials of monolayer and bilayer graphene as well as the insulating interfacial carbon layer and bare SiC, correlated with scanning electron micrographs of the same location. The surface potential differences between monolayer and bilayer graphene and between IFL and monolayer graphene are both suggestive of low doping ($\leq 10^{12}$ cm^{-2}). The surface potentials of monolayer and bilayer graphene are relatively smooth, while the IFL and bare SiC, in contrast, showed larger variations in surface potential suggesting the presence of unscreened charged impurities present on the IFL that are later screened by the overgrown graphene. I model the potential variations for unscreened and graphene-screened charged impurities using the self-consistent theory of graphene developed by Adam et al. The results show that although surface potential variations are, as expected, larger in the IFL than in graphene, both surfaces display surface potential variations 10-40 times smaller than predicted by theory. While ambient electronic transport data and surface potential steps suggest our samples are only lightly doped ($\leq 10^{12}$ cm^{-2}), in a regime dominated by electron-hole puddles, we do not observe these puddles in UHV. The absence of puddles in UHV leaves the source of doping in these samples an open question.

KELVIN PROBE MICROSCOPY STUDIES OF EPITAXIAL GRAPHENE ON
SiC(0001)

By

Alexandra Elizabeth Curtin

Dissertation submitted to the Faculty of the Graduate School of the
University of Maryland, College Park, in partial fulfillment
of the requirements for the degree of
Doctor of Philosophy
2011

Advisory Committee:
Professor Michael S. Fuhrer, Chair
Dr. William G. Cullen
Dr. D. Kurt Gaskill
Professor Christopher Lobb
Professor John Melngailis

Preface

This dissertation represents four years of work performed under the guidance of Dr. Michael Fuhrer in the physics department of the University of Maryland in College Park. Although my first year of graduate school took place in State College, PA, I returned to Maryland in 2007 for the research portion of my graduate career. While in Dr. Fuhrer's group, I was funded by the Material Research Science and Engineering Center and had the opportunity to collaborate with and receive my samples from the Gaskill group at the Naval Research Laboratory.

The work presented here uses Kelvin probe microscopy to provide insight into the charge distribution environment of epitaxial graphene samples. Chapter 1 introduces the band structure of graphite and graphene monolayers. Charge transport in exfoliated graphene devices is discussed from experimental and theoretical perspectives, outlining the self-consistent theory of charged impurity scattering. Further experimental support of the charged impurity scattering model is presented as evidence of the formation of electron-hole puddles. Chapter 2 presents the experimental methods of atomic force microscopy and Kelvin probe microscopy used in this work. Chapter 3 outlines four methods of fabricating graphene films, with a focus on epitaxial growth on SiC. Chapters 4, 5, and 6 discuss Kelvin probe data collected on epitaxial graphene samples grown on SiC(0001). Specifically, Chapter 4 presents ambient data showing carrier concentration variation over $(10 \ \mu m)^2$ sample regions. Chapter 5 focuses on capability of the Kelvin probe technique to distinguish between graphene layers. I return to the question of charge distribution in Chapter 6 as measured by UHV Kelvin probe microscopy. The predicted electron-hole puddles

are not observed in the UHV data, suggesting that the charged impurities of the self-consistent theory may not be at the graphene/substrate interface as previously thought.

Dedication

To my mother, Madelyn Elaine Curtin, for daily moral support, endless phone calls,

some serious editing chops, and the drive to see this through to the end.

Acknowledgments

There are many people I would like to thank for helping me complete this work and finish my PhD here at Maryland. First and foremost, I am grateful to my advisor, Michael Fuhrer, for hiring me not just once, but twice, first as an undergraduate and later after I completed my first year of graduate work at Pennsylvania State University. Michael has always looked out for my best interests, helping me chart my way through graduate school. He has given me many opportunities for collaboration, not least of which was the opportunity to collaborate with the Naval Research Laboratories on their studies of epitaxial graphene. I have always felt that I had his support, whether it was on a scientific question or a major equipment repair.

Second in this list, I thank my family. I have realized that having two parents who went through graduate school is something of a rare luxury. With every twist and turn of the past five years, they have been there to support me, to understand what graduate school was all about, and to give me a nudge in the right direction. I am thankful to Nate Clark for all the moral support and bike rides. I especially thank Betsy Pugel for mentoring me. Our many weekend breakfast conversations about work, school, and life gave me guidance when I needed it and many laughs along the way.

I would like to thank my research group, especially Sungjae Cho, for being a great labmate, and Dan Lenski for mentoring me as an undergraduate. I would also like to include a special note to Kristen Burson. She was my first REU student, and it has been a pleasure to watch her thrive as a graduate student in our group.

Dr. Bill Cullen deserves a special thank you all his own for the many, many hours spent training me and helping me tame the UHV JEOL system. He has been infinitely patient with me and, in turn, has taught me the value of being infinitely patient with cantankerous microscopes. I also thank Kurt Gaskill and John Melngailis, not only for being on my committee but also for putting exciting new projects on my path through school. Finally, I am grateful to the committee as a whole. Thank you all for taking the time to read my thesis and sit on my committee. I could not have asked for a better group.

Table of Contents

List of Figures

Chapter 1: An Introduction to Graphene Theory

Introduction

Graphene is a single atomic layer of carbon atoms arranged in a honeycomb lattice and may be thought of as a single atomic plane of graphite. Recently, graphene has generated a lot of interest as a truly two-dimensional (2D) material and for its massless dispersion relation for charge carriers.[1]

As the experimental body of work on graphene has grown over the past six years, obstacles remain relating to the fabrication of clean, undoped, large-scale graphene samples. Small samples of graphene exfoliated from graphite onto SiO_2 substrates have received the most attention in transport experiments, which have probed the effects of charged impurities, substrate effects and environmental dopants. The experiments point to a model of graphene on SiO_2 in which transport is governed to a large extent by charged-impurity scattering due to trapped charges in the SiO_2 substrate.[2] The impurity potential of random charged impurities also induces electron and hole puddles in net-charge-neutral graphene, resulting in an inhomogeneous charge distribution throughout the material[3], [4] with a characteristic length scale of a single charge puddle ($\approx$20 nm).[2]

The future of graphene in industry relies on the success of large-scale growth of graphene. Among methods for growing large-area graphene, epitaxial growth on the Si-face of SiC has emerged as a means of consistently producing continuous monolayer growth. While the wafer-scale growth is promising for device

applications, much remains to be learned about how the epitaxial growth process affects the doping and transport properties of devices made from these films.

Scanning tunneling spectroscopy (STS) and scanning single-electron transistor (SSET) measurements of exfoliated graphene on SiO_2 are consistent with the puddle theory.[3-5] However, these methods are limited in length-scale to tens of nanometers, frequently only imaging a single puddle.[4] As I began work on this thesis, transport measurements on graphene on SiC had indicated, in contrast, large variation in carrier concentration in samples over much larger areas (tens of micrometers).[5] At this time scanned probe studies of charge inhomogeneity had not yet been performed on epitaxial graphene on SiC.

The work presented here investigates the charge inhomogeneity of graphene on silicon-face SiC and the underlying carbon-rich interfacial layer (IFL) of the SiC substrate using scanning Kelvin probe microscopy under ambient and ultra-high vacuum (UHV) conditions, and over length scales ranging from millimeters to nanometers. The beginning of this chapter (Chapter 1) will introduce the atomic and electronic structure of graphene. Chapter 1 will then briefly describe the various methods for fabricating graphene explored by experimental groups to date, before focusing on the epitaxial growth of graphene films by silicon sublimation from SiC substrates. Chapter 1 will next review the current theoretical and experimental understanding of charge transport in graphene in the presence of random charged-impurity potential. Chapter 2 will outline the experimental techniques used to collect the surface potential data presented in chapters 3, 4, and 5. The precise details of graphene growth will be outlined for the samples used in the work, and the principles

of Kelvin probe microscopy will be discussed in detail. Chapter 3 will detail Kelvin probe data collected under ambient conditions sampling widely-separated areas of a sample of graphene on Si-face SiC and relate these measurements to previously collected electron transport data. The results indicate a much more uniform carrier density in graphene on Si-face SiC than previously thought, and the transport measurements are reinterpreted in this light. Chapters 4 and 5 extend the Kelvin probe technique to study graphene on Si-face SiC in UHV at higher spatial resolution. Chapter 4 will demonstrate that both KPM performed under ambient and UHV conditions differentiates between monolayer and bilayer graphene as well as two distinct IFLs. The results corroborate scanning electron microscopy (SEM) and Raman spectroscopy data from my collaborators at the Naval Research Laboratory. Chapter 5 will explore the nature of microscopic surface potential variation within the graphene monolayer on Si-face SiC and how this variation relates to charge puddling and the charge environment in the SiC substrate and IFL.

Graphene Atomic Structure and Electronic Properties

Figure 1 shows the atomic structure of graphene. The unit cell of graphene has two atoms arranged on a trigonal lattice. This honeycomb structure appears also in the planes of graphite and in rolled up form as carbon nanotubes. The electronic structure of graphene was studied theoretically as early as 1947 by Wallace.[6] The band structure was calculated for a single layer of carbon atoms in a hexagonal lattice and expanded to apply to the stacked configuration of graphite. Wallace performed a tight-binding calculation for the carbon π-orbitals including nearest-neighbor overlap, γ_0, and next-nearest-neighbor overlap, γ_1. The eigenvalue is

3

$$\begin{pmatrix} H_{11} - ES & H_{12} \\ H_{21} & H_{22} - ES \end{pmatrix} = 0. \tag{1.1}$$

From Wallace, $S = N$, the number of unit cells.[6] Using the symmetry of the crystal, one can reduce the number of matrix elements labeled in equation 1.1 and write

$$H_{12}^{'} = \frac{1}{N} H_{12} \qquad H_{11}^{'} = \frac{1}{N} H_{11} \quad \text{and}$$
$$E = H_{11}^{'} \pm \left| H_{12}^{'} \right| \tag{1.2)[6]}$$

where

$$H_{11}^{'}(k) = E_0 - 2\gamma_0^{'} \left[\cos 2\pi k_y a + 2\cos\left(\pi k_x a\sqrt{3}\right)\cos\left(\pi k_y a\right) \right]$$
$$H_{12}^{'}(k) = -\gamma_0 \left(e^{-2\pi i k_z a/\sqrt{3}} + 2\cos\left(\pi k_y a\right)e^{2\pi i k_z a/2\sqrt{3}} \right) \tag{1.3)[6]}$$
$$\left| H_{12}^{'}(k) \right|^2 = \gamma_0^2 \left(1 + 4\cos\left(\frac{\sqrt{3}k_x a}{2}\right)\cos\left(\frac{k_y a}{2}\right) + 4\cos^2\left(\frac{k_y a}{2}\right) \right).$$

The interaction of the nearest neighbors, atoms A and B, is given by γ_0.

$$\gamma_0 = \int X^*(r - \rho_{AB})(U - V)X(r)dr \tag{1.4)[6]}$$

and the interaction of nearest neighbors among only the atoms of a single type, A, is given by γ_0' to be

$$\gamma_0^{'} = \int X^*(r - \rho')(U - V)X(r)dr \tag{1.5)[6]}$$

Here U is the potential of the isolated atom and V is the potential of the lattice. $X(r)$ is the $2p_z$ wave function for a single carbon atom. Taking only the nearest neighbor interactions, one obtains the following expression for the band structure:

$$E(k) = E_0 \pm \gamma_0 \sqrt{1 + 4\cos\left(\frac{\sqrt{3}k_x a}{2}\right)\cos\left(\frac{k_y a}{2}\right) + 4\cos^2\left(\frac{k_y a}{2}\right)}$$
$$\tag{1.6}$$

4
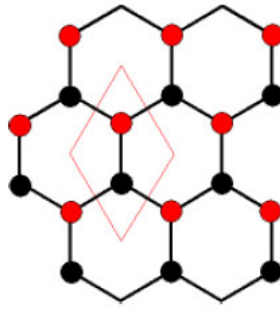
Figure 1: Graphene unit cell
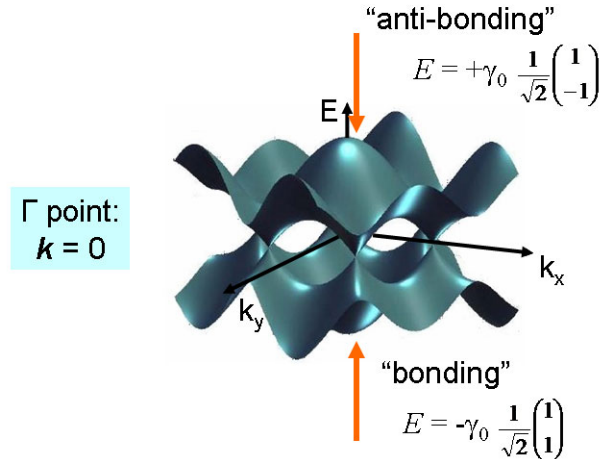
Figure 2: Band structure of graphene. Figure courtesy of Michael Fuhrer.

Figure 2 shows the dispersion of the π-bands given by equation 1.6 There are two bands that may be thought of as having bonding and anti-bonding character. The corners of the first Brillouin zone of the two-dimensional hexagonal lattice are denoted K in the usual notation for high symmetry points. There are two distinguishable K points, which I will denote K and K'. The bonding and anti-bonding bands touch at the K points in the Brillouin zone.[7]

Returning to the single layer, at low energy, a **k·p** expansion around the K point in momentum gives the Hamiltonian [8]

$$H_K = v\sigma \bullet k = v \begin{pmatrix} 0 & k_x - ik_y \\ k_x + ik_y & 0 \end{pmatrix}, \tag{1.7}$$

with the corresponding Hamiltonian at K' given by [8]

$$H_{K'} = \hbar v \sigma^\dagger \bullet k \tag{1.8}$$

where $v = \dfrac{\sqrt{3}\gamma_0 a}{2}$ is the Fermi velocity, $\hbar$ is Planck's constant, and $\boldsymbol{\sigma}$ are the Pauli

matrices. The Hamiltonians operate on a two-component vector wavefunction, where

the two components represent the magnitude and phase of the π-orbital on each atom

in the two-atom unit cell. The eigenvectors, $\boldsymbol{k}$, are [7-9]

$$|k, \pm\rangle = \left(|k, A\rangle \pm e^{i\varphi} |k, B\rangle\right) \tag{1.9}$$

where $\varphi \equiv \tan^{-1}(k_x/k_y)$ and A and B now denote the two distinct atoms in the unit cell.

The eigenvalues are

$$E_{k,\pm} = \pm v \, |k|. \tag{1.10}$$

Equation 2.7 is similar to the Dirac equation for massless relativistic particles.

In graphene, the role of the electron spin is played by the direction of the two-

component wavefunction, which is termed the pseudospin. The pseudospin is

coupled to momentum and points parallel to $\boldsymbol{k}$ around the K point and antiparallel to $\boldsymbol{k}$

at the K' point. (The real electron spin in graphene is considered to be uncoupled to

orbital motion since there is little spin-orbit coupling in carbon).[10] The pseudospin

ensures that electrons with opposite momenta about a given K point are orthogonal

and therefore backscattering is forbidden for long wavelength perturbations.[7]

As a side note, the band structure of graphene above also forms the basis for

understanding carbon nanotubes. The electronic band structure of carbon nanotubes

is constrained by the periodic boundary conditions imposed by wrapping the honeycomb lattice around the circumference of the nanotube. The wrapping angle and number of unit cells counted around the circumference of a nanotube can make the tube either metallic or semiconducting; if the wave vector K is commensurate with the nanotube circumference, then the nanotube is metallic; if not, it is semiconducting. Thus, for one-dimensional (1D) transport along the length of the nanotube, the band structure is semiconducting for two-thirds of tubes and metallic for the remaining one third. Similar effects are expected in graphene nanoribbons, where the hard-wall boundary conditions at the ribbon edge can result in metallic or semiconducting 1D dispersions.[17], [18]

The linearity of the band structure near the K-points, high Fermi velocity, small electron-phonon coupling, and absence of backscattering due to the pseudospin of the electrons are predicted to lead to extremely high mobilities (upwards of 200,000 cm^2/Vs) at room temperature.[11-13] This would put graphene at the top of the semiconductor hierarchy for room temperature performance, out-pacing silicon by two orders of magnitude. This incredible performance, coupled with the relatively low cost of obtaining graphene's precursors—highly-oriented pyrolitic graphite (HOPG), for instance—has pushed experimentalists to explore a variety of methods of graphene device fabrication in the hope of achieving large-scale production. Along the way, many phenomena unique to graphene systems have come to light.

Electron Transport in Graphene

In experimentally realistic conditions (i.e. graphene on SiO_2 or similar substrate exposed to a lab environment), graphene generally exists in a doped state. Since 2007, the Fuhrer group has performed a series of transport measurements on exfoliated graphene devices on Si/SiO2 substrates. To make graphene FETS, exfoliated flakes are contacted with Cr/Au contacts using electron-beam lithography. Four probe and Hall bar configurations are common. The devices are gated through the Si substrate, with the 300 nm oxide layer acting as the gate dielectric. Figure 3 shows an example of a graphene FET fabricated in the Fuhrer group for transport measurements.
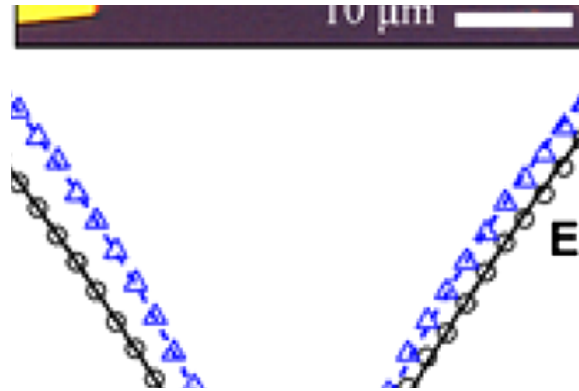
Figure 3: From reference [4]. A typical graphene FET fabricated from an exfoliated flake on an Si substrate with 300 nm oxide layer. The contacts are evaporated Cr/Au patterned by electron-beam lithography.

The material retains its linear dispersion relation, but the Fermi energy lies somewhere in the conduction or valence bands of the Dirac cone. Random charged impurities, present at the SiO_2/graphene interface, and also possibly on top of the graphene as a result of processing, limit the mobility of graphene due to charged-

impurity scattering. These impurities also give rise to a random potential that will cause graphene to be locally doped n- or p-type, forming electron or hole puddles.

Conductivity measurements of graphene FETs on SiO$_2$ substrates have consistently shown a linear relation between the conductivity, σ, and the charge carrier density (or carrier concentration), n. Since not all contributing factors to the conductivity obey a linear relation, this trend allows for the isolation of the dominant scattering sources. Theoretical predictions give charged-impurity scattering a linear relation

$$\sigma_{ci}(n) = C_{ci}e\left|\frac{n}{n_{imp}}\right|,\qquad(1.11)$$

where e is the electronic charge, n is the carrier concentration, n_{imp} is the concentration of charged impurities, and C_{ci} is a constant calculated from the screened Coulomb potential to be ≈ 5 x 10^{15} V^{-1} s^{-1}.[14], [15]

Equation 1.11 is expected to be valid at carrier densities high enough that inhomogeneities in the carrier density are negligible. At low carrier density, the inhomogeneity in carrier density due to the random Coulomb potential itself becomes important. A self-consistent model of graphene transport including both the minimum conductivity at low-carrier density and the linear $\sigma(n)$ at high-carrier density was developed using a random phase approximation (RPA)-Boltzmann formalism.[2], [16] Induced charge impurities in our current graphene devices will always induce a carrier density that makes the Dirac point experimentally inaccessible.

There are two regimes to consider for graphene transport, both revolving around charged-impurity scattering. The two regimes, low and high density, are

defined by the relation of the gate-induced average carrier density, n, to the residual carrier density n^*.

$$\sigma(n-\bar{n}) = \begin{cases} C_{ci}e \left| \dfrac{n^*}{n_{imp}} \right| & \text{if } n-\bar{n} < n^* \\[4mm] C_{ci}e \left| \dfrac{n}{n_{imp}} \right| & \text{if } n-\bar{n} > n^*. \end{cases}$$ (1.12) [2]

Here $\bar{n}$ is related to the shift in σ_{min} that is experimentally observed in [2]. The residual carrier density n^* arises from spatial fluctuations in the carrier density in the sample, and may be thought of as the rms carrier density when the average carrier density $n = 0$. Here, n^* is dependent on the charged-impurity density n_{imp} following the relation

$$\frac{n^*}{n_{imp}} = 2r_s^2 C_0^{RPA}\left(r_s, a = 4d\sqrt{\pi n^*}\right), \quad \bar{n} = \frac{n_{imp}^2}{4n^*}$$ (1.13) [2]

where C_o^{RPA} is the voltage fluctuation calculated using the RPA for screening. The RPA expansion is done about r_s, which is ≈ 0.8 for SiO_2. The constant $a = 4k_F^* d$ for purposes of the RPA method.[2] The distance, d, is between the graphene and the plane of charged impurities and is taken to be ≈ 1 nm.

The minimum conductivity σ_{min} is simply the conductivity of graphene at a carrier density n^*: $\sigma_{min} = n^* e\mu$.[3-5] The low-density regime occurs when $n^* > n$ and for typical graphene samples with $n_{imp} = 3$ to 10×10^{11} cm^{-2}, $n^* = 1$ to 4×10^{11} cm^{-2}. In the low density regime, charged impurities induce electron-hole puddles in the plane of the graphene.[3], [4] As the carrier density increases so $n > n^*$, the electron puddles grow and hole puddles shrink, resulting in an inhomogeneous screened Coulomb potential and a conductivity that is linear in n.

10

The theory of charged impurity scattering has been verified experimentally by doping graphene with potassium and measuring the conductivity *in situ* in ultra-high vacuum (UHV) at low temperature.[15] Figure 4 shows the carrier-density-dependent conductivity of graphene with various concentrations of potassium, which acts as a charged impurity. The experiment verified quantitatively the relation in equation 3.1, and also qualitatively the behavior in equation 3.4, that n^* is roughly proportional to n_{imp}, giving σ_{min} roughly independent of n_{imp}.
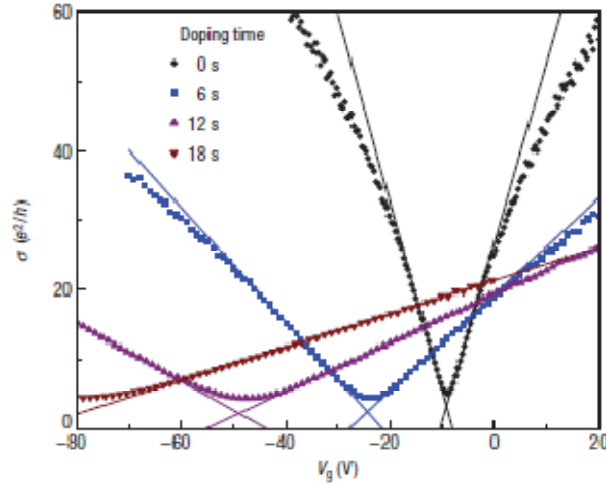
Figure 4: Conductivity (σ) vs. gate voltage (V_g) for graphene on SiO_2 for four different K dosing levels from Chen et al. (from reference [5]). K-dosing results in a shift in $V_{g,min}$, a decrease in σ_{min}, broadening of the minimum conductivity region and increased linearity of the conductivity curve as charged-impurity scattering is increased. The fit lines here are generated using equation 1.11.

To further study scattering sources, particularly the balance between long- and short-range range sources as controlled by screening, the dielectric environment of graphene FETs on SiO_2 was varied by the introduction of an ice layer in UHV at low

temperature.[15] The introduction of ice, with a relative dielectric constant $\kappa = 3.2$, has two effects. First, the Coulomb scattering potential is directly reduced since it is inversely proportional to the average dielectric constant $(\kappa_1 + \kappa_2)/2$, where are κ_1 and κ_2 are the dielectric constants of the materials above (ice or vacuum) and below (SiO$_2$) the graphene. Second, the electron-electron interaction is reduced, which results in a reduction in screening of the impurity potential

The linear dispersion relation for graphene gives rise to a dimensionless coupling constant, α, which is the ratio between the graphene Coulomb potential energy and kinetic energy. The dielectric environment around the graphene mediates the screening of charged impurities, altering the Coulomb potential energy. α may be written as:

$$\alpha = \frac{2\,e^2}{\left(\kappa_1 + \kappa_2\right)\,v_F}$$

(1.14) [2]

where κ_1 and κ_2 are the top and bottom dielectric constants. In this case, κ_2 is roughly 3.8, the dielectric constant for SiO$_2$. In air, κ_1 is 1, giving $\alpha \approx 0.81$. Introducing the ice layer, with $\kappa_1 \approx 3.2$, lowers α to 0.56. Changing the coupling constant in this manner affects the conductivity in two ways: (1) it improves the mobility, μ_L, due to long-range scattering by reducing the interactions of electrons with charged impurities, and (2) it decreases the short-range conductivity, because the more weakly interacting ice system no longer screens short-range scattering due to charged impurities as effectively. The experimental $\sigma(n)$ curves are fit to

$$\sigma(n)^{-1} = \frac{1}{n\,e\,\mu_L} + \sigma_s^{-1}$$

(1.15)

12

where $\mu_L = C_{ci}/n_{imp}$ corresponds to charged impurity scattering, and σ_s corresponds to

scattering by short-range impurities (delta-function correlated disorder).[2], [17]

These effects may be seen in Figure 5 with the change in slope of the conductivity

curve upon the addition of six layers of ice. The data are in good agreement with the

Boltzmann transport theory put forth by Adam et al. including screening.[2] For

short-range scatterers, the only effect is the reduction in screening, and the addition of

the ice reduces the screening of these puddles, causing the decrease in σ_s.
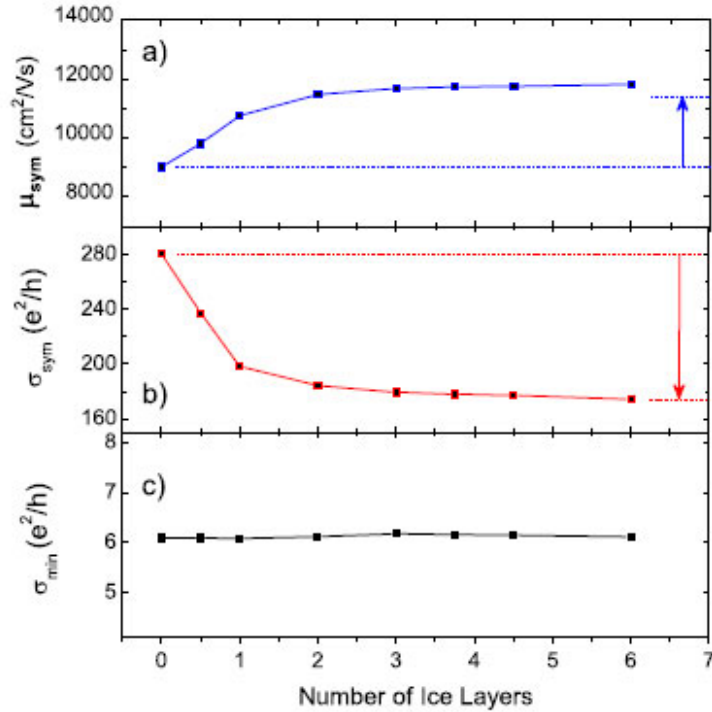
Figure 5: From reference [4]. μ_{sym} (corresponding to μ_L in text; blue squares), σ_{sym} (corresponding to σ_s in text; red squares), and σ_{min} (black squares) with respect to an increasing number of ice layers. The labels μ_{sym} and σ_{sym} here refer to the symmetric portion of the electron and hole sides of the conductivity curve. The mobility increases and short-range conductivity decreases while minimum conductivity remains constant. The predicted changes (arrows) are calculated from theory and are in good agreement with the data.

The experiments described above provide strong evidence for graphene's mobility being limited by charged impurities of a concentration a few 10^{11} cm^{-2}. The random impurity potential gives rise to another effect: at the charge neutrality point, graphene will break into electron and hole puddles. These puddles, in turn, screen the impurity potential; hence a self-consistent theory of the puddles is necessary.

Scanned Probe Measurements of Charge Inhomogeneity in Graphene

Since 2008, scanned probe techniques have been used to characterize the nature of charge puddles on the graphene surface. Most of these works have relied on STM technology to measure charge variation over regions comparable to the length scale of a single puddle.[3], [4] An exception to this was the early work by Martin et al. that employed a scanning single electron transistor (SSET) to measure the inverse compressibility of the graphene.[5]

In terms of the chemical potential, μ, the inverse compressibility $\partial\mu / \partial n$ is the inverse of the compressibility, or density of states $D(E) = dn/dE_F$, and can be measured locally by measuring the surface potential Φ_{total} as a function of carrier density as tuned by varying the gate voltage:

$$\left(\frac{dn}{dE_F}\right)^{-1} = -e\frac{\partial\Phi_{total}}{\partial n}. \tag{1.16}$$

The linear dispersion in graphene results in $\mu \propto n^{1/2}$ and $\partial\mu / \partial n \propto n^{-1/2}$. The divergence of the inverse compressibility at the Dirac point is smeared by fluctuations in carrier number, resulting in a finite peak in $\partial\mu / \partial n$. The local value of the Dirac

point potential can also be mapped by tracing the peak in $\partial\mu / \partial n$ spatially. Figure 6

shows a map of the Dirac point along a 2.5-micron line scan from Martin et al.

To map charge puddles, the SSET mapped potential fluctuations over areas of

a few square micrometers. From the potential map, charge density fluctuations were

extracted to produce the data shown in Figure 7. The density values were plotted as a

histogram and fit to a Gaussian curve. The density fluctuations averaged over the

SSET area are extracted to be $\Delta n = 3.9 \times 10^{10}$ cm^{-2}.
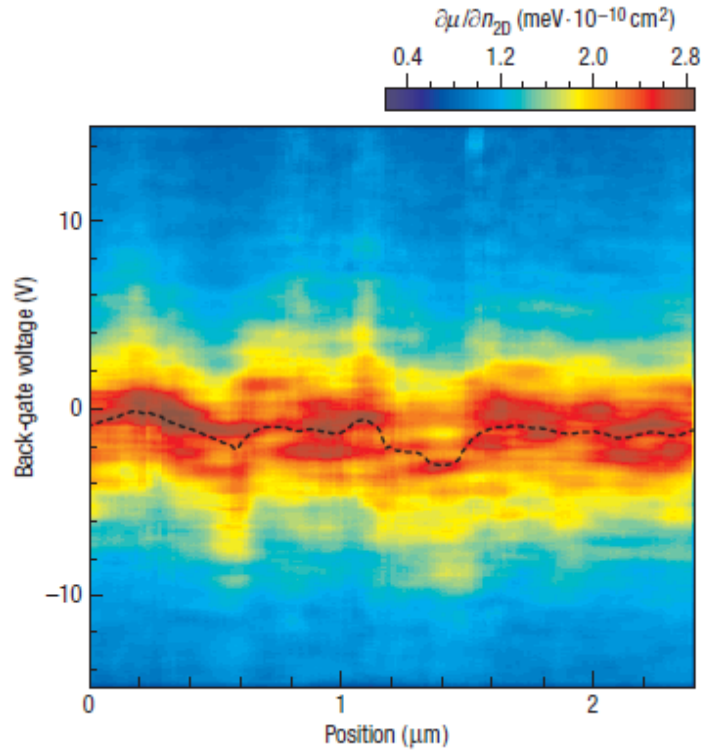
Figure 6: SSET measurements of the inverse compressibility of graphene on SiO$_2$ from Martin et al.

(from reference [5]) The inverse compressibility of graphene is measured along a 2.5 μm line as a

function of back-gate voltage. The change in position of the peak represents a shift in the Dirac point.

The smallest features resolved in this line are 150 nm.
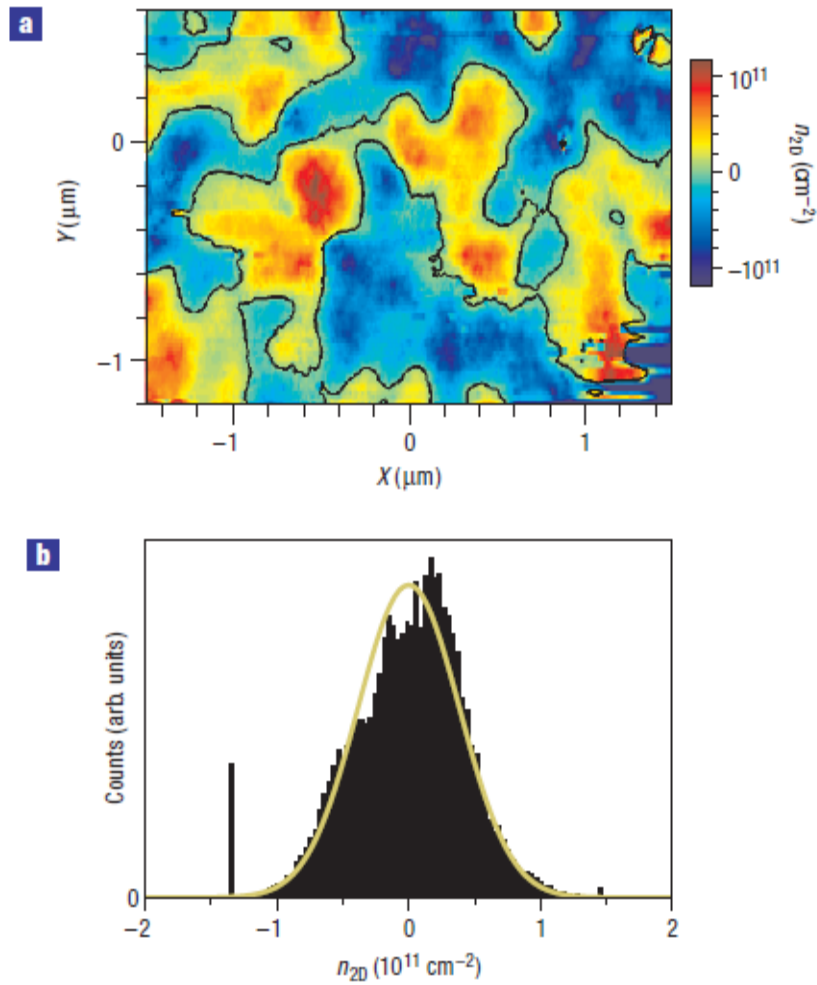
Figure 7: SSET measurements of surface potential of graphene on SiO_2 from Martin et al. (from reference [5]) Above (a) shows a map of the charge density as extracted from measurements of inverse compressibility. Below, in (b), the carrier density is plotted into a histogram and the carrier density fluctuations are extracted from the width of the histogram to be $\pm 3.9 \times 10^{10}$ cm^{-2}.

The SSET experiment was largely limited by its spatial resolution. The transistor had a diameter of 100 nm and was lifted 50 nm above the surface, approximating a spatial resolution of 150 nm.[3], [4] This value is considerably longer than theoretical puddle length scales. Martin et al. suggested that the actual density fluctuations were

of larger amplitude on a short length scale than measured using the SET. To correct for this, the carrier density dependence of the inverse compressibility was measured at high magnetic field (B = 11 T). In a field of 11 T, Landau levels are evident, and the broadening of the Landau levels gives $\Delta n = 2.3$ x 10^{11} cm^{-2}.[5] Comparison of $\Delta n = 3.9$ x 10^{10} cm^{-2} obtained from the histogram of the Dirac point spatial map and $\Delta n = 2.3$ x 10^{11} cm^{-2} obtained at high magnetic field (which should approximate the actual density fluctuations) indicates that the SSET resolution of 150 nm is $\approx$5x larger than the puddle correlation length which is $\approx$30 nm.

After the SSET work by Martin et al. was published, STM work further confirmed the size scale for a single charge puddle. In 2009 the LeRoy group at the University of Arizona and a collaboration of the University of California at Berkeley and the Lawrence Berkeley Laboratory both performed STM and scanning tunneling spectroscopy (STS) measurements on exfoliated graphene samples.[3] Both experiments were performed in UHV STM systems at 4.5-4.8 K. The STS method applies a DC bias voltage and small ac modulation to the tip and maps the variation in the differential conductance dI/dV over the sample surface. The variation in the location of the Dirac point as shifted by local potential variations is also measured at select locations. Both groups reported successful mapping of the graphene topography both at a scan size of 30 x 30 nm^2 and at atomic resolution. A sample measurement from Berkeley is shown in Figure 8. Zhang et al. measured *dI/dV* as a function of sample voltage and position over 40 x 40 nm^2 areas at sample voltages of -0.2 V, 0 V, 0.2 V, and 0.4 V and observed the effect of sample voltage on charge puddle size.[4] The sample voltage was applied by lithographically-fabricated metal

contacts on the graphene. The *dI/dV* mapping was performed in constant current

mode, causing the tip-sample distance to vary as the tip traveled over more or less

conductive regions on the graphene surface. From the *dI/dV* map, the charge density

fluctuation was extracted to be $\Delta n = 4.3 \times 10^{11}$ cm^{-2}.[4] This is in good agreement

with both the theory and the earlier SSET measurement done in high magnetic field.

The paper does not commit to a conclusion as to the origin of these density

fluctuations, although it does note that there is no correlation between the surface

topography and the charge puddles.[18] The presence of charged impurities is

suggested as a source of the charge inhomogeneity.
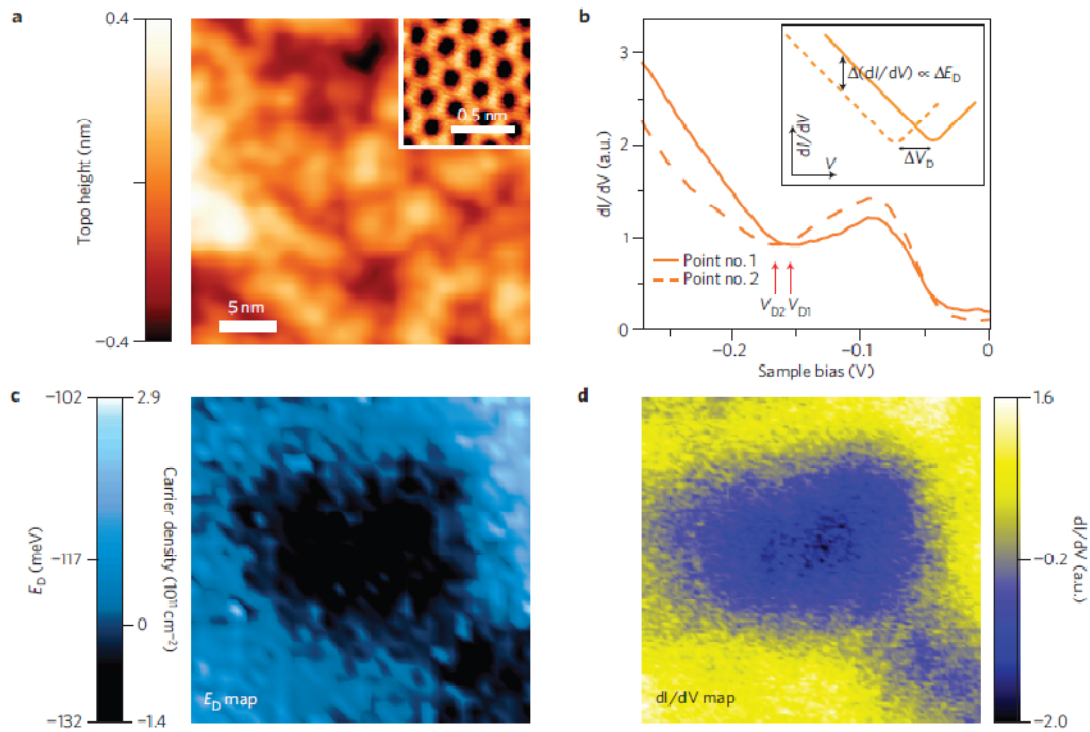
Figure 8: Topography and STS of graphene on SiO$_2$ from Zhang et al. (from reference [4]) Top left
(a) shows a topography image of a mechanically exfoliated graphene sample. The inset shows the
carbon lattice. (b) shows the dI/dV with respect to bias voltage taken at two points 17 nm apart. (c)
The map of the Dirac-point energy is extracted from the dI/dV map, shown here in (d) at a fixed gate

voltage of 15 V and fixed bias voltage of 0.25 V. The data in (a) and (c) are taken over the same

sample area, showing that there is no correlation between the topography data and the dI/dV map. The

puddle length scale may be seen here to be ≈20 nm.
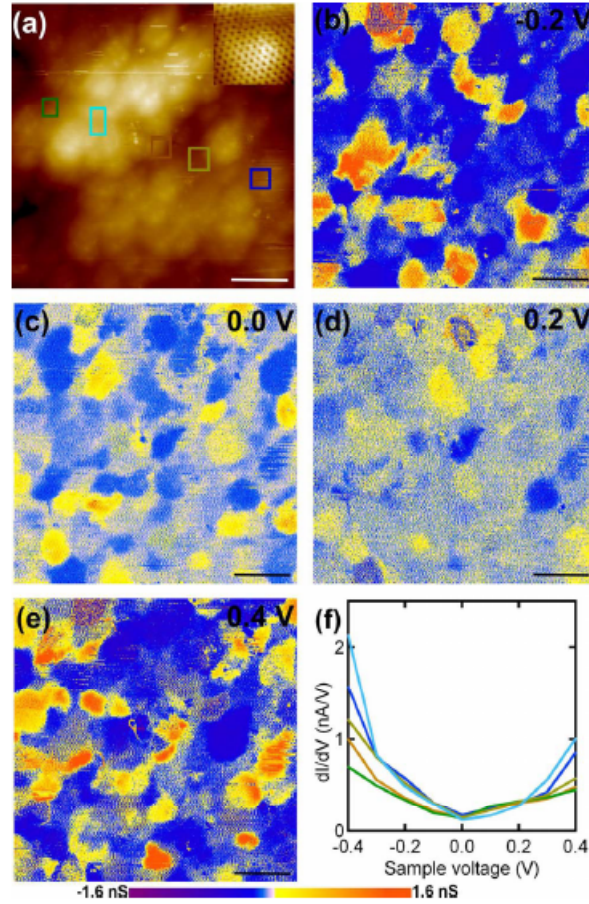
Figure 9: Topography and STS of graphene on SiO_2 from Deshpande et al. (from reference [3]) The

boxes in the topography image (a) correspond to spatially average dI/dV spectra taken as a function of

sample voltage and plotted in (f). (b) – (e) show dI/dV maps at four different sample voltages. Scale

bar is 8 nm.

The LeRoy work, shown in Figure 9 also credits charged impurities, likely

between the substrate and the graphene, as the source of the puddle behavior. The

Berkeley group agrees with LeRoy's work in finding charge-density fluctuations of

$\Delta n \approx 4 \times 10^{11}$ cm^{-2}. They map the Dirac point over an area of 30 x 30 nm^2 and find

that the charge puddles are ≈20 nm in diameter. This is in agreement with the value extracted by the SSET work at high magnetic field. In addition to observing charge puddles, quasi-particle interference patterns were also observed to be caused by the same scattering centers that caused the charge puddles. Rather than looking for a correlation between the graphene topography and the charge puddles, then, Zhang et al. used the imaging of quasi-particle interference patterns to associate individual scattering centers with charge puddles.[19]

Recently, the use of hexagonal boron nitride (hBN) as a substrate for graphene exfoliation has been of some interest, as hBN provides a flat, low-impurity platform for graphene devices. Both the LeRoy group at the University of Arizona and the Crommie group at Lawrence Berkeley National Laboratory have extended their STS studies to graphene on hBN.[20], [21] By mapping dI/dV on gated graphene/hBN devices, both groups report on lower surface roughness and lower carrier concentration variation compared with graphene/SiO_2 devices. In particular, the graphene conforms to the flat crystalline surface of exfoliated hBN flakes to give a surface roughness of 30.2+/- 0.2 pm, roughly eight times flatter than graphene on SiO_2. Figure 10(a) shows the topography for graphene on hBN. Figure 10(b) and(c) show a map of the tip voltage at the Dirac point for graphene on hBN and graphene on SiO_2, respectively, as extracted from dI/dV maps collected by STS. A histogram for the graphene/hBN data is shown Figure 10(d) in the main image and for the graphene/SiO_2 in the inset. The histograms for both data sets appear Gaussian but where the width of the graphene/SiO_2 distribution point voltage distribution corresponds to a low variation in carrier concentration for graphene samples on hBN

substrates. The low carrier concentration corresponds to larger charge puddles, as predicted for graphene with a lower charged impurity density.[21], [22] Work by the Crommie group similarly finds a lower charge-density roughness for graphene on hBN compared to graphene on SiO_2.[20]
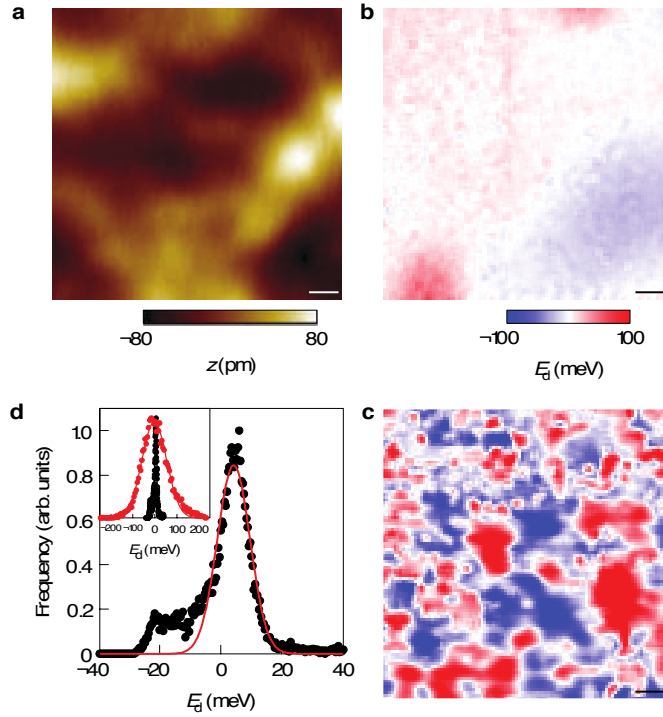
Figure 10: From reference [21]. (a) STM topography of graphene on hBN. (b) A map of the tip voltage at the Dirac point taken from dI/dV curves on graphene/hBN. (c) A map of the tip voltage at the Dirac point taken from dI/dV curves on graphene/SiO_2. The scanned area in panels (a), (b), and (c) are $(100 \text{ nm})^2$. The scale bar for panels (b) and (c) is 10 nm. (d) Histograms of Dirac point data for graphene/hBN (main graph) and graphene/SiO_2 (inset)

The lower charge density variation or Dirac point variation reported by the both the LeRoy group and the Crommie group is presumed to be due to the crystalline nature of the hBN substrate. The amorphous SiO_2 substrate serves as a source of

charge impurities that dominate scattering and limit mobility for exfoliated graphene devices on SiO_2 substrates. The hBN surface is flatter and more inert, without any dangling bonds that act as a source for charged impurities. As a result, graphene devices on hBN are strikingly similar to suspended graphene devices in their electronic properties, without the fabrication and fragility issues involved in working with a suspended device. From an applications standpoint, graphene on hBN is still hampered by the exfoliation problems common to graphene on SiO_2. Nevertheless, these recent studies of graphene on hBN provide good contrast for existing data on charge puddling in graphene on SiO_2. The larger puddle size and lower carrier concentration variation seen in these devices are indicative of the strong effect of substrate and dielectric environment on graphene charge puddling.

Conclusions

The existing body of experiment on graphene on SiO_2 points to charged impurities as a dominant source of static disorder. Graphene on hBN shows improved mobility, and lower charge inhomogeneity, suggesting reduced charged disorder is responsible for the mobility increase. Comparatively little is known about charge disorder in graphene on SiC. This thesis discusses the use of Kelvin probe microscopy as a tool to study the macroscopic and microscopic charge inhomogeneity of graphene on SiC. Chapter 2 discusses the experimental techniques of atomic force microscopy and Kelvin probe microscopy, and the synthesis and characterization of graphene on SiC samples used in this study. Chapter 3 outlines common methods for fabricating graphene samples, including original work done on chemically-derrved

graphene samples and current methods for fabricating the epitaxial graphene samples used later in this work. Chapter 4 describes an ambient-environment study of the macroscopic surface potential variations in graphene on Si-face SiC, and the results are also found in reference [23]. Chapters 5 and 6 discuss Kelvin probe microscopy of graphene on Si-face SiC in ultra-high vacuum (UHV). Chapter 5 discusses the layer-to-layer variations in the surface potential of graphene on Si-face SiC, while Chapter 6 discusses variations in surface potential within a layer due to disorder.

Chapter 2: Experimental Techniques

Atomic Force Microscopy – An Introduction to Scanned Probe Techniques

Kelvin probe microscopy (KPM) is the primary technique used in this work to study the charge distribution in epitaxial graphene samples by direct measurement of the local surface potential variations over the sample surface. KPM is a variation on atomic force microscopy (AFM), a technique which itself was developed in 1986 as a modification of early scanning tunneling microscopy (STM) methods. The first paper describing AFM was published in 1986 by Binnig and Quate in Physical Review Letters.[24] This was the same year that Binnig and Rohrer received the Nobel Prize in physics for their 1981 invention of the STM.[25], [26] Derived from the STM, the first AFM did not use the optical methods for beam deflection detection used today. Instead, the method of detection relied on the current tunneling loop as in STM to detect the deflection of a cantilever.

In its simplest form, the STM mapped the topography of a conducting surface by measuring and maintaining a constant tunneling current between the sample surface and a sharp tip. The first obvious limitation of this method was that it was not suited to measuring insulators. Other methods of surface measurement at the time included stylus profilometers and scanning capacitance microscopes, which were limited to ≈100 nm in spatial resolution and could not resolve atomic steps.

Binning and Quate's AFM used a handmade probe fabricated from a gold foil cantilever beam with a sharp diamond tip glued to the end of it. The STM tip was then placed above the cantilever, measuring a tunneling current between the tip and the gold foil. As the diamond tip passed over the sample surface, the cantilever was deflected, allowing for measurement of the surface characteristics through the STM feedback loop.
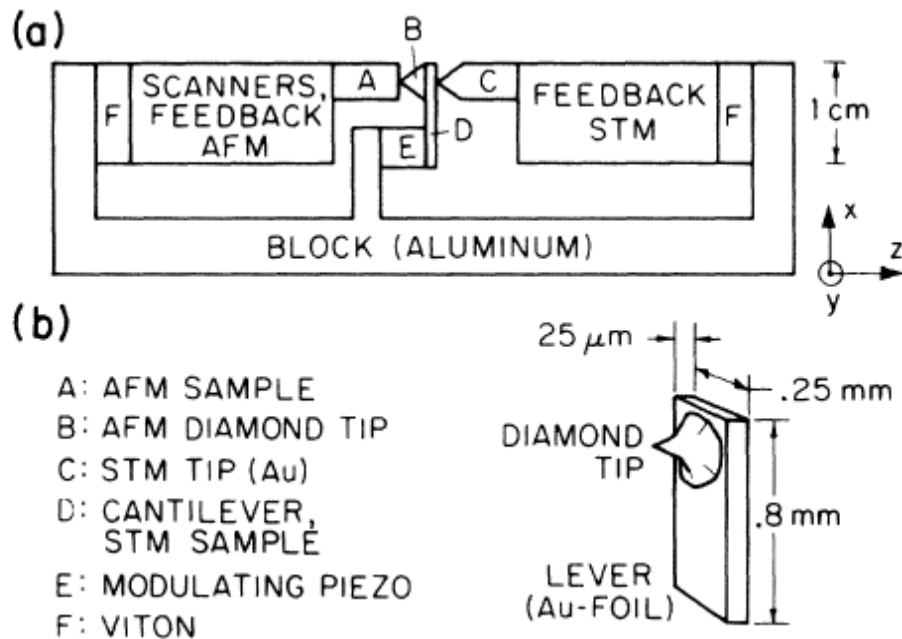
Figure 11: From reference [24]. (a) shows the setup for the AFM prototype developed by Binnig and Quate. The AFM cantilever, D, and diamond tip, B, were sandwiched between the sample, A, and the STM tip, C. Panel (b) shows the design for the handmade AFM probe.

The original work used the tunneling method of feedback to suggest four different modes of operation. The most successful mode of operation was to apply the ac modulation again to the AFM cantilever but to have it also attached to the tunneling current feedback loop. Previous methods used two separate feedback

loops, the traditional STM loop controlling the tunneling current and a second one modulating either the sample or AFM cantilever. By using just one feedback loop, the signal applied to the AFM cantilever is modulated specifically to maintain a constant tunneling gap between the cantilever and the tip.

The resolution of the first AFM was reported in terms of the smallest measurable force on the cantilever rather than in terms of topographical step heights, and was $\approx 10^{-15}$ N for the cantilever design described in Binnig et al.[24] To put this number in perspective, consider that the van der Waals bonds between atoms, the weakest interatomic bonds, are $10^{-11} - 10^{-12}$ N.[24] This means that the force sensitivity of even the earliest AFM cantilever was good enough to easily resolve interatomic forces. Binnig et al. estimated in their original work that a vertical resolution below 1 Å should be achievable.[24]

Shortly after the publication of the Binnig paper, further tailoring of the AFM was performed by Martin et al. at the IBM T. J. Watson Research Center.[27] In this work the method of cantilever deflection detection used was optical, relying on an optical heterodyne to measure the vibration of the cantilever. The optical heterodyne falls into the interferometry family of AFM detection methods. Optical methods currently used today do include interferometry, but laser beam deflection methods are simpler to implement and more commonly used.[24], [26], [27] The major advantage of optical detection was that it eliminated the need for the STM tip completely, consequently eliminating any perturbation of the force data by roughness on the back surface of the AFM cantilever.

As mentioned earlier, the AFM is a tool for measuring tip-sample forces as a means of characterizing a solid surface of arbitrary electronic properties. The interaction between the tip and the sample is the product of many forces, including the atomic bonds on the surface of the sample, but is most simply discussed in terms of van der Waals forces between the tip and the surface. To refer back to a familiar form from solid-state physics, the long-range potential between the AFM tip and the sample can be written as the Lennard-Jones potential for a chemical bond of strength E_{bond}

$$V_{Lennard-Jones} = -E_{bond}\left(\frac{\sigma^{12}}{r^6} - 2\frac{\sigma^6}{r^{12}}\right)_.$$

(2.1) [25]

Here, the first term describes the attractive van der Waals potential that is proportional to $1/r^6$ and the second term is repulsive and proportional to $1/r^{12}$. Modeling the interaction of a conical AFM tip with this potential gives a tip-sample force that follows a $1/r$ force curve. At smaller r, the potential due to surface chemical bonds is described in terms of the Morse potential such that:

$$V_{Morse} = -E_{Bond}\left(2e^{-\kappa(r-\sigma)} - e^{-2\kappa(r-\sigma)}\right)$$

(2.2)[25]

In both equations, σ represents an equilibrium distance, r is the tip-sample distance, and κ is the decay length for the Morse potential. A plot of the tip-sample forces is shown in Figure 12. It is interesting that while the van der Waals potential is short range at first glance, the forces add up to have a long-range effect. Electrostatic forces also have a strong effect on the tip; however, the overall shape of the force curve from Figure 12 holds true.
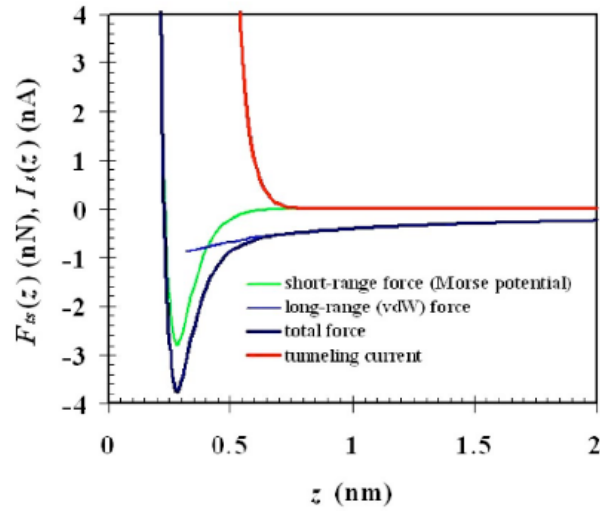
Figure 12: From reference [25]. The total tip-sample force is a sum of forces described by contributions from the long-range van der Waals potential and short-range Morse potential.

The force curve versus tip-sample distance is the primary guide for determining the mode of operation for AFM. At very small r, the tip experiences repulsive contact with the surface. This is the operating region for static AFM or "contact mode" AFM, the oldest of AFM methods. In contact mode, the deflection of the tip due to surface topography is directly measured. At further distances from the sample, the AFM may operate in intermittent, or "tapping," mode or noncontact mode; this is known generally as dynamic AFM. Tapping mode is today the most commonly used method for ambient AFM measurements. In tapping mode, the tip remains in the attractive force regime in the force curve but intermittently hits (or taps) the repulsive region close to the sample. Tapping mode is implemented by driving the cantilever with an ac signal. The deflection of the tip is measured while the perturbation of the driving signal by the surface forces is monitored by a variety of feedback loops.

28
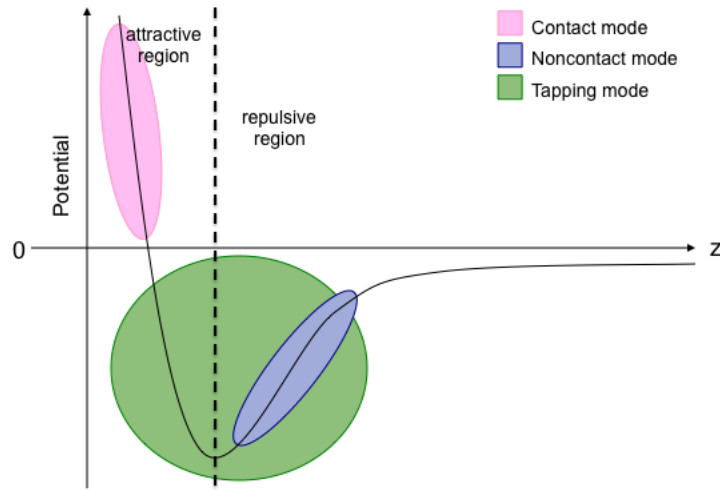
Figure 13: A simple cartoon of the force experienced by the AFM vs. tip-sample distance (z). The circles highlight the force conditions for contact mode, tapping mode, and noncontact imaging.

Within oscillating cantilever methods of AFM, there are two modes of operation: amplitude modulation and frequency modulation. The frequency modulation mode has several advantages over amplitude mode, including improved scanning speed in vacuum, but is largely restricted to noncontact UHV applications. Amplitude modulated AFM (AM-AFM) is the common method used in most ambient AFMs and is the mode of operation for the Veeco D5000 microscope used in the experiments described in Chapter 4. AM-AFM is also the older of the two operating modes and is described thoroughly in Martin et al.[27]

The methods described by the IBM group for tuning the resonance frequency of the cantilever and selecting a desirable operating frequency closely resemble the methods used currently.[27] In this work, and on the D5000, the operating frequency of the cantilever is not the resonance frequency at which the greatest tip deflection is achieved for a particular tip-sample force. The operating frequency of the AFM is

chosen such that the derivative of the amplitude with respect to frequency, $\partial A/\partial f$ is positive and maximized. This provides the strongest signal for measurement for two reasons. (1) As the tip approaches the surface, attractive forces shift the resonance frequency negative; thus, choosing the operating frequency to be below the resonance frequency means the signal at the operating frequency will increase with the shift. And (2) operating at the maximum of the derivative ensures the largest laser beam deflection due to the maximized change in amplitude with change in tip-sample interaction.

When the AFM tip is far from the surface, the amplitude of oscillation depends on the frequency of oscillation in the following manner:

$$A = \frac{A_0 (\omega_0 / \omega)}{\sqrt{1 + Q^2 (\omega / \omega_0 - \omega_0 / \omega)}} . \tag{2.3)[27]}$$

Here A_0 is the amplitude of oscillation of the tip at the resonance frequency ω_0 and Q is the quality factor of the tip. The derivative is maximized by the condition

$$\frac{\partial A}{\partial \omega} = \frac{4 A_0 Q}{3\sqrt{3}\, \omega_0} . \tag{2.4)[27]}$$

The resonance frequency is shifted by tip interaction with the van der Waals forces of the surface by an amount $\omega_0' = \omega_0 \sqrt{1 - f'/k}$ where f' is the force derivative normal to the surface and k is the spring constant of the tip.[27] The desired operating frequency is then given by

$$\omega_d = \omega_0 (1 \pm \sqrt{8}Q)\sqrt{1 - f'/k}. \tag{2.5)[27]}$$

At this frequency of maximum sensitivity, measurable amplitude shifts are

$$\delta A = \frac{\partial A}{\partial f'} \delta f' = \frac{2 A_0 Q}{3\sqrt{3}(k - f')} \delta f'. \tag{2.6)[27]}$$

The IBM group notes that the smallest measurable force derivative is dependent on the spring constant and quality factor of the tip and the temperature and environment in which the measurement is performed.

On our equipment—the Veeco D5000—I select the operating frequency to be 5-10% lower than the resonance frequency. This offset puts the operating frequency toward in the region of maximum positive slope on the tuning curve (amplitude vs. frequency). The resonance frequency itself will be shifted lower as the tip approaches the surface; thus, it is important to operate on the positive slope side of the curve to ensure that the shift does not result in a loss of signal. The autoengage routine common to Veeco microscopes (and previously Digital Instruments microscope) approaches the surface by measuring the damping of the tip oscillation amplitude by van der Waals forces. The set point chosen by the autoengage routine is representative of the fractional damping of the tip oscillation. A lower set point indicates a greater damping and therefore harder tapping force on the AFM tip.

The third regime for performing AFM is the noncontact mode. Originally attempted for both AM-AFM and frequency modulation AFM (FM-AFM) methods in ambient conditions, this type of AFM was proven to be most successful in UHV environments.[25] In noncontact mode, the primary interactions between the tip and the sample are due to the long-range van der Waals and electrostatic forces. In an ambient environment, this means that the presence of water and other adsorbates would cause a noncontact AFM image to look very different from a contact mode image and interferes with accurate surface measurements.[25] For this work, FM-AFM was implemented on a JEOL combination AFM/STM with an attached SEM for

location targeting. Unlike AM-AFM, the FM-AFM method maintains a constant tip

oscillation amplitude during the approach. That is, a tip tuned to a 4-nm oscillation

amplitude away from the sample surface will maintain that oscillation amplitude even

in the presence of van der Waals forces. Where the frequency shift due to tip-sample

interaction was accounted for in AM-AFM by a rough offsetting of the operating

frequency, it is exactly this shift that becomes the measureable quantity in FM-AFM.

The frequency shift is measured as a phase shift between the driving and detected

signals. A phase shift of 90° is equivalent to a null frequency shift.[25] For small

oscillation amplitudes and assuming a simple tip-sample interaction potential, the tip

frequency shift is described as $f = f_o + \Delta f$. Then Δf is dependent on the second

derivative of the tip-sample potential as follows:

$$k_{ts} = \frac{\partial^2 V}{\partial z^2} \quad and \quad \Delta f = \frac{k_{ts}}{2k} f_0. \tag{2.7)[25]}$$

Here k is the spring constant of the cantilever, and f_o is the resonance frequency. If

the tip-sample force gradient (k_{ts}) is not constant over the distance z between the tip

and the sample, then the force must be accounted for in an integral over the tip

oscillation period. To do this, the oscillation of the tip is described by a Fourier series

$$q'(t) = \sum_{m=0}^{\infty} a_m \cos(m 2\pi f t) \tag{2.8)[25]}$$

with an amplitude A, such that the frequency shift is now

$$\Delta f = -\frac{f_0^2}{k A^2} \int_0^{1/f_0} F_{ts}(q') \cos(2\pi f_0 t)$$

$$= -\frac{f_0^2}{k A^2} \langle F_{ts} q' \rangle \tag{2.9)[25]}$$

.

32

The quantity $\langle F_{ts} q' \rangle$ is then just a time average of the tip-sample forces over an oscillation period of the tip.

For noncontact FM-AFM on the JEOL AFM, I monitor the tip deflection signal using a phase-locked-loop (PLL) setup. The combination of the PLL and FM-AFM methods allows for lower noise and greater scan speed in UHV than AM-AFM.[25] The JEOL microscope used cantilevers similar to those used under ambient conditions in the D5000. For AFM only, silicon cantilevers may be used. Because this work was focused on collecting Kelvin probe data, I used Ti/Pt-coated silicon cantilevers with a resonance frequency of ≈300 kHz and Q of ≈8000-9000. The tip bias for normal imaging was set to be equal to the contact potential difference (CPD) minimum as found by sweeping the sample bias at low set point (-0.5-1 Hz) and finding the peak in frequency shift. By operating at the CPD minimum for noncontact imaging we eliminate the contribution of the previously mentioned long-range electrostatic forces. The set point for imaging was determined by taking Z spectroscopy curves. The ideal set point values had a slope of -(10-20) Hz/nm on the Z curve.

With the feedback properly optimized, both ambient AM-AFM and UHV FM-AFM can easily resolve atomic steps in the vertical direction. Although atomic resolution has been achieved by AFM methods, our images tend to have a lateral resolution of roughly 20 nm depending on tip radius of curvature. The metal-coated tip used in both ambient conditions and UHV for KPM have a somewhat larger size than the equivalent uncoated cantilever.

AFM is used throughout our work to provide accurate imaging of graphene surfaces. While the next section will discuss KPM methods separately, every surface potential image collected for this project was collected alongside a topographical image, either simultaneously (UHV) or by interleave scan lines (ambient).

The common implementations of KPM allow for the simultaneous collection of topographical and surface potential data for samples of varying electronic characteristics, presenting a variety of interfaces, and with a wide range of dimensions. Because the Kelvin probe technique is performed using an AFM, scan sizes are not limited as they are in scanning tunneling techniques. The large scan size is coupled with good tip-dependent spatial resolution, making KPM preferable to SSET, photoemission electron microscopy (PEEM), and other methods of measuring surface electronic properties. In its UHV implementation, the lateral spatial resolution of the surface potential is generally comparable to the tip radius. In ambient implementations employing a LiftMode™ technique, resolution is somewhat worse and depends on the lift height used during the Kelvin loop. When applied to measuring charge puddles in epitaxial graphene on SiC(0001), KPM is a powerful technique, with a spatial resolution of ≈20 nm (smaller than the predicted puddle size) and the capability to scan over several micrometers, measuring multiple puddles and microscopic variations in charge distribution. This section will present the details of KPM, discussing in particular the difference between KPM in ambient and UHV environments and how the resolution of these techniques is determined.

The first discussion of adapting existing AFM techniques to local surface potentiometry originated at IBM's T. J. Watson Research Center in 1991.[28], [29] Introduced by Nonnenmacher et al. as "Kelvin probe force microscopy," the name of the technique came from the non-local measurement from which it was derived.[28] The Kelvin force describes the force between two materials arranged as a parallel

plate capacitor. By mechanically vibrating one of the two plates, an oscillating

current is generated between the two plates as follows:

$$i(t) = V_{CPD}\omega\Delta C\cos(\omega t) \tag{2.10)[28]}$$

Here V_{CPD} is the contact potential difference (CPD) between the two plates. It

is this quantity that is locally measured in KPM. The vibrating signal is applied at the

frequency ω, and ΔC is the change in capacitance between the two plates. This

capacitance will be addressed in a different manner when the local probe

measurement is discussed.

In the parallel plate configuration, the Kelvin force measurement measures the

CPD between the different materials of the two plates without giving any information

about local variation within a material. The CPD is representative of the difference in

work functions between the two materials; thus, a local measurement of CPD

between a known and unknown material would give a measurement of the local work

function variation over a surface. Measuring spatial variations in a surface by local

probe techniques, then, provides insight into the nature of charge distribution across a

surface; and, in the case of graphene, allows for the characterization of charge

puddling.

For the adaptation of the Kelvin force measurement to a local probe

technique, the measured quantity to be considered is the force between the AFM

cantilever and the sample surface. In its simplest form, the force is derived from the

potential

$$U = \frac{1}{2}CV^2 \qquad \text{such that}$$

$$-\frac{\partial U}{\partial z} = F = -\frac{1}{2}V^2\frac{\partial C}{\partial z} \tag{2.11)[29]}$$

36

where F is the force on the tip, V is the voltage on the tip and $\partial C/\partial z$ is the change in tip-sample capacitance as the tip-sample distance varies. Weaver et al. note that in ambient this last quantity is poorly defined, effectively throwing a wrench into the idea that the force F is proportional to amplitude of tip oscillation.[29] The term $\partial C/\partial z$ is dependent on the dielectric environment between the tip and the sample, which may be affected by different surface adsorbates, in addition to the tip-sample distance.

There are a variety of methods in practice to accomplish the KPM measurement. In common implementations, a dc voltage $V_{\text{tip,dc}}$ and an ac voltage $V_{\text{tip,ac}}(\omega)$ at frequency ω are applied to a conducting tip. The technique employs two lock-in amplifiers, one to control the loop collecting topographical data and the second to measure the CPD between the tip and the sample and nullify the force on the tip. A more explicit form of equation 3.11 is given by

$$F_{ac}(\omega) = \left(\frac{\partial C}{\partial z}\right)\left[\left(\phi_{tip} - \phi_{surface}\right)V_{tip,ac}(\omega) + \frac{1}{2}V_{tip,ac}^2(2\omega)\right],$$ (2.12)

where z is the tip-sample distance, and ϕ_{tip} and $\phi_{surface}$ are the local electrostatic potential of tip and surface when in electrochemical equilibrium ($V_{tip} = 0$).

The Kevin probe method of surface potential measurement uses the first term in the force at frequency ω. This term drives oscillations at frequency ω resulting from mixing of the ac potential with the dc electrostatic CPD which results from different work functions for the two surfaces. The potential feedback loop is used to

apply a dc bias $V_{tip,dc}$ to the tip to nullify the CPD such that the force and the amplitude of oscillation is zero such that

$$V_{tip,dc} = \phi_{surface} - \phi_{tip} \tag{2.13}$$

and $V_{tip,dc}$ maps local variations in surface potential.

Both the original IBM work and current interpretations of KPM data tie the lateral variation in surface potential to the local variation in work function. The work function is the difference between the vacuum level and the chemical potential:

$$\mu_{tip} = \mu_{vac} - W_{tip}; \qquad \mu_{surface} = \mu_{vac} - W_{surface} \tag{2.14}$$

where W_{tip} is the tip workfunction. The electrostatic potential of tip and surface are related to the vacuum chemical potentials for electrons by

$$\phi_{tip} = V_{tip,dc} - \frac{\mu_{vac,tip}}{e}; \qquad \phi_{surface} = -\frac{\mu_{vac,surface}}{e}. \tag{2.15}$$

The feedback condition then gives

$$\mu_{vac,tip} = \mu_{vac,surface}$$
$$V_{tip,dc} = \mu_{tip} - \mu_{surface} = \left(W_{tip} - W_{surface} \right) / e \tag{2.16}$$

and $V_{tip,dc}$ maps local variations in $-W_{surface}$.

The frequency ω of operation for the ac signal varies from method to method and system to system. For this work, KPM was performed in an ambient environment using a Veeco D5000 scanning probe microscope with an internal lock-in amplifier was used. The ac signal is applied at the resonance frequency of the tip in LiftMode™. Each tapping mode scan line is interleaved with a LiftMode™ scan line. During the LiftMode™, tapping feedback was turned off, and the lock-in measures an oscillation resulting from a force at frequency ω. The feedback loop

applies the nullifying dc voltage $V_{tip,dc}$ such that the oscillation amplitude is zero. The interleaving of tapping and LiftMode™ scan lines means that topography and potential data are taken in alternating lines, mapping out exactly the same area for both channels of data.

Kelvin probe on the D5000 is implemented using a standard silicon AFM cantilever that has been coated with Co/Cr. The metal-coated tip provides a more uniform work function than bare silicon, allowing for a precise measurement of the sample surface potential variation without any question about the homogeneity of the tip work function itself. The Co/Cr tips used in this work had a resonance frequency of ≈60-90 kHz, somewhat lower than a standard silicon tapping cantilever with resonance at ≈300 kHz. The primary disadvantage in using a coated tip is that the metal coating increases the radius of curvature on the cantilever. While a bare cantilever may have a tip radius of < 20 nm, the Co/Cr tips like the one shown in Figure 14 tend to be in the 20-40-nm range. The lateral resolution of the topographical data is roughly the same as the tip radius, while the lateral resolution of the Kelvin measurement is the tip radius plus the particular lift height used. This work was performed using Co/Cr tips produced by both NanoWorld and Veeco, with similar results. It is worth noting that Veeco also produces Pt/Ir coated tips with improved radius of curvature; however, the Pt/Ir coating was found to be not as robust under repeated scanning, causing frequent tip failure.
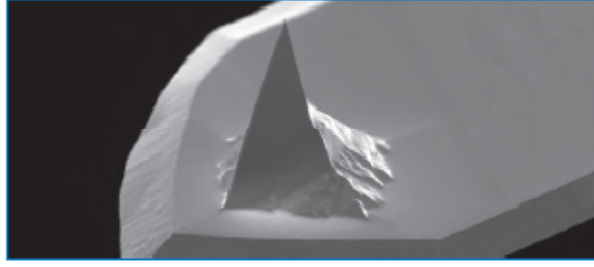
Figure 14: From the Bruker (formerly Veeco) probes catalog. An SEM image of a Co/Cr coated AFM cantilever with a tip radius of 20-40 nm.

The vertical resolution of all AFM techniques, both for height data and surface potential measurement, is much better than the lateral resolution. While the lateral resolution for AFM with our tips is quoted at 20-40 nm for topographical data and 20-100 nm for surface potential data, depending on lift height, the vertical resolution is much more sensitive to changes in tip-sample interaction. In normal AFM operation, the vertical resolution of the D5000 is sub-nanometer, easily resolving single graphite (0.33 nm), SiC (0.25 nm) and atomic steps. The surface potential resolution during Kelvin probe operation is dependent on different factors depending on the implementation of the method. For ambient measurements on the D5000, the limiting factor is thermal noise. The surface potential resolution of a tip is affected by thermally induced noise and may be calculated from the tip properties via [28]

$$V_{CPD,\min} = \sqrt{\frac{2k_B T\,k\,B}{\pi^3 Q f_{res}}} \left(\frac{1}{\varepsilon_0 V_{AC}}\right)\frac{d}{R}. \tag{2.17}$$

Here $V_{CPD,min}$ is the minimum CPD resolvable by the cantilever, k is the spring constant of the cantilever, B is the bandwidth of the feedback loop, Q is the quality factor of the tuned cantilever, f_{res} is the resonance frequency, V_{AC} is the ac signal

40

applied to the tip ($V_{tip,ac}$), d is the tip-sample distance, and R is the radius of curvature

of the tip. For a 60 kHz cantilever operating in ambient conditions in our D5000,

$V_{CPD,min}$ is ≈ 2 mV. The variation in Q from ambient to UHV means that $V_{CPD,min}$

should be orders of magnitude better in UHV. However, using values for the 300

kHz tips used in the JEOL UHV system, the surface potential resolution at resonance

is again ≈ 2 mV. In our UHV system, the Kelvin loop operates away from f_{res},

resulting in a lower thermal noise contribution. We suggest further that in the case of

the JEOL UHV system, thermal noise may take a backseat to noise introduced by the

phase-locked loop setup responsible for data collection. For our purposes it turns out

that a resolution of ≈ 1 mV is about an order of magnitude below the standard

deviation in surface potential within an image collected in ambient conditions in the

D5000. This will be discussed later, but for now this figure shows that I am able to

collect meaningful surface potential data on our samples with good resolution.

The surface potential measurement is performed by applying a 1500-mV ac

voltage, $V_{tip,ac}$, to the tip at resonance frequency, ω, with the tip lifted 2-20 nm above

the graphene surface and the piezo driver turned off. The tip voltage $V_{tip,dc}$ is

controlled by a feedback loop such that the amplitude of the tip at the ac frequency is

zero. For graphene, I expect that $W_{surface} = W_{cnp} - E_F$, where W_{cnp} is the work function

of charge-neutral graphene on SiC (0001). Hence $V_{tip,dc}$ directly tracks variation in

E_F, and I take the standard deviation in V_{tip} to be equal to $E_{F,rms}/e$.

Other methods of simultaneous data collection rely on applying the ac signal

at an off-resonance frequency and using the lock-in to separate the at-resonance

topography data from the off-resonance potential data. The UHV implementation of

41

KPM as performed for this work is conducted on a JEOL combination AFM/STM with an SEM attached. The UHV analog of traditional tapping mode AFM is noncontact mode AFM. To perform KPM in noncontact mode, the ac voltage is applied to the tip at an off-resonance frequency ω_{kelvin} simultaneous with the topographical loop running at the tip resonance frequency ω_{res}.

Performing KPM in UHV carries several distinct advantages over ambient KPM. The first is simply due to the difference in implementation. The noncontact mode methods employed in UHV eliminate the need for a lift height as employed in the interleaved ambient scan. Because the tip is closer to the sample surface during the CPD measurement, the spatial resolution is improved over ambient values.

The lateral resolution of UHV KPM is better than that of ambient KPM. The resolution of ambient KPM is roughly the tip radius plus the necessary lift height. The choice of lift height is determined primarily by surface topography. During LiftMode™ operation, the side of the AFM cantilever may interact with step edges and features if the lift height is smaller than the tallest features. The lift height must be chosen so that the tip is never closer to the side of a step or feature than to the surface itself. For graphene on SiC(0001), the lift height used may be small, as noted previously because the sample surface is devoid of tall steps and abrupt surface features. The small tip-sample distance of the non-contact KPM implementation allows for lateral surface potential resolution comparable to the lateral resolution of the topographical data.

The third advantage of UHV KPM over ambient KPM lies in the adequate description of $\partial C / \partial z$. The tip-sample capacitance in an ambient environment is

affected by a variety of factors, particularly the dielectric environment between the tip and the sample. At first glance, the primary difference between ambient and UHV techniques is simply the difference in dielectric constant between air and vacuum. However, in an ambient environment, the question of surface adsorbates becomes much more important. Samples used in UHV KPM have been heated at 420 ^{o}C for 15 minutes to clean off most surface contamination. This, combined with the UHV environment, means the sample surface is cleaner than in ambient conditions. In an ambient environment, it can be assumed that there is a layer of adsorbates on the sample. If this layer is homogeneous, all measurements of *variation* in surface potential are unaffected. However, graphene on SiC(0001) samples does not present a completely homogeneous surface for these adsorbates. Epitaxial graphene samples, in addition to monolayer graphene, have bilayer and exposed IFL regions that may have different surface energies and may attract adsorbates differently. The simplest evidence of this is that Al_2O_3 top gate dielectrics deposited by atomic layer deposition (ALD) does not stick equally well to monolayer and bilayer graphene regions on a single sample, with the film "beading up" and not adhering to bilayer regions.[30] Different adsorbed layers on monolayer and bilayer regions of the sample could skew the ambient measurement of surface potential differences on the two surfaces. While this work will look at the matter of distinguishing graphene layers by KPM in ambient and UHV conditions, it may be the case that ambient results across different surfaces cannot provide conclusive surface potential steps unless supported by UHV work. That there is a surface potential step between layers is clear, but the height of this step may not be absolutely determined in ambient conditions. Variations within a

single graphene layer or single surface do not have this same problem; nevertheless, the inherent variability in $\partial C/\partial z$ gives strong motivation for performing measurements in UHV.

In the JEOL tool, an ac voltage of 300 mV amplitude is applied at $\omega_{kelvin} = 450$ Hz, much lower than the typical ω_{res}. The cantilevers used in the JEOL are multi-purpose metal-coated AFM cantilevers similar to those used in ambient conditions. The particular cantilevers used in this work are MikroMasch Pt-coated silicon AFM cantilevers with a resonance frequency of $\approx$300 kHz. The topographical data are collected using a phase-locked loop operating at ω_{res} while the surface potential data is collected at ω_{kelvin}. The limitation of this method is that the scan speed must be slow enough to allow the PLL to follow the 450 Hz Kelvin signal. Scan speeds in UHV are in general much slower than in ambient. Ambient AFM and KPM scan speeds used in this work are general several microns/s, while ambient images are generally captured at 100-550 nm/s. Scan speeds for UHV KPM are slower than UHV AFM because the operating bandwidth of the PLL has to be widened from 200 Hz to 500 Hz to accurately measure the 450 Hz Kelvin oscillation. The quality factor for AFM cantilevers is boosted in UHV to be $\approx$8000 for the Mikromasch tips. Finally, the simultaneous operation of the Kelvin probe loop and the topographical loop in UHV decouples the topography data from any electrostatic variation in the sample surface due to variation in the charge environment. The Kelvin loop nullifies the electrostatic force on the tip, allowing for the topographical data to be a true measurement of the van der Waals interaction in the noncontact regime.

Chapter 3: Methods for Fabricating Graphene

Introduction

This chapter provides a summary of the current common methods for fabricating graphene. While exfoliated graphene flakes have provided an adequate platform of study for much of the fundamental research characterizing graphene since 2004, the low-yield and size limitations of doing experiments on flakes makes them poorly-suited for large-scale applications. Before focusing my work on epitaxial graphene samples, I briefly worked on depositing graphene flakes on SiO_2 using solution-phase methods. The techniques involved in fabricating graphene by mechanical exfoliation (the "Scotch tape method"), solution-phase processing, chemical vapor deposition, and epitaxial growth on SiC substrates are discussed here.

Mechanical Exfoliation

The first fabrication method widely used for making graphene electronic devices was mechanical exfoliation or micromechanical cleavage.[12] Graphite is cleaved using double-stick tape and tweezers and placed on a SiO_2/Si substrate. The cleaved graphite is in the form of ultra-thin flakes 1 to 2 mm long. The flakes are rubbed or pressed with tweezers or another piece of substrate until the bulk of the material is removed, leaving behind many small flakes of graphene and thin graphite.
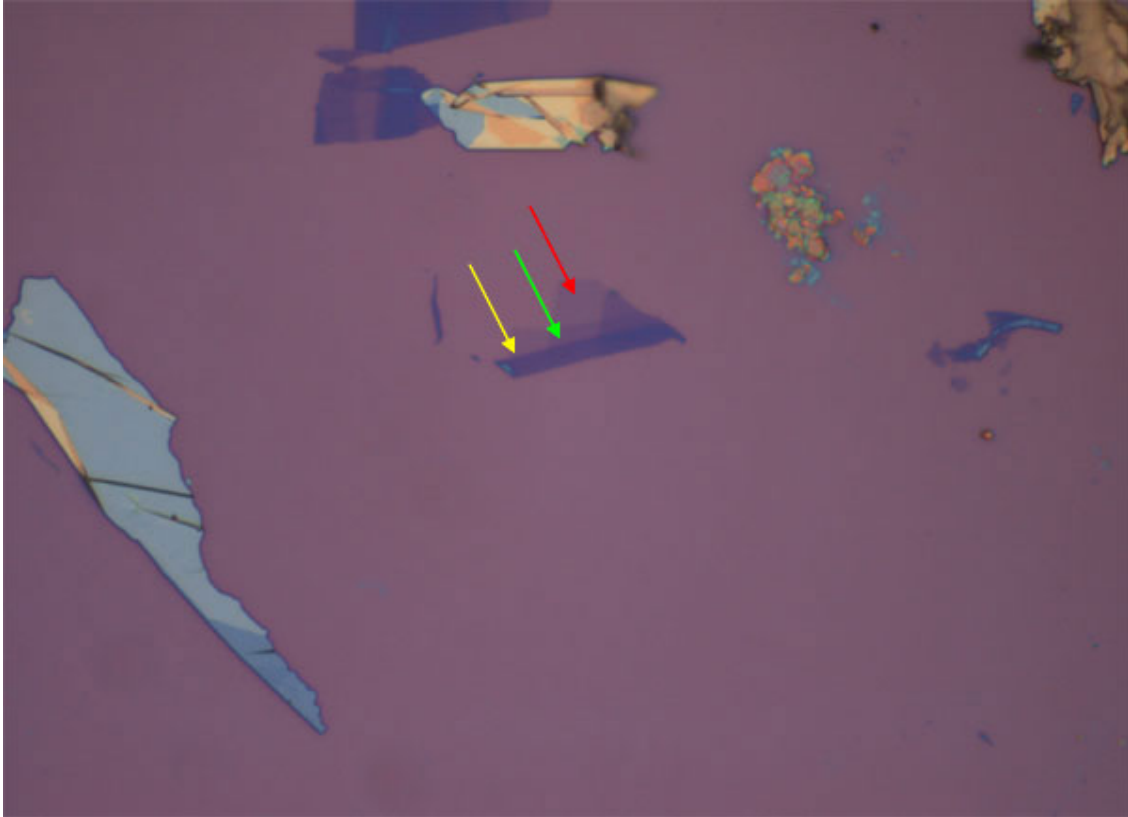
Figure 15: Optical micrograph of monolayer graphene and thicker graphite flakes on 300-nm SiO$_2$. The central graphene flake is folded, revealing mono- (yellow arrow), bi- (red line), and trilayer (green line) regions as well as thicker areas.

Figure 15: shows an optical micrograph of graphene debris on a substrate of 300-nm SiO$_2$ over Si. The visibility of monolayer graphene on SiO$_2$ of varying thicknesses has been well documented and is largely dependent on the wavelength of the light used.[12] Monolayer graphene is visible on 300-nm oxide with the peak in the contrast spectrum occurring in the green light range ($\approx$550 nm).[13] Graphene on 200-nm oxide is not visible at this commonly used wavelength or under normal white light.[12] The primary effect of changing oxide thickness, then, is to shift the wavelength at which maximum contrast appears.[13] Graphene may be made visible

on a wide range of SiO_2 thicknesses by the application of the correct light filters. The

200-nm oxide thickness, for example, requires a filter in the blue light range.[11] The

visibility of graphene on any dielectric is relatively surprising, given that it only

increases the optical path by ≈ 0.34 nm. Graphene is made visible by two

mechanisms: (1) the phase shift that occurs in any interfering light when passing

through a medium of different refractive index and (2) the opacity of the graphene,

which is commonly discussed with reference to its extinction coefficient.[11-13]

Experimental observations agree with models calculating the index of refraction of

graphene to be $\approx 2.0 - 1.1i$.[31] The use of 300-nm oxide is ideal because of its wide

availability and because optimum contrast is easily reached using normal microscopy

light. The maximum contrast reported for graphene on SiO_2 is $\approx 10\%$ using white or

green light.[31] Flakes thicker than monolayer appear darker and more opaque and

are easily observed on the SiO_2/Si substrate.

Wiring transistors from these samples is most commonly done using electron

beam lithography. Alignment markers are put down around the graphene flake, and

contacts are designed to accommodate the particular geometry of the flake and the

measurement being performed. While mechanical exfoliation is one of the most

widely used graphene fabrication techniques, it is not ideal for transistor fabrication.

Only about one to three in ten wafer chips will yield graphene flakes. The process of

locating these flakes using an optical microscope is time-consuming, and there is no

guarantee that flakes will be isolated enough or that they will be large enough to wire.

Experimentalists continue to rely on this method of fabrication because it is still the

cheapest and cleanest way to get graphene flakes, and exfoliated graphene on SiO_2

exhibits high quality, with low-temperature charge carrier mobility typically in the range of 10000 -20000 cm^2/Vs.

Solution-phase Methods of Obtaining Graphene

The impetus to seek out methods for fabricating graphene via solution processing had its roots in two previous areas of experimental work. Work done by Hongjie Dai and others had already shown that it was possible to dissolve carbon nanotubes in solution without damaging their unique electronic properties. More specifically, dissolving carbon nanotubes with long-chain polymers such as poly(m-phenylenevinylene-co-2,5-dioctoxy-p-phenylenevinylene) (PmPV) was ideal because the polymer bonded non-covalently to the nanotube.[32], [33]

To put graphite in a form suitable for solution processing, maximum surface area had to be exposed and made available to the dissolving polymer. The history of functionalizing graphite as a means of generating expandable graphite dates back to 1859.[33] To create expandable graphite, graphite is intercalated with sulfuric and nitric acids, causing the oxide groups to bond between graphite layers, effectively exfoliating the material. Upon rapid heating, oxide groups burn off, and the acid-intercalated or acid-washed graphite expands to 500 times its original volume, greatly enlarging the space between individual layers. In the past, acid-intercalated graphite has been used as a flame retardant and is widely available from commercial sources. Uniting these two techniques, expandable graphite is well suited to dissolving in solution, while long-chain polymer methods hold promise for preserving the desirable electronic properties of graphene.

In January 2008 the Dai group at Stanford reported the fabrication of semiconducting graphene nanoribbons from solutions of acid-washed graphite and PmPV.[34] Dai's process produced graphene nanoribbons ranging in width from less that 10 nm up to 50 nm and with lengths around 1-1.8 μm. SiO_2 substrates pre-patterned with alignment markers were soaked in graphene/PmPV/dichloroethylene (DCE) solutions for 20 min, rinsed with isopropyl alcohol (IPA), and blown dry with Ar gas. Chemical residues from the solution were further removed by annealing the sample in air at $350^{o}C$ for 10 min and in vacuum at $600^{o}C$ for 10 min. Nanoribbons were found and characterized using AFM and TEM techniques. The use of AFM to measure nanoribbons requires an accurate measurement of the microscope tip size to deduce true nanoribbon width from apparent width.   Dai's discovery of nanoribbons by this method does not address the low yield of the process. Only 0.5% of the expanded graphite pieces was retained in solution with PmPV and dichloroethylene (DCE). The group started with ≈10 mg of graphite and while they characterized >100 ribbons, this was only a tiny fraction of the starting mass.

In my search for chemically derived graphene, I attempted to replicate the method published by the Dai group. Expandable or acid-washed graphite was obtained commercially from Anthracite Industries, Inc. The expandable graphite was first annealed at $1000^{o}C$ in forming gas for about 1 min. This annealing process caused the desired 500-fold expansion in the graphite, creating large gaps between graphene layers and making the material easier to dissolve into solution. The resulting pieces of expanded graphite were put in 10 mL of the aforementioned PmPV/DCE solution and sonicated for 30 min to create an even solution and further

break up the graphite. The suspension of graphite in PmPV/DCE was centrifuged for 5 min in ten 1-mL containers to allow larger pieces of graphite to separate out. The top portion of the liquid was then drawn off and spin-coated at low speed (1000 rpm) onto SiO_2 substrates. Drop-casting was also experimented with, but the rings of material produced by this method were too dirty to perform detailed characterization.
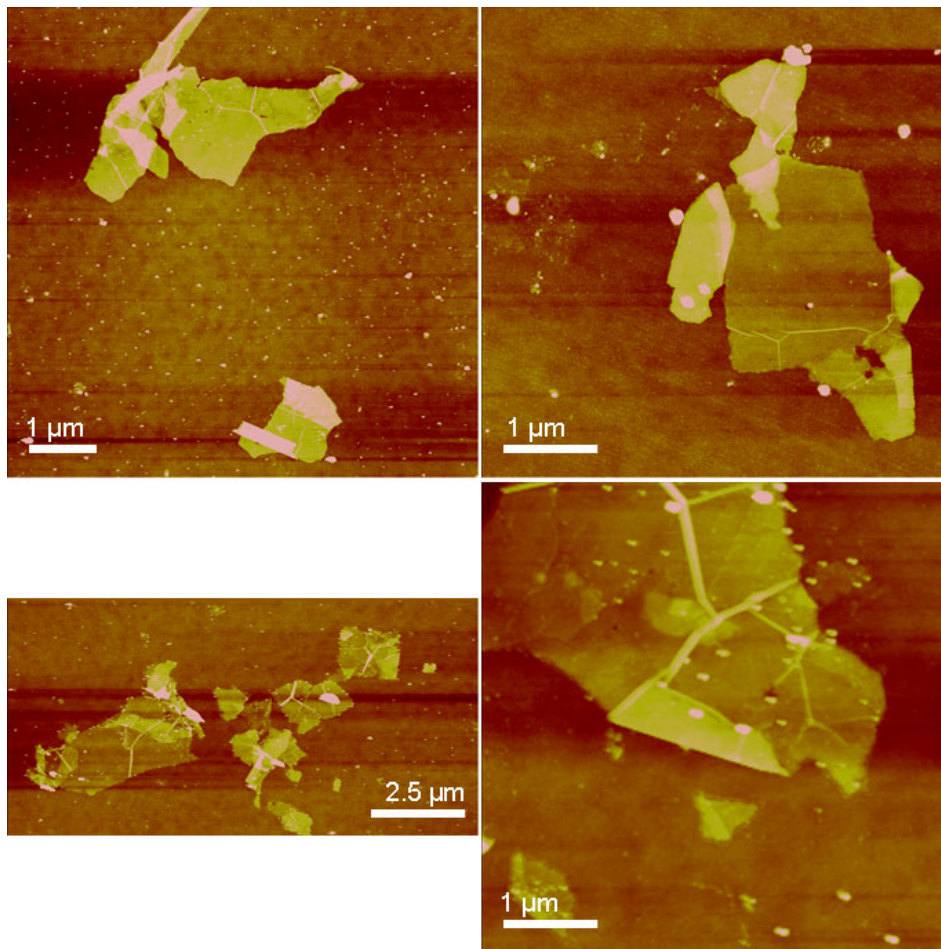
Figure 16: AFM images of chemically derived graphene flakes. The flakes were placed on SiO_2 substrates by spin-coating a solution of DCE/PmPV/expanded graphite that had been centrifuged and sonicated to facilitate the splitting of graphene layers. The vertical scale here is 30 nm for all the flakes except the top left figure where the scale is 20 nm.

Spin-coated samples showed a homogeneous covering of the SiO_2 surface with flakes of graphite and graphene from several to 20 μm in width. There was considerable variation in flake thickness from graphite-like thickness down to monolayers. Graphene and graphite flakes from spin-coating covered the SiO_2 substrate much more densely than anything produced by mechanical exfoliation.

The samples I generated on SiO_2 were first inspected in an optical microscope for likely monolayer and few-layer candidates. Further characterization of these flakes was done via AFM. Figure 16 shows a collection of monolayer and few-layer graphene flakes deposited on 300-nm SiO_2 using the PmPV method developed by the Dai group.[19] While individual nanoribbons were not found, flakes such as these were prevalent over the substrate surface. AFM characterization revealed several features: (1) monolayer and few-layer flakes, much like those made by mechanical exfoliation, frequently had folds and thicker regions; (2) flakes were characterized by wrinkles or pleating, possibly due to the deposition process; (3) flakes and the surrounding substrate were contaminated by small dots of chemical residue. Of the features observed by AFM, the problem of chemical cleanliness was the most troublesome. Although the PmPV is supposed to be bonded noncovalently to graphene, the exact nature of the observed residues is unknown, and their effect on graphene band structure is unmeasured.

While I was pursuing chemically derived graphene dissolved using PmPV, additional work was published indicating that this process was in no way unique to PmPV. Organic solvents (without polymers), such as *N*-methylpyrrolidone (NMP),

have also been shown to be effective in dissolving expanded graphite in solution.[19], [35-38]

In spite of the versatility of this method and the low cost of solution-processed methods in general, chemically derived graphene is still hampered by problems of yield and chemical contamination. Although graphene nanoribbons provide us with a platform for interesting physics, graphene flakes are much more observable. Still, the problem of properly cleaning chemically derived graphene flakes makes them less well suited to device fabrication than flakes produced by mechanical exfoliation. For this reason, chemically derived methods are currently considered more useful for work on graphene oxides and other graphene derivatives than for the production of pristine graphene samples.

Chemical Vapor Deposition of Graphene on Metals

Before the interest in 2D graphene peaked in the last six years, thin graphite was grown epitaxially on various metal and insulator surfaces as far back as 1966.[31] Growth of graphene on metal substrates by chemical vapor deposition (CVD) was first explored as an option for thin graphite film growth as early as 1974.[19], [35-38] While the original process involved annealing single-crystal Ni in UHV conditions, newer methods relied on polycrystalline substrates at easily attainable low vacuum pressure or atmospheric conditions.[36]

The recent work on CVD growth of graphene on nickel has focused on polycrystalline Ni as a substrate with the goal of obtaining large-area graphene.[19], [35] The substrates—either ≈300-nm thick films grown by electron-beam

53

evaporation [35], [36] or 0.5-mm thick foils [19]—are annealed in precursor gases. The gas composition is usually some combination of CH_4 or C_2H_2 gas and H_2 gas. Introduction of the hydrocarbon gas is usually preceded by a H_2 etch.[19], [35], [36] Two competing methods have emerged, the first requiring only atmospheric pressures [19], [35], [36] and the second operating at tens of mTorr [35]. Extensive work has been done to optimize the growth temperature, cooling process, and gas concentrations for both of these methods. For both atmospheric and low-pressure methods, a growth temperature of 900-1000°C is used.[36]

Growth studies measuring graphene quality with increasing temperature from 700 to 1,000°C indicated that, while graphene does grow at lower temperatures, the Raman D peak (only present in graphene and graphite with point disorder[39]) is prominent for samples grown at lower temperatures. In Figure 17: Raman studies show that as the temperature increases from 700°C to 1000°C, the D peak intensity decreases, indicating fewer point defects and higher quality graphene.[19] The G' peak has an full width at half maximum (FWHM) of only 33 cm^{-1}.
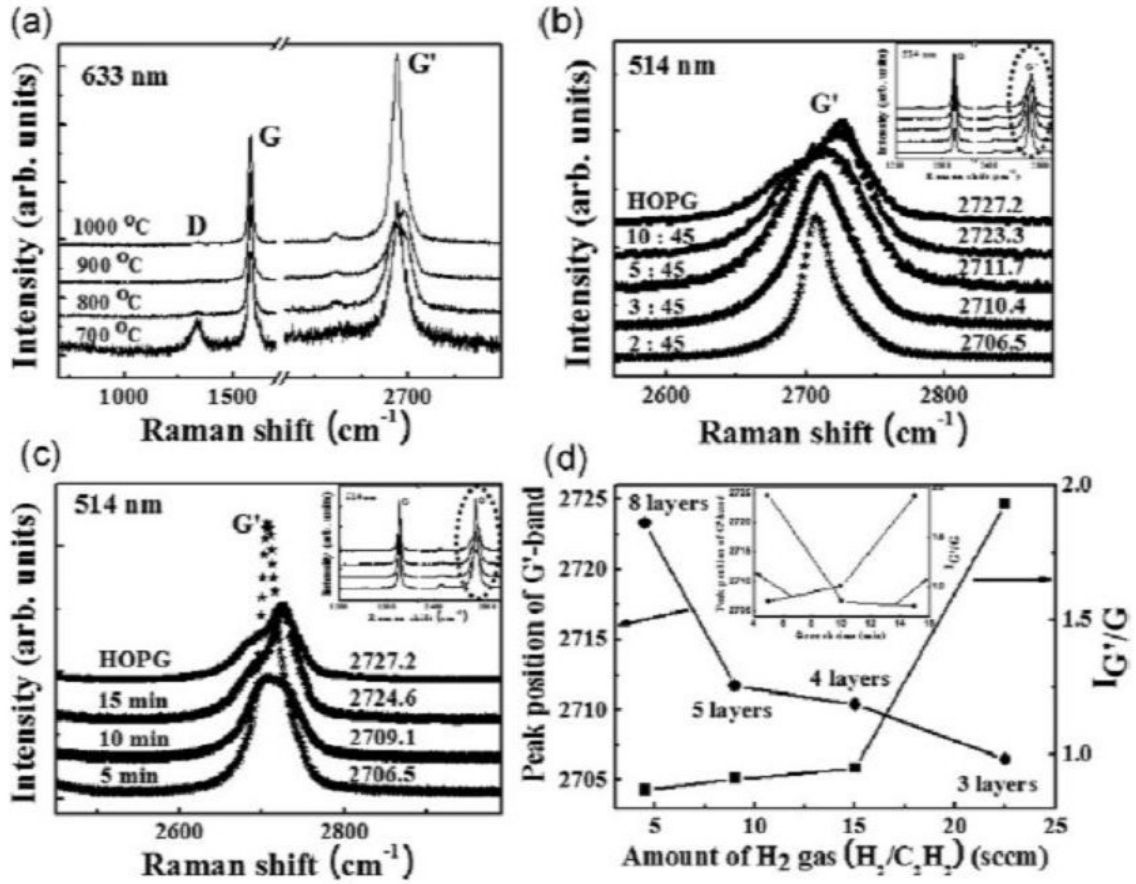
Figure 17: Raman spectroscopy of graphene grown by CVD on Ni substrates from reference [5]. (a) The evolution of the G' peak with increasing temperature shows that optimum growth occurs at 1,000°C. Similarly, the increase in temperature causes a decrease and eventual disappearance of the D peak. (b) The G' peak is shown to depend on the C_2H_2/H_2 ratio. The G' peak is strongest for a concentration of 2:45, and approaches that of HOPG with increasing C_2H_2. (c) Growth time is similarly optimized and viewed in relation to the G' peak for HOPG. (d) The position of the G' peak and the ratio of the G to G' peak are shown to depend on gas concentration. The inset shows these values to be dependent on growth time as well.

Although the growth of graphene on Ni is called "chemical vapor deposition," the growth mechanism is not a typical CVD process and should probably be referred to as a vapor-solid solution-solid process in analogy to vapor-liquid-solid (VLS)

growth. During the heating process, carbon is incorporated into the Ni lattice from the precursor gas, creating a solid solution of carbon in the metal. The solubility of carbon in nickel drops during the cooling process, causing the carbon to precipitate out and allowing for the controlled growth of several layers of graphene. This method of carbon precipitation is called carburization and is characteristic of growth on nickel.

In May 2009, the Ruoff group published work on CVD of graphene on Cu foils.[38] The Cu growth process differed from the previous work on Ni in two key ways: (1) because the solubility of carbon in Cu is much lower than that in Ni, the carbon does not become incorporated into the metal lattice; and (2) perhaps as a consequence of this, the growth process is more like traditional CVD, with carbon atoms adsorbing onto the Cu surface. These two factors combine to produce a growth process that is self-limiting, making monolayer coverage of 95% or better more easily attainable.

The self-limiting nature of the graphene-on-Cu growth process is tied to a substantial difference in the growth mechanism from the carburization that takes place on Ni. Because of the low solubility of carbon in Cu, the carbon from precursor gases does not become incorporated in the 25-μm-thick foils. Once the graphene fully covers the Cu surface, surface catalyzation is not possible, and the reaction stops after 10 min. Raman spectra of the grown graphene show good monolayer features with a strong G' peak at ≈2680 cm^{-1}.

To help answer some of the questions surrounding the various growth processes, the Ruoff group grew graphene on both Ni and Cu substrates using an

alternating sequence of a conventional CH_4 precursor gas and a precursor gas containing ^{13}C isotopes.[14] For the growth on Cu, $^{12}CH_4$ and $^{13}CH_4$ sequencing could be distinguished in the resulting graphene by Raman microscopy, consistent with surface adsorption as in the CVD growth process. Ni-grown samples showed a homogenous mixing of carbon isotopes consistent with the carburization or precipitation process.

Methods for fabricating CVD graphene into isolated electronic devices revolve around the acid-etching of the metal growth substrate. Ni foils and films may be completely etched away using solutions of HNO_3 or sulfuric acid. Prior to the acid etch, graphene is spin-coated with poly(methyl methacrylate) (PMMA), polydimethylsiloxane (PDMS), or other polymers. The resulting membrane floats and is relatively easy to deposit onto Si/SiO_2 substrates. Some samples have been successfully transfer printed onto transparent plastics to eliminate any folding or buckling that may occur. Top-gated field-effect transistors (FETs) were produced from graphene grown on Cu foils with an electron mobility of 4,050 cm^2/Vs.[16] This is well within the range of acceptable mobilities for current graphene devices and cements CVD graphene in the field of plausible graphene production methods.

Epitaxial Graphene on SiC

The first large-scale graphene production arrived in the form of epitaxial growth on SiC crystals. The first intentional forays into the graphitization of SiC in vacuum were published as early as 1960.[40] Interest in graphene, and the naming of

the single carbon layer, came later in 2002.[41] The first electronic transport

experiments on graphene on SiC, however, came in 2004.[42]

While Geim and Novoselov were publishing transport data on an exfoliated

graphene flake, Walt deHeer and Claire Berger were patterning and measuring a

single layer of graphene grown on SiC.[42] While much of the fundamental physics

of graphene, most notably transport work, has been carried out on exfoliated flakes,

work on epitaxial growth has to date provided the highest-quality large-area films.

Today, complimentary transport experiments have shown that epitaxial graphene

possesses the anomalous quantum Hall behavior, Raman G' peak, linear dispersion

relation, and other electronic properties unique to graphene and measured on

exfoliated flakes, meaning that the epitaxial film is just as much a true graphene as

the exfoliated flake.[41-47]

Of the many different crystal polytypes for SiC crystals, the 4H and 6H

configurations are most commonly used. The crystal structure for these polytypes is a

hexagonal structure similar to wurzite. The 4H and 6H polytypes are distinguished

by the relative rotation of successive layers of Si atoms. As shown in Figure 18, the

4H polymorph is characterized by an ABCB orientation, where the C and B layers

have atoms in the voids of the A lattice, and the C and B layers are rotated 60° with

respect to each other, so that the three voids in the A layer left open by the C layer are

aligned with atoms in the B layer. The 6H crystal structure is characterized by an

ABCACB stacking. Epitaxial growth experiments carried out on both 4H and 6H

crystal polytypes have seen no differences in graphene quality or electronic

properties.[43-45] The crystal face, and not the polytype, is the dominant factor in determining the topographical and electronic properties of the graphene.
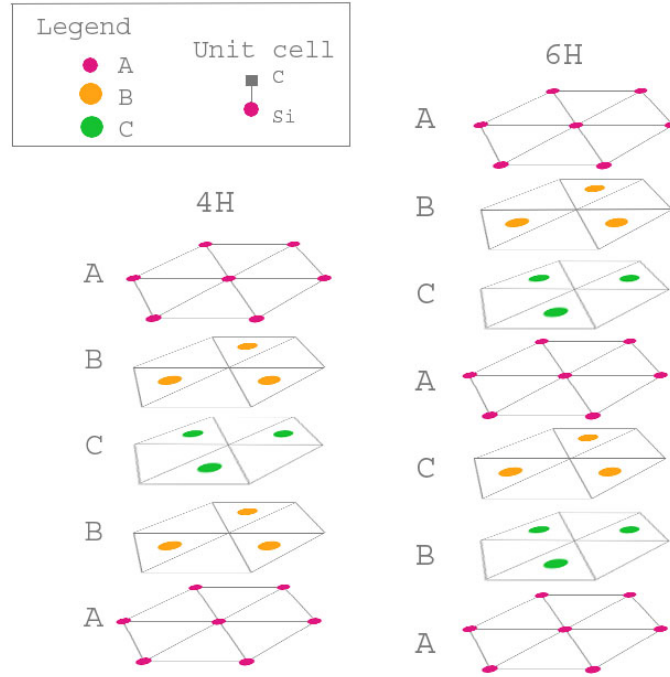
Figure 18: Crystal structure of 4H and 6H SiC. The 4H and 6H morphologies are characterized by ABCB and ABCACB stacking, respectively. Here the color points on the lattice each represent a single Si-C unit cell as shown in the top left box. Each layer in the lattice represents a bilayer containing these two elements.

Before graphene is grown, SiC substrates have to be prepared to create a smooth, growth-friendly surface. To achieve a good growth surface, mechanically polished SiC is etched in H_2 gas. The hydrogen etch produces slightly different results on the carbon and silicon crystal faces. In both cases the surface is etched into single step edges, but on the Si-face the steps are more closely spaced.[45] After the hydrogen etch, graphene is grown by annealing the SiC crystals at 1500-1600°C.

59

Originally, the high-temperature sublimation of silicon from the SiC surface took place in UHV. Samples grown by these methods were predominantly monolayer but had relatively poor surface morphology compared with later samples. In recent work, various methods have been employed to provide a gas overpressure to the growth environment. Tedesco et al. documents the successful growth of graphene in low-vacuum and argon environments using a CVD reactor.[45]

The CVD reactor method of Si sublimation employs an Ar flow ranging from low vacuum pressures up to 200 mbar. Under these conditions the growth rate of graphene is better controlled, producing Si-face films of monolayer thicknesses. On both crystal faces, the early stages of growth involve the formation of a carbon nanostructure coupled to the underlying SiC crystal.[18] The exact nature of this buffer layer is not well known. On the Si-face, the 0th layer or interfacial layer (IFL) is a disordered $6\sqrt{3}$ x $6\sqrt{3}$ reconstruction of carbon atoms. A large area percentage of this layer is sp^2 hybridized, although the pi-bands do not appear in ARPES data due to substrate-overlayer interactions.[46] The IFL is, in fact covalently bonded to the dangling bonds of the underlying SiC.[47] With further annealing, this layer becomes the sp^2-hybridized lattice that is a graphene monolayer, and the underlying layer develops the $6\sqrt{3}$ reconstruction symmetry. With each successive layer of growth, there remains an IFL of carbon between the SiC and the honeycomb lattice of graphene.

Graphene growth characteristics on the C-face, SiC(000-1), and Si-face, SiC(0001), of the substrate are distinctly different in surface morphology and electronic properties. The early epitaxial graphene papers of 2004 from Georgia Tech

focused on the Si-face of the substrate since monolayer results were more readily achievable. Since then, however, the group has done the bulk of its work on C-face growth. In the past six years, FETs have been patterned and measured on both sides of 4H and 6H substrates and the differences in growth on either side have been further distinguished.

On the C-face, growth typically proceeds rapidly to a thickness of many layers, destroying the ordered SiC steps left by the H_2 etch. Additionally, there is rotational disorder on the C-face, which causes decoupling of the layers.[18] Because of this, the top layer of C-face growth may appear electronically and spectroscopically similar to monolayer graphene although the actual graphene film thickness is tens of layers.

To explain further the role of rotational disorder in the growth of graphene on the C-face of SiC crystals, it is worth looking first at stacking in graphene flakes from mechanically exfoliated graphite. Exfoliated graphene from Kish graphite is Bernal stacked. If the graphene unit cell contains carbon atoms of type A and B, then in Bernal stacking, atoms of type A from the top layer are aligned over atoms of type B in the next layer down. Atoms of type B in the top layer are aligned over the hexagon center (empty space) in the lattice of the next layer down. The alignment of atoms in Bernal stacking gives bilayer graphene its unique parabolic band structure and Raman G' peak distinct from that of monolayer graphene.[18] Graphene growth on the Si-face follows Bernal stacking.[18] Bernal stacking is observed in some portion of C-face samples, but it is not prevalent. When graphene grows on the C-face, subsequent layers have a twist showing preferred angles near $\pm 30^{o}$ or +/-2°.[48-50] The twist

61

destroys Bernal stacking, destroying any coupling between the pi-orbitals of type-A atoms in the top layer and type-B atoms in the next layer down. This rotational stacking may be compared to that of turbostratic graphite and results in a decoupling of the graphene layers. Electronically, this means two things for graphene grown on the C-face. First, the increased thickness of the graphene combined with the decoupling twist decreases the screening in the top layers generated by impurities in the SiC. Second, Raman spectra taken on the C-face do not resemble the spectra for thick graphene or bulk graphite. A C-face sample tens of layers thick may exhibit a Raman spectrum similar to that of monolayer graphene if the top layer is twisted relative to the underlying layers.

The Raman signature for C-face graphene has a G' peak at $\approx$2720 cm^{-1}, distinct from Si-face and other forms of Bernal stacked graphene. Figure 19 shows a comparison of monolayer growth on the Si-face to rotationally disordered growth on the C-face, as well as a comparison of Bernal-stacked Raman spectra to bulk graphite. Where AB-stacked growth occurs, C-face graphene will have a G' peak that fits to a sum of two Lorentzians, similar to bulk graphite.[18] Thick graphene growth that is rotationally disordered will follow the single-Lorentzian behavior of other forms of monolayer graphene.
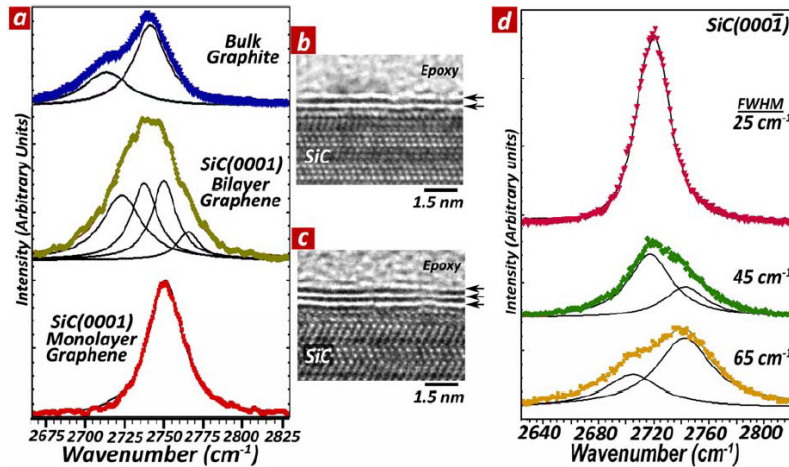
Figure 19: Raman spectroscopy of graphene on SiC from reference [15]. (a) Monolayer graphene (red peak) on the SiC(0001) surface fits a single Lorentzian, while the bilayer (olive peak) is fitted by four Lorentzians. The two-Lorentzian fit (blue peak) is provided for comparison. TEM may be used to resolve monolayer (b) and bilayer (c) growth along with the accompanying buffer layer. (d) On the (0001) crystal face, graphene growth is generally many tens of layers thick. Rotational disorder can lead to electronic decoupling, resulting in a single Lorentzian peak (pink curve). In the presence of Bernal stacking, however, C-face growth exhibits a Raman peak similar to that of bulk graphite (green and gold curves).

The rotational disorder of graphene on the C-face is not uniform across the entire sample. The characteristically multi-layer growth nucleates at the threading screw dislocations that are prevalent across the C-face of the substrate.[51] The screw acts as a source, allowing easy sublimation of silicon atoms. Growth proceeds outwards from the center of the screw in spiral fashion. Frequently, the spiral will encounter a substrate step edge and proceed outward in an arm. Because of the many screw dislocations over the substrate surface, graphene on the C-face grows in many islands that eventually contact each other to achieve complete coverage. Since the screws are not identical, different graphene islands may have different layer

63

thicknesses and different rotational ordering.[51] Because of this, it is possible to have a mix of Bernal stacked and completely decoupled, twisted monolayers on the films' surface when growth is completed.

The G' peak for monolayer graphene on the Si-face looks like that of an exfoliated graphene flake, with similarly narrow FWHM < 45 cm^{-1}. When bilayer growth occurs on the Si-face, the Raman G' peak is the sum of four Lorentzians, as it is with other Bernal stacked bilayers.[33] Because of the distinct Lorentzian G' peak, 2D Raman mapping may be used to identify high-quality monolayer graphene films on SiC(0001).[43]

The self-limiting nature of graphene grown on SiC(0001) is due to the different growth mechanism on this face of the substrate. On the Si-face, the screw dislocations do not appear to play a strong role in growth except in cases where their density per unit area is exceptionally high.[47] In these anomalous cases, many screw dislocations may be observed in a (100 μm)^2 area by AFM.[30] On "good" Si-face substrates with straight step terraces and a low density on screw dislocations, Si is most easily sublimated from step edges. These two types of growth are compared in Figure 20. The step edge is the primary source of Si sublimation and growth nucleation for Si-face substrates. Even poor substrates with a high screw dislocation density show a mixture of spiraling island growth and edge-nucleated growth.
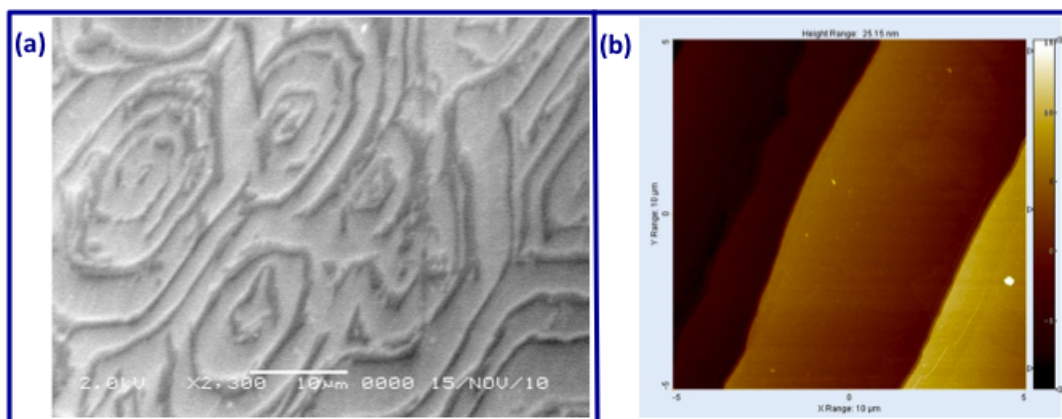
Figure 20: (a) An SEM image of graphene grown on SiC(0001). This substrate is an example of a sample with a high density of screw dislocations, resulting in poor, anomalous graphene growth. Graphene is located in the darker regions of contrast. The light grey regions are IFL. (b) An ambient AFM scan of graphene grown on SiC(0001). This substrate is an example of a normal arrangement of SiC steps.

In order to grow a single layer of graphene on the SiC(0001), three layers of SiC, totaling 0.75 nm deep, must be removed from the substrate. Si removal is thought to progress from the step edge "uphill" until the next step is reached.[52] Once the step edge is surrounded by monolayer graphene, growth is greatly slowed, limiting films to predominantly monolayer thickness. Depending on growth rate and SiC step bunching, a bilayer may be able to nucleate at the step edge, producing bilayer stripes along the film.[53] Also, sometimes areas of IFL are not covered by further growth. A further three layers of Si removal is necessary to grow the first properly decoupled layer of graphene.[46], [47] The exact manner in which Si sublimation progresses away from the step edge is still a matter under study. On substrates with wavy step edges and non-uniform terraces, graphene growth appear to

progress in "fingers" toward the next step.[52] This dendritic growth may be what causes IFL regions to be left behind after the majority surface is covered with monolayer graphene.

In spite of dendritic growth in the presence of wavy SiC step terraces, the Si-face produces good monolayer growth with fewer few-layer regions and topographical irregularities than graphene grown on the C-face. While C-face graphene samples have been shown to have very high electronic quality [54] , the ease of production of monolayer graphene on Si-face SiC makes it a good model system to understand the interaction of epitaxial graphene with its substrate. Furthermore, due to the true monolayer nature of graphene on SiC(0001), I am able to compare transport and scanned probe studies of our graphene films. This is not possible on the C-face, where the conduction channel is thought to be the bottom, highly doped graphene layer, and is not accessible by microscopy techniques. This work will therefore focus exclusively on monolayer graphene films grown on SiC(0001).

To date, monolayer graphene devices grown on SiC(0001) have been touted for their high mobilities and for applications to high frequency devices (transistors with cutoff frequencies >100 GHz have been demonstrated[55].) Fundamental questions remain, however, as to the nature of charge transport in epitaxial graphene grown on SiC. The role of the IFL in doping monolayer graphene films on SiC(0001) has been studied,[47] but it is not yet clear as to whether the model of charged-impurity scattering that applies to exfoliated flakes on SiO_2 may be easily adapted to the case of epitaxial growth.

Samples Used in this Work

The samples used in this work are predominantly monolayer graphene films grown on SiC(0001) in an Axitron/Epigress VP508 Hot-Wall CVD reactor tool by the Power Electronics group at the Naval Research Laboratory in Washington, DC. As noted briefly in the previous section, the methods for growing graphene on SiC have evolved somewhat since its step into the limelight in 2004.[7] Our samples were grown on semi-insulating, on-axis (+/-0.5^o) 4H- and 6H-SiC substrates of both silicon (0001) and carbon (000-1) crystal faces.[8] The SiC substrate was cut down from 50.8-mm and 76.2-mm wafer to 16- by 16-mm squares prior to being loaded in the reactor. To remove the scratches from mechanical polishing, the samples were first cleaned by an H_2 etch. The samples were annealed at 100 mbar in 80 standard liters per minute at 1600°C for 5-20 minutes.[8] The chamber was then flushed with argon prior to beginning the growth step. Samples grown in 2008 and the beginning of 2009 were grown in high vacuum. During growth, the reactor pressure would range from 10^{-4}-10^{-6} mbar while the temperature was held steady.[8] Early growth experiments were conducted at temperatures ranging from 1225 to 1700°C, but that range was quickly narrowed to $\approx$1500-1620°C.[8], [9] Growth times for samples grown in vacuum ranged from 10-120 minutes. After preliminary AFM imaging of both C-face and Si-face samples, I continued to work exclusively with Si-face samples because of the smooth surface and predominantly monolayer growth. As previously discussed, and as shown in Figure 21, the C-face of SiC produced samples that were many layers thick and covered with pleats and large topographical

variations. Growth on the Si-face, in contrast, preserved the step terraces of the original substrate. In addition to the smooth surface of graphene on SiC(0001) being better suited to microscopy techniques, it is worth noting that the conduction channel in C-face graphene devices is thought to be in the lower layers, near the substrate, and as such, a local probe measurement of the charge distribution in the surface would not provide insight into the transport characteristics of C-face film.
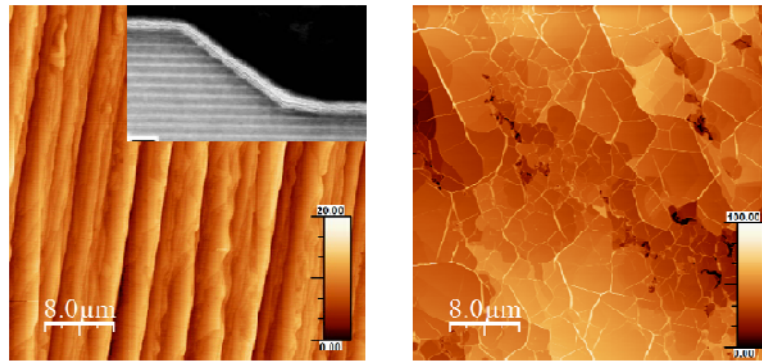
Figure 21: From reference [8]. AFM images of graphene grown on the Si-face (left) and C-face (right) of SiC. The vertical scale, in nm, shows the step bunching on the Si-face film and the presence of tall pleats on the C-face film. Left inset shows transmission electron microscopy image showing graphene and SiC layers.

Monolayer graphene regions on the SiC(0001) surface were identified by Raman spectroscopy. While work done at NRL included extensive Raman mapping, I performed a cursory check on many of our early samples to confirm the presence of a narrow, single Lorentzian 2D peak. Figure 22 shows a sample 2D Raman peak from a monolayer graphene sample grown on SiC(0001). The 2D peak is the definitive peak for monolayer identification, as the SiC background peaks obscure the D and G peaks to some extent.
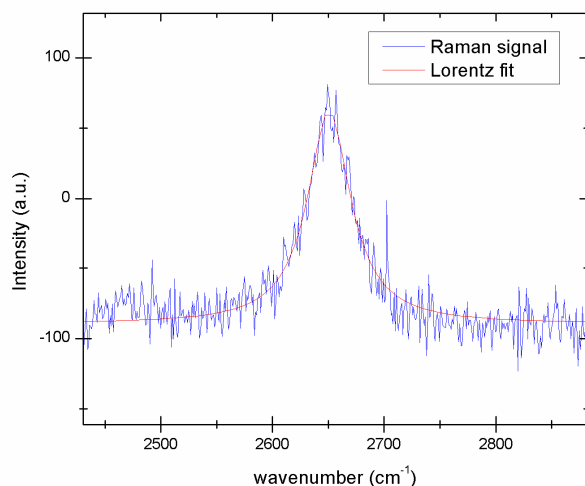
Figure 22: A sample 2D peak from a vacuum-grown graphene sample on SiC(0001). The 2D peak occurs at 2649 cm^{-1} and is fit to a Lorentzian with FWHM = 44 cm^{-1}.

The growth morphology and monolayer area percentage of graphene on SiC(0001) was greatly improved when, in 2009, growth methods began to incorporate an Ar overpressure during the Si sublimation part of the growth process. After chamber was flushed with argon to remove H$_2$ used in the etch process, an argon overpressure of 100-150 mbar was maintained during graphene growth. The argon over pressure had two notable effects on graphene growth: (1) the growth time had to be extended because the Si sublimation process was retarded, and (2) graphene growth did not begin until 1500°C on the C-face and 1550°C on the Si-face.[9] The growth temperature was optimized to 1620°C, and growth times were extended to be 90-150 minutes.[10] Because growth was slower, less bilayer and multi-layer nucleation occurred at step edges. The quality of the film was seen to rely on regular substrate steps with straight edges prior to growth. Figure 23 shows Nomarski optical images and AFM images of graphene grown on SiC(0001) in vacuum and argon.[9] While the surface morphology of the argon-grown sample is more regular than that of

the vacuum-grown sample, perfectly straight step edges would have produced a higher quality film. The rippling in the step edge as seen in Figure 23(d) effects the step bunching during growth.[11] The rippling SiC step terraces are a characteristic of the substrate as it is received from Cree (4H substrates) and II-VI (6H substrates) and cannot be corrected for during the H_2 etch process.
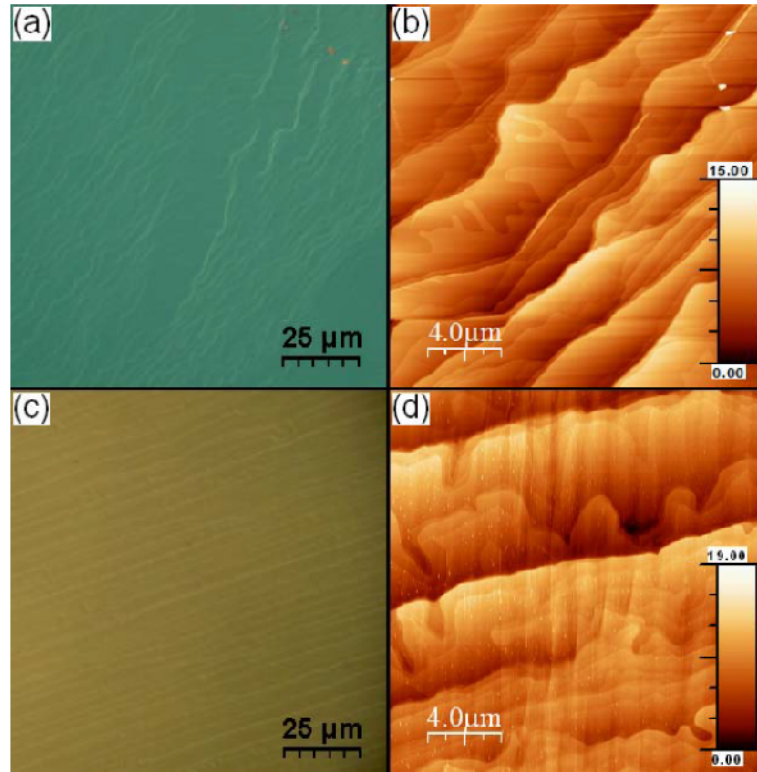
Figure 23: From reference [9]. Nomarski micrograph (a, c) and AFM image (b, d) of graphene grown on SiC(0001) in vacuum and in argon respectively.

The primary characterization work performed on the NRL samples in 2008 and 2009 was a series of transport measurements.[9], [12] On the 16- by 16-mm samples, van der Pauw measurements were performed to extract carrier density and mobility at 77 K and 300 K. Additionally, some samples were patterned by photolithography with an array of two-probe and four-probe ungated devices with

70

Au-evaporated contacts. The mask used for this patterning is shown in Figure 24. From this array of devices, a selection of 10-μm Hall crosses was measured also to extract mobility and carrier concentration. The Hall crosses were only measured at 300 K. The transport measurements were performed on both C-face and Si-face samples, with the C-face samples generally showing higher mobility. A selection of these measurements is shown in Figure 25. In total 44 van der Pauw measurements were performed on different samples, and 386 Hall crosses across several patterned samples were measured.
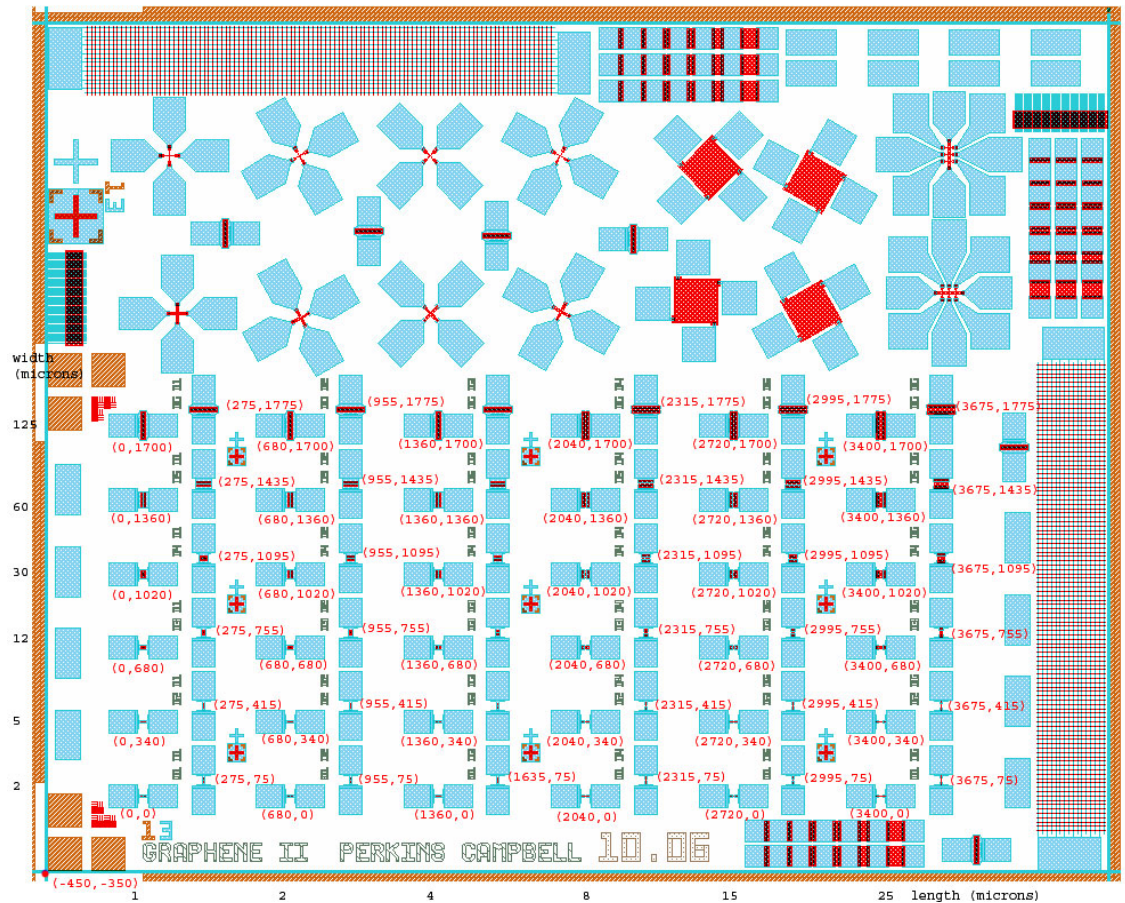
Figure 24: From NRL. The photolithography mask used to pattern graphene devices for transport measurements. The die shown here is 4- by 3-mm. Each 16- by 16-mm sample was patterned with 12

71

of these die. The eight 4-probe devices in the top left quadrant are the Hall crosses presented here. All

devices were ungated.
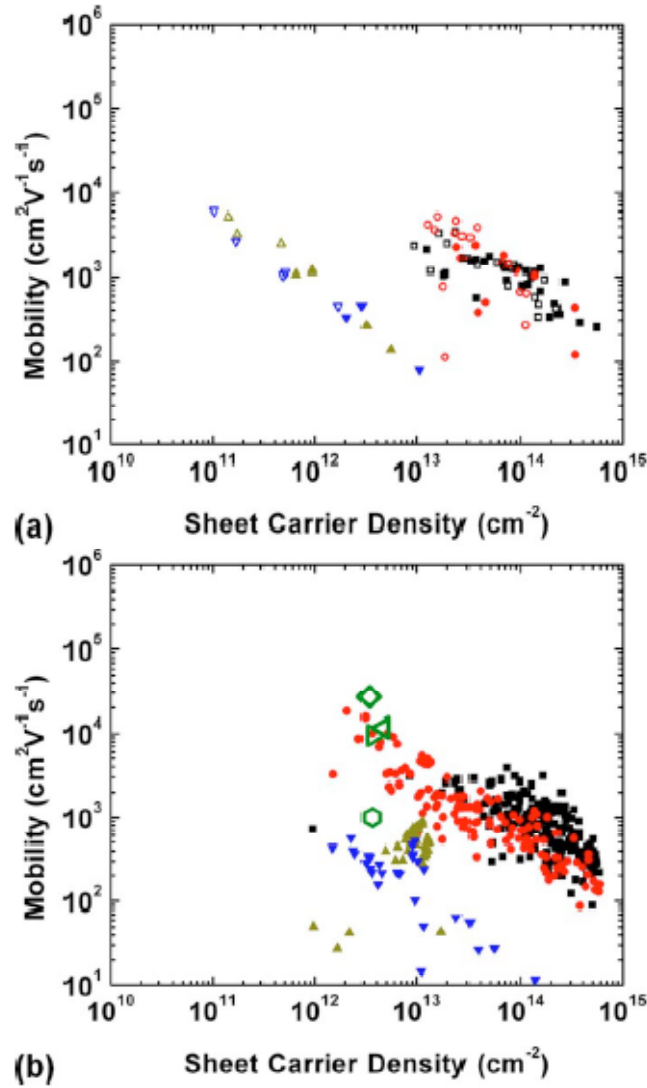
Figure 25: From reference [12]. (a) van der Pauw measurements conducted on 16- by 16-mm

samples and (b) Hall measurements conducted on 10-μm patterned crosses. In both graphs, red and

black symbols are for C-face samples. Red circles are p-type, and black squares are n-type. Green and

blue triangles are for Si-face samples. Green upward triangles are n-type ,and blue downward triangles

are p-type. Open symbols in panel (a) are devices measured at 77 K. The green samples in panel (b)

refer to samples from other references measure at low temperature. (◇ and ◁) Data from n-type C-

face samples measured at 1.4 K. ($\triangleright$) Data from n-type C-face samples at 180 K. The open green hexagon is for n-type Si-face samples measured at 4 K. See original reference for sources.

Of particular interest was the fact that the apparent Hall carrier density of the Si-face samples spans several orders of magnitude with both p-type (hole) and n-type (electron) doping. While this might have been explained by different growth conditions for the van der Pauw measurements on different samples, the large variation in sheet carrier density was also seen within sets of Hall crosses measured on the same sample. This suggests that the samples grown by NRL had a large variation in carrier concentration on micron length scales. This assumption is revisited in Chapter 4.

The application of KPM to graphene on SiC(0001) can provide insight into the nature of charge distribution and puddling in these films. Angle-resolved photoemission spectroscopy (ARPES)[56], [57], STM[58] and transport [59], [60]experiments have left the door open for a surface potential measurement such as KPM to properly characterize carrier concentration variation and possible puddling in epitaxial graphene. The remainder of this work will detail ambient and UHV KPM measurements that seek to address the problem of carrier concentration variation in epitaxial graphene with the aim of forming a model of graphene on SiC(0001) analogous to the model of charged-impurity scattering that describes graphene on SiO_2.

Chapter 4: Ambient KPM of Graphene on SiC(0001)

Introduction

      This chapter discusses ambient-environment surface potential measurements taken on a single 16- by 16-mm argon-grown Si-face epitaxial graphene sample using KPM to understand the macroscopic (i.e. between locations millimeters apart) variations in surface potential. The following chapters will discuss measurements on additional samples grown in vacuum and samples grown in argon, performed in ambient and in UHV, to understand the microscopic variations in surface potential due to differences in number of graphene layers, and within a layer type due to disorder. The work described in this chapter closely follows our manuscript published in *Applied Physics Letters*.[23]

      Growth on "Si-face" SiC (0001) has produced graphene films of highly uniform thickness, consisting almost exclusively of single-layer graphene (SLG), as evidenced by Raman spectroscopy [18], [44], [61] and the half-integer quantum Hall effect unique to SLG.[59], [60], [62], [63] However, questions remain as to the electronic uniformity of these films. Photoemission, [56], [57] STM, [58] and transport [59], [60] experiments report a wide range of Fermi energies $+90 \leq E_\mathrm{F} \leq +500$ meV relative to the charge-neutral point (CNP) for SLG on SiC (0001). A recent transport study [64] of a large number of similar ungated devices, both (16 mm)^2 chips and multiple (10 μm)^2 Hall crosses fabricated on the same chip, found large variations in carrier concentrations; electron and hole concentrations exceeding

3×10^{13} cm^{-2} were observed, corresponding to a standard deviation in Fermi energy $E_{F,rms} > 500$ meV.

Here I use ambient KPM to probe variations of surface potential, and hence Fermi energy, in SLG grown on 6H-SiC (0001). In contrast with the Hall-cross measurements,[64] KPM of multiple (10 μm)^2 areas shows an $E_{F,rms}$ of only 12 meV, indicating highly uniform doping on a macroscopic scale. Transport measurements on this sample and many nominally identical samples[64] reveal that the conductivity σ is clustered about a value of $\approx 4\ e^2/h$, which is consistent with the predicted minimum conductivity for graphene on SiC with a charged-impurity density n_{imp} on order of 10^{13} cm^{-2}. This impurity density is also consistent with the mobility on order 1000 cm^2/Vs observed for the few highest-conductivity samples with σ $>> 4\ e^2/h$ which are presumably doped outside the minimum conductivity regime. I conclude that our samples, and the majority of the samples in reference [11], are in the low-doped minimum conductivity regime, where the small Hall coefficient was misinterpreted to indicate a high carrier density and large doping variations.

Sample Growth and KPM Procedure

As discussed in more depth in the previous chapter, epitaxial growth of graphene on SiC has been performed in vacuum and argon environments at temperatures ranging from 1150°C to 1620°C.[43], [46], [65], [66] These conditions have produced graphene of varying quality, with early reports of many-layer graphitic growth on both the Si-face and C-face of SiC. Recently it has been shown that the use of a gas overpressure improves the quality of the graphene, allowing for higher

growth temperatures and slower growth times and producing a larger area percentage of SLG.[67], [68]   For this work, samples were grown on semi-insulating SiC substrates in argon at a pressure of 150 mbar at 1620°C for 90 minutes. Extensive Raman mapping of graphene surfaces shows that the majority of the sample surface is monolayer.[18], [69]

I performed KPM in ambient conditions using a Co/Cr-coated silicon tip with radius of curvature of $\approx$50 nm. As implemented on the Veeco D5000 scanning probe microscope, the Kelvin probe method uses the lifted tip to perform surface potential measurements interleaved with traditional tapping AFM. The surface potential measurement is performed by applying a ac voltage, $V_{tip,ac}$, with an amplitude of 1500 mV to the tip at resonance frequency, ω, with the tip lifted 2-20 nm above the graphene surface and the piezo driver turned off. The tip voltage V_{tip} is controlled by a feedback loop such that the amplitude of the tip at the ac frequency is zero; at this condition $eV_{tip} = W_{tip} - W_{surface}$, where W_{tip} and $W_{surface}$ are the work functions of surface and tip respectively. For graphene, I expect that $W_{surface} = W_{cnp} - E_F$, where W_{cnp} is the work function of charge-neutral graphene on SiC (0001). Hence V_{tip} directly tracks variation in E_F, and I take the standard deviation in V_{tip} to be equal to $E_{F,rms}/e$. A simple schematic of the KPM setup is shown in Figure 26.

Piezo is off, and instead tip oscillates due to V_{ac} applied at resonance to the tip
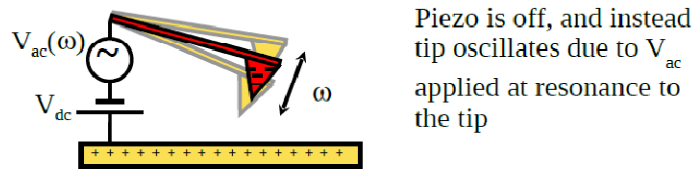
$$A \sim F_z(\omega) \sim (V_{dc} + \Delta\Phi)V_{ac}(\omega)$$

Figure 26: KPM is performed in ambient conditions by applying an ac voltage to a metal-coated cantilever in LiftMode™ . This cartoon provides a summary of ambient KPM as discussed in more detail in Chapter 2.

Ambient KPM of Graphene on Si-face SiC

To address the transport measurements of Tedesco et al., I focused this ambient KPM study on measuring the carrier concentration variation within monolayer regions. The argon-grown samples were especially well-suited to this, as I was able to measure many regions over a $(16 \text{ mm})^2$ sample without encountering multilayer regions or multiple surfaces. Over the course of this work, one sample in particular appeared to have the highest monolayer coverage, and was therefore most extensively measured. I performed KPM over seven $(10 \ \mu\text{m})^2$ regions of this $(16 \text{ mm})^2$ sample. All the data shown were taken with a single tip over a single session of data collection to eliminate any changes due to ambient doping variation, tip condition, temperature, etc. Figure 27(a) shows topography and Figure 27(b) shows the surface potential of a single $(10 \ \mu\text{m})^2$ scan that was typical of the majority of the sample surface; occasionally a clearly multimodal surface potential distribution was observed (see discussion below). A histogram of the potential observed over the scanned area is

shown in Figure 27(c). The potential variation over the surface is smooth with no

sharp steps correlated to topographical features or otherwise. Figure 28 shows the

mean and standard deviation of the surface potential for seven widely separated (10

μm)^2 scan areas over a 16- by 16-mm sample. For the data taken at these locations, I

found the standard deviation in peak position to be $E_{F,rms} = 12$ meV, with $E_{F,rms}$

within each individual (10 μm)^2 area ranging from 5 to 16 meV.
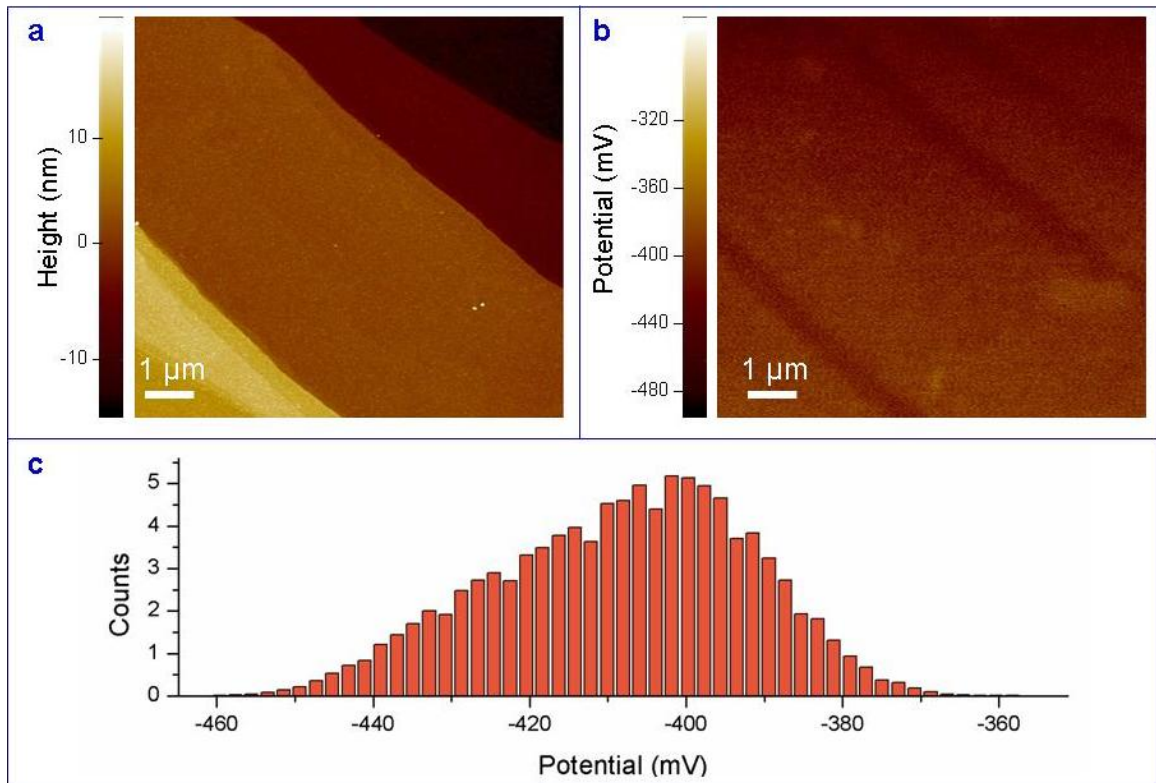
Figure 27: Topography (a) and surface potential (b) collected by KPM on a typical (10 μm)^2 region of

epitaxial graphene on SiC(0001). The dark regions in the surface potential data suggest there may be

bilayer regions along the edge of the SiC step. (c) Histogram of the potential data from (b).
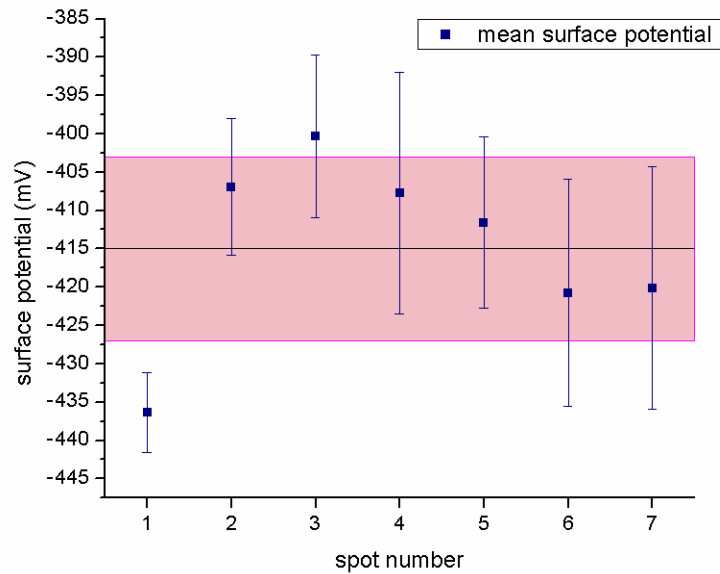
Figure 28: The mean surface potential of seven $(10 \ \mu m)^2$ regions and their standard deviation (error bars). The average and standard deviation over all locations are given by the black line and pink box respectively.

I occasionally observed multimodal surface potential images, with clearly defined regions of different surface potential with boundaries that correspond to topographic steps. I interpret the regions of different surface potentials as regions of different graphene layer thicknesses, e.g. IFL or bilayer grpahene, previously observed to have different surface potentials by Filleter et al.[70] The fact that I rarely observe these sharp step in surface potential suggests that our sample is homogeneous in layer number. However, in Figure 27(b) there appears to be regions of slightly lower surface potential near step edges. This could indicate the presence of BLG at the step edges, though the potential difference (≈25 meV) is much smaller than that observed between monolayer and bilayer graphene by Filleter et al. (≈100

79

meV).[70] A much more detailed look at layer distinction by KPM will be presented

in the next chapter. For now I simply note that that lack of well-defined steps further

supports the conclusion that our sample is almost entirely covered in monolayer

graphene.

Discussion

To extract information about the charge carrier concentration variation over the

graphene, I relate the peak positions variation plotted in Figure 28 to a variation in E_F,

and thus a variation in the carrier density of the sample. Near the charge neutrality

point, the carrier concentration variation is

$$\delta n = \left(E_{F,rms} / v_F \right)^2 / \pi, \tag{4.1}$$

where $v_F = 1.1 \times 10^8$ cm/s is the Fermi velocity in graphene,[71] and $\hbar$ is

Planck's constant. The macroscopic variation $E_{F,rms} = 12$ meV then corresponds to a

variation in carrier concentration of $\approx 10^{10}$ cm^{-2}. If the sample is highly doped, the

carrier concentration variation is approximated by:

$$\delta n = \frac{dn}{dE} E_{F,rms} = D(E) E_{F,rms} = \frac{2}{v_F} \sqrt{\frac{n}{\pi}} E_{F,rms} \tag{4.2}$$

where $D(E)$ is the density of states in graphene. For a doping of $n = 10^{13}$ cm^{-2}, the

variation $E_{F,rms} = 12$ meV would correspond to $\delta n = 5 \times 10^{11}$ cm^{-2}. The variations in

carrier density measured by KPM are therefore much smaller than the apparent

variations measured by Hall resistivity.

To address this discrepancy, I reexamined the transport data in Tedesco et al.

Figure 29(a) and (b) show transport data from nominally identical samples prepared

80

in argon, as well as from samples grown in vacuum and reported in reference 11,
replotted as sheet conductivity versus apparent Hall carrier density $1/R_H e$, where R_H is
the Hall coefficient of each sample. The conductivity is seen to cluster around a
value of ≈ 4 e^2/h over a wide range of carrier densities, with the exception of the
vacuum-grown 10 μm Hall crosses [Fig. 4(b)] where for an intermediate carrier
density range of (0.5-1.5) x 10^{13} cm^{-2} there is a cluster of points whose conductivities
rise rapidly with carrier density. The data point circled in red in Figure 29(a)
corresponds to the sample in this study (imaged in Figure 27), which has a
conductivity of 5.3 e^2/h and an apparent Hall carrier density of 2.8 x 10^{12} cm^{-2}.
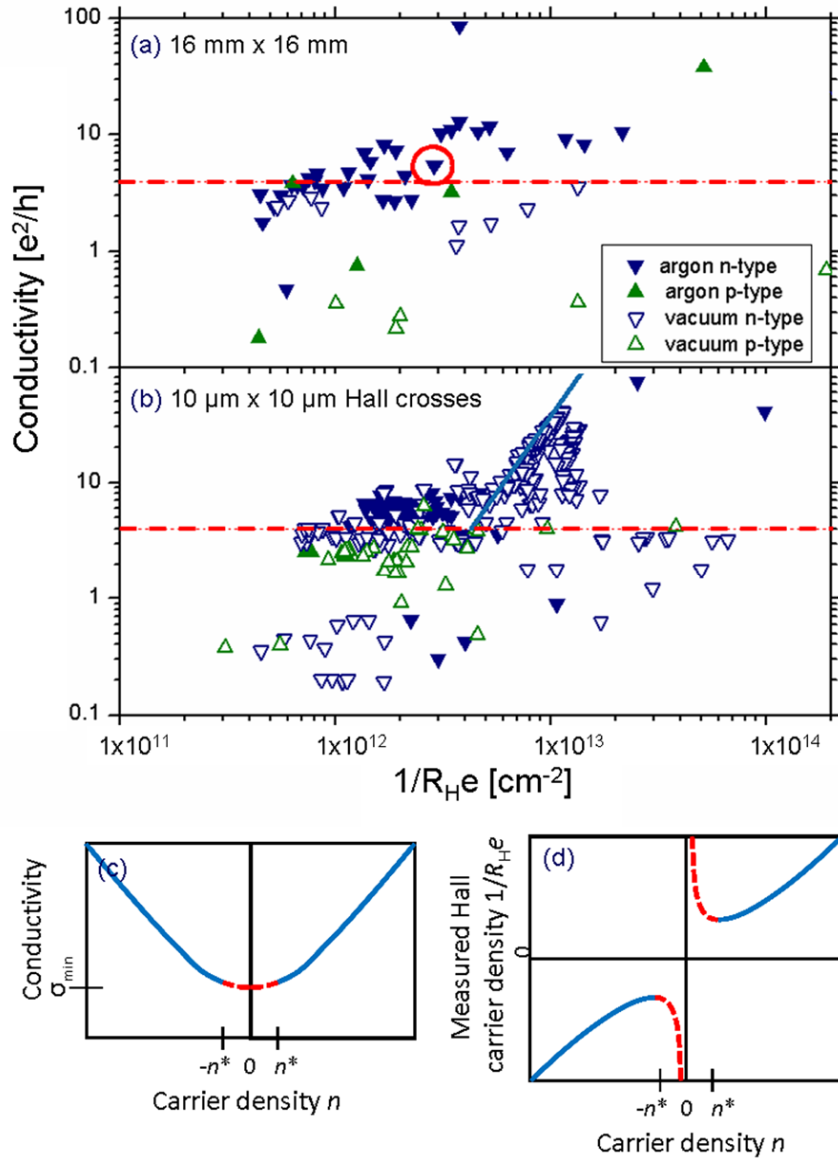
Figure 29: (a-b) Conductivity *vs*. apparent Hall carrier density for (a) 16- by 16-mm van der Pauw samples and (b) 10- by 10-µm Hall crosses of epitaxial graphene on SiC(0001), grown in argon (filled symbols) and vacuum (open symbols, Ref. 11). Upward-pointing triangles (green) are p-type and downward-pointing triangles (blue) are n-type. The data point circled in red represents the sample studied in this work. The dashed lines in (a) and (b) are at a conductivity of 3.5 e^2/h. The solid line in (b) is a guide to the eye, discussed in the text. (c-d) Conductivity (c) and apparent Hall carrier density $1/R_He$ (d) vs. average carrier density, *n*, within the self-consistent theory of Adam et al.

I interpret the data in Figure 29(a) and 2(b) within the self-consistent Boltzmann theory for graphene dominated by charged impurities put forth by Adam et al.[2] Figure 29(c) and (d) show qualitatively how σ and $1/R_He$ are expected to vary with average carrier density, n. At high n (solid blue lines), the conductivity is proportional to n (constant mobility) and the apparent Hall carrier density $1/R_He$ asymptotically approaches the average carrier density n. For $n < n^*$, graphene is dominated by electron and hole puddles with an *rms* carrier density n^* caused by the random charged impurity potential (red dashed lines). The conductivity is roughly constant around a minimum value σ_{min} of a few e^2/h, and the apparent Hall carrier density diverges as $n \to 0$. The apparent Hall carrier density always overestimates the average carrier density n and is never less than $\approx n^*$.

In Figure 29(b) the highest conductivity devices have $\sigma \approx 50$ e^2/h. I assume that these devices are in the high-density regime, and $n \approx 1/R_He \approx 10^{13}$ cm^{-2}, indicating a mobility $\mu \approx 1000$ cm^2/Vs. Applying the self-consistent theory of Adam, *et al* to the case of graphene on SiC ($\kappa \approx 9.6$), this corresponds to a charged impurity density of $n_{imp} \approx 8 \times 10^{12}$ cm^{-2}, $n^* \approx 8 \times 10^{11}$ cm^{-2}, and $\sigma_{min} \approx 3.5$ e^2/h.[2] I observe a large number of samples ($\approx 50\%$ of vacuum-grown, and nearly all argon-grown samples) with conductivities of ≈ 3.5 e^2/h, and $1/R_He > 7 \times 10^{11}$ cm$^{-2} \approx n^*$, and I conclude that these samples are in the low density minimum conductivity regime $n < n^* \approx 8 \times 10^{11}$ cm^{-2} and were previously mis-identified as being highly doped. This indicates that our SLG on SiC (0001) in ambient conditions has much lower doping than has been previously reported.

The very small spread in surface potential measured by KPM indicates a uniform doping level on a macroscopic scale. The transport data are inconsistent with a uniform, *high* doping level $n > n^*$: in this case one would expect all the samples to be outside the minimum conductivity regime, and display high conductivity and a narrowly distributed Hall carrier density which reflects the true carrier density. I conclude that the samples as probed by KPM are uniformly doped in the minimum conductivity regime $|n| < n^* \approx 8 \times 10^{11}$ cm^{-2}. I further conclude that the previously reported [11] large spread in carrier densities from Hall measurements on similar samples is an artifact of electron-hole puddling in the minimum conductivity regime.

Our conclusion is consistent with top-gated FETs fabricated on similar SLG on SiC (0001) showing low threshold voltages.[55] The microscopic fluctuations within a single surface potential image, $E_{F,rms} = 5\text{-}16$ meV are approximately one order of magnitude smaller than the expected electron-hole puddle fluctuations $E_{F,rms} = 110$ meV for $n^* \approx 8 \times 10^{11}$ cm^{-2}. I assume that the discrepancy results from the puddle correlation length of 10-20 nm being an order of magnitude smaller than the resolution of the Kelvin probe measurement. Chapter 5 discusses higher-resolution KPM measurements on similar samples in UHV. It is not clear why some previous experiments [4,8,9,11] on SLG on SiC(0001) show much higher doping. In Ref. 11, high doping was inferred incorrectly from Hall measurements in the minimum conductivity regime, but ARPES [56], [57] and some transport measurements performed in vacuum[59] clearly show highly and uniformly doped SLG ($n \approx 10^{13}$ cm^{-2}). It is possible that the samples in this work are low-doped as-grown in contrast to many previous reports due to different substrate chemical potentials. These

samples were prepared on semi-insulating SiC substrates produced by vanadium doping which creates deep levels, while other reports of graphene on semi-insulating SiC likely used SiC with compensated dopants.[72]   Also, at least one report in the literature showed very low doping (confirmed by quantum Hall effect) for graphene on Si-face semi-insulating SiC (though prepared at much higher temperature than the samples used here), indicating that low-doped as-grown samples are possible in principle.[60] These ideas will be discussed more in Chapters 5 and 6.

UHV measurements discussed in the following chapters will provide further insight into charge distribution in epitaxial graphene samples. In particular, the observation of discrete surface potential steps will be discussed in terms of diagnosing layer thickness and doping level. I also use KPM in UHV to investigate the nature of the IFL in contrast to the graphene monolayer. Kelvin probe results on the exposed IFL will allow for the mapping of the charge environment that exists under the as-grown graphene. These measurements will be compared again with the self-consistent theory for graphene transport and with similar measurements collected on bare SiO_2.

Chapter 5: Distinguishing Graphene Layers by KPM

Motivation

Ambient KPM has shown the surface potential of graphene to be smooth within monolayer regions, with a standard deviation in surface potential voltage of <16 meV (Chapter 4). While this low variation in surface potential was characteristic of the majority of the sample surface, surface potential steps were observed in some images corresponding to topographical steps in the AFM data. For the argon-grown sample discussed in the previous chapter, one of the eight 10- by 10-μm regions showed correlated surface potential and topographical steps. Figure 30 shows the stepped region. The area highlighted in the blue box of Figure 30(b) has been plotted in the histogram shown in Figure 30(c). The histogram shows a multimodal distribution corresponding to three distinct surface potentials. Previous work on exfoliated and epitaxial graphene samples points to these distinct surface potential regions as being due to different surfaces and graphene thicknesses.[70], [73], [74]
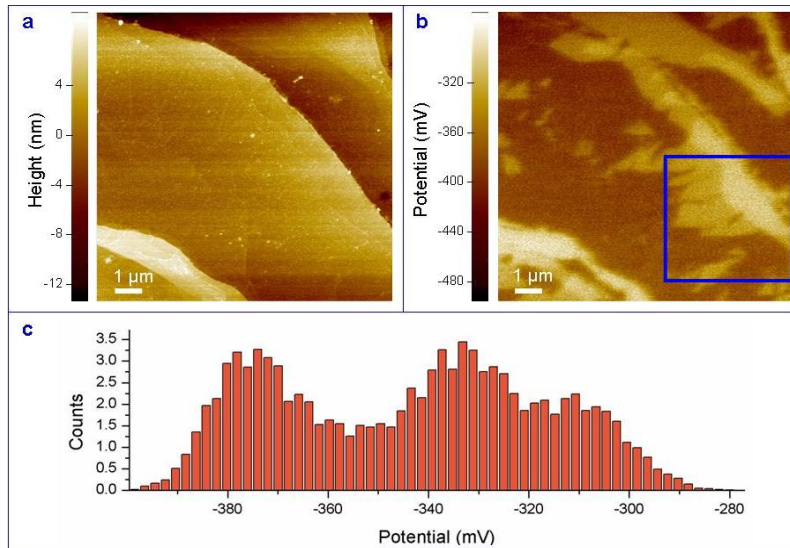
Figure 30: Topography (a) and surface potential (b) data collected by KPM on a rare (10 μm)2 region of epitaxial graphene on SiC(0001) which shows a multimodal potential distribution. (c) Histogram of the potential data in the area indicated by the blue box in (b).

In 2009, the Kim group published Kelvin probe data on SLG and BLG devices on Si/SiO$_2$ substrates patterned with Cr/Au contacts.[74] The paper noted that previous studies of the work function of graphene devices had concluded that it is close to the 4.6 eV value for graphite. The Kim group took the measurement a step further, exploiting the ability of the Si back gate to tune the carrier density in the graphene device. Measurements were performed in ambient and nitrogen environments using an interleaved KPM method as described in Chapter 2 with a lift height of 10-30 nm and an ac voltage to the tip of 300-500 mV applied off resonance at a frequency of 16 kHz. On several separate devices, the variation in graphene work function with change in gate voltage was measured on both SLG and BLG samples. Figure 31(a) plots the work function of a SLG device (in red, closed points) and of a BLG device (in blue, open points) vs. varying gate voltage. The gate

87

voltage here has been offset about the Dirac point for each device and is written as V_g – V_D. Since the quantity directly measured by KPM is the CPD between the tip and the samples, the work function of the sample is extracted to be:

$$W_{sample} \approx W_{tip} - e\Delta V_{CPD} \qquad (5.1)[74]$$

Here the W_{sample} is the sample work function, W_{tip} is the tip work function, and $e\Delta V_{CPD}$ is the measured CPD times the fundamental charge. To properly determine W_{sample}, the work function of the tip was calibrated on the gold electrodes of each device and found to be $W_{tip} = 4.82$ +/- 0.08 eV.[74]

Figure 31: (b) provides a cartoon of how the measurement of V_{CPD} is related to W_{sample} and to the Fermi energy E_F of the graphene. The measurement of W_{sample} with varying gate voltage then tracks the change in E_F with the change in carrier concentration, n.

The carrier density, n, is related to E_F through the momentum k_F by

$$\frac{k_F^2}{\pi} = n; \, k_F = \sqrt{\pi n}$$
$$E_F = h v_F k_F \qquad (5.2)$$
$$n = \frac{E_F^2}{\pi h^2 v_F^2},$$

where $v_F = \frac{1}{h}\frac{\partial E}{\partial k}$ is the Fermi velocity of 1.1 x 10^8 cm/s and $\quad$ is Planck's constant.

Equations 5.2 establish the relationship between E_F and n that is proportional to $n^{1/2}$. For the bilayer device, the energy dispersion relation is different and is given by:

$$E_{\pm}(k) = \pm\left[\sqrt{\left(v_{F,m}k\right)^2 + \frac{\gamma_1^2}{4}} - \frac{\gamma_1}{2}\right]. \qquad (5.3)$$

To rewrite $E_{\pm}(k)$ as $E_{\pm}(n)$, I first find k to be:

$$k = \frac{1}{v_F}\sqrt{\left(E_{\pm}(k)+\frac{\gamma_1}{2}\right)^2 - \left(\frac{\gamma_1}{2}\right)^2}$$ (5.4)

which produces the result

$$E_{\pm}(n) = \pm\left[\sqrt{\pi\left(hv_F\right)^2 n + \frac{\gamma_1^2}{4}} - \frac{\gamma_1}{2}\right]$$

$$n(E) = \frac{1}{\pi}\left(\frac{1}{hv_F}\right)^2\left[\left(E_{\pm}(k)+\frac{\gamma_1}{2}\right)^2 - \left(\frac{\gamma_1}{2}\right)^2\right].$$ (5.5)

where the constant $\gamma_1 = 0.39$ eV. If I take equation 1.5 in the high-momenta limit where $E(n)$ is much larger than γ_1, then the bilayer device follows a linear relation between n and E_F.

$$E = \frac{h^2 k^2}{2m^*} = \frac{h^2 v^2 n}{\gamma_1}$$

$$m^* = \frac{\gamma_1}{2v^2}.$$ (5.6)[75]

The data presented in Figure 31 follows these curves, with the SLG device data showing the predicted $n^{1/2}$ dependence and the BLG device data showing the predicted linear dependence.

Figure 31(c) shows the calculated change in Fermi energy with change in gate voltage extracted from the variation in W_{sample} shown in Figure 31(a). The work clearly shows the difference in the Fermi energy dependence of SLG and BLG devices on carrier concentration. The work also indicates a shift in the work function at charge neutrality, with BLG having a work function approximately 100 meV higher than that of SLG. However, this observation relies on proper calibration of the tip work function in each case. None of the devices allowed for the measurement of

adjacent SLG and BLG graphene regions on the same sample, which would have

provided a much more convincing measurement of the workfunction offset.
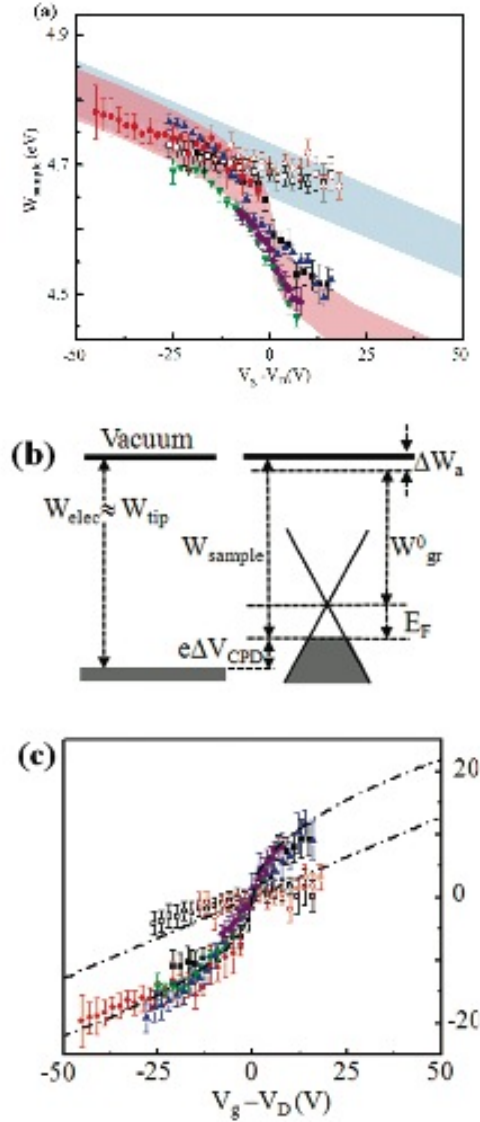
Figure 31: From reference [74]. (a) The change in the work function of the sample is plotted against

varying gate voltage for five devices. The three SLG devices are shown in the red area (closed

symbols). The two BLG devices are shown in the blue area (open symbols). The data are centered

about the point $V_g - V_D = 0$. (b) The Fermi energy and W_{sample} may be extracted from the measurement

of V_{CPD} and the calibration of the work function of the tip, W_{tip}. (c) From the measurement of W_{sample}, the change in Fermi energy with gate voltage may be calculated.

A 2008 paper by Filleter et al. addressed the measurement of adjacent SLG and BLG regions on epitaxial graphene with measurement of KPM by sample biasing in UHV.[70] Figure 32 shows sample topographical (a) and Kelvin probe (b) data from measurements collected on graphene grown on SiC(0001). Unlike the samples grown for our work, these graphene samples were grown in 1 atm of argon and then subjected to a 600°C anneal in UHV for surface cleaning.[70] The histogram in Figure 32(c) clearly shows three peaks in the measured CPD, while STM scans are used to confirm identification of the SLG (d) and BLG (e) regions. An important difference between all other KPM data presented here is that Filleter et al. followed the typical STM convention of applying the bias to the sample, i.e. the ac signal was sent through the SiC substrate. This means two things: (1) In Filleter et al. the contact potential difference is (apparently) defined as $e\Delta V_{CPD} = e\phi_{sample} - e\phi_{tip} = W_{tip} - W_{sample}$ in contrast to equation 5.1. The relative differences between SLG and BLG regions and SLG and IFL regions are flipped in sign or direction. To make sure it is unambiguous, I report my data as surface potential. To make a comparison to my data or the data from the Kim group, the data in Filleter et al. should be flipped in sign. (2) Because of the semi-insulating nature of the substrate, some information about surface potential features may be lost since the IFL may not respond to changes in the voltage applied to the sample. While the surface potential steps are clearly shown, variation within a layer may be under-resolved.
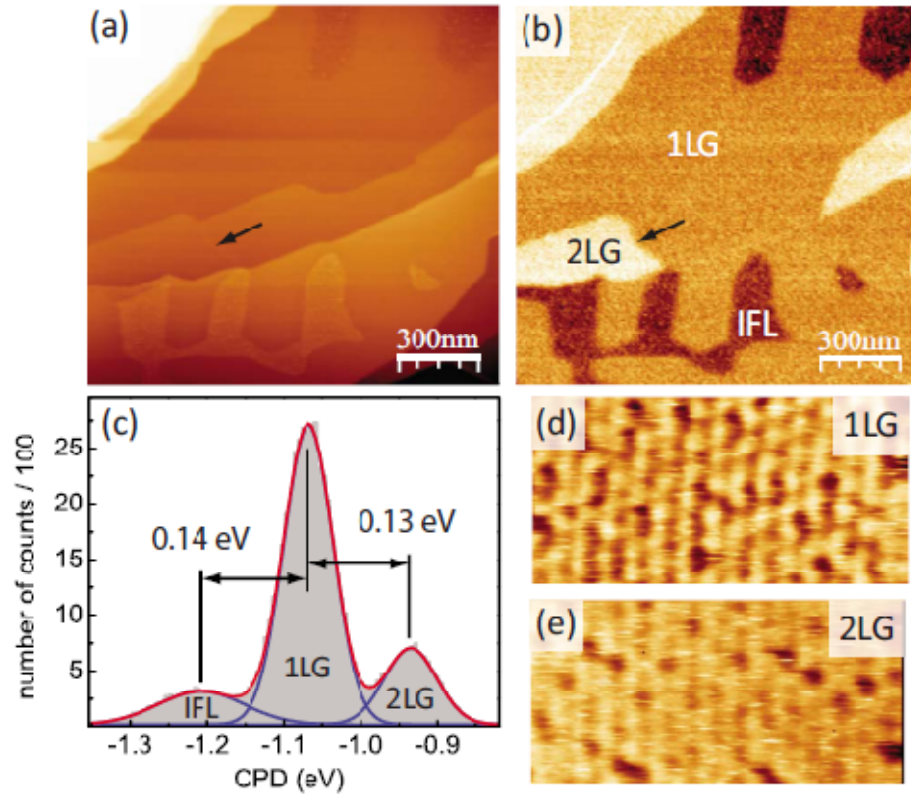
Figure 32: From reference [70]. (a) Topographical data and (b) KPM data of epitaxial graphene on SiC(0001). (c) A histogram of the potential data shows three distinct peaks tied to SLG, BLG, and IFL regions. (d) STM image of the SLG and (e) BLG regions. STM scale bar was not provided in original image.

Lacking the ability to vary the carrier concentration in the sample by applying a gate voltage, Filleter et al. relied on topographical step heights and STM images for layer identification. The identification of graphene layers by topographical steps on SiC depends on the particular growth characteristics in the surrounding region. To grow one 0.35-nm thick layer of graphene or IFL, the removal of three 0.25-nm SiC layers is necessary, placing the first layer of growth, the covalently-bonded IFL, 0.4 nm below the surrounding SiC. The true graphene monolayer sits another 0.4 nm

lower than this. However, if the sample surface has SiC steps near the graphene or IFL regions, then it is possible to have graphene sitting above neighboring IFL or SiC. Figure 33 shows seven possible cases for observing topographical steps between neighboring SiC, IFL, SLG, and BLG surfaces.[70] These figures do not represent all possible combinations but, rather, provide some examples of commonly occurring surface features.

Theo (nm)	0.25	0.085	0.335	0.17	0.335	0.085	0.415
Exp (nm)	0.24(3)	0.06(5)	0.34(2)	0.15(2)	0.33(2)	0.07(2)	0.43(2)

Figure 33: From reference [70]. The topographical steps measured in epitaxial graphene samples may be attributed to a variety of layer combinations. Here SiC layers (0.25 nm high) are shown as light grey, IFL (0.35 nm high) is shown as hashed, and graphene (0.35 nm high) is dark grey. Each column shows the step configuration, theoretical step height and measured step height for a particular combination of adjacent surfaces.

In the work by Yu et al., exfoliated SLG and BLG were positively identified by micro-Raman spectroscopy, and the variation in Fermi energy with carrier concentration agreed with the expectations for SLG and BLG.[74] I became aware of the work by Filleter et al. after considering the Yu paper and performing our own measurements on epitaxial samples. Because neither the Filleter samples nor our samples could be back-gated due to the semi-insulating nature of the SiC, and because performing Raman microscopy on the exact region probed by KPM is exceedingly difficult, I (and Filleter) could not directly distinguish SLG and BLG regions. Like Filleter, I relied on our knowledge of step heights in graphene growth on SiC to suggest layer identification on our own samples. The data present in Figure

30 were seen on an argon-grown sample in conjunction with the smooth monolayer data presented in Chapter 3; however, earlier samples grown in vacuum showed more surface variation.

Distinguishing Graphene Layers by Ambient KPM

I first performed ambient KPM on epitaxial graphene samples on SiC(0001) that were grown at the Naval Research Laboratory in a high-vacuum environment. These samples were not as uniform in growth as the argon-grown samples presented in the previous chapter. Figure 34 shows a $(10 \ \mu m)^2$ region of a vacuum-grown sample with typical surface morphology. While the surface potential data does not show variation across the SiC steps where graphene growth is continuous, several raised regions in the topographical data stand out in the Kelvin probe data as being at higher surface potential.
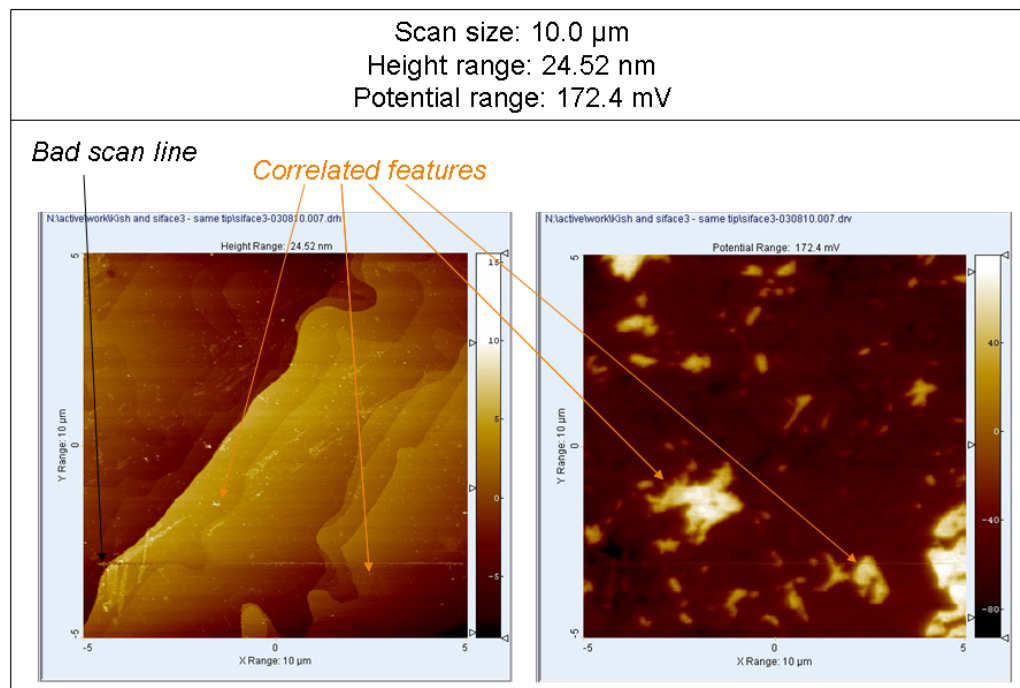
Figure 34: Topography (left) and surface potential (right) data for a $(10 \ \mu m)^2$ region of epitaxial graphene grown in vacuum on SiC(0001). The bright surface potential features are correlated to raised features in the topographical data.

One particular feature from the large-area scan was chosen for a higher-resolution scan, shown in Figure 35. The raised feature in the topographical data (Fig. 34a) corresponds to an area of surface potential feature (Fig. 34b) elevated ≈100 mV above the surrounding region. The majority of the sample (and presumably the majority of the image which is at low surface potential) is identified as SLG, since Raman spectroscopy confirms that the sample is predominantly SLG, and a simple multimeter check confirms that the sample was conducting (i.e. should consist of a continuous SLG area). A histogram of the entire region (Fig 34c, top) shows a bimodal distribution. By considering the high region (blue box) and the low region

(white box) from Figure 35(b) separately, one sees that there is a sharp single-moded surface potential distribution associated with each boxed region. The middle and bottom histograms in Figure 35(c) show the box of low surface potential and high surface potential, respectively.

A closer look at the topographical step in the form of an averaged step profile (Figure 35(d)) shows that the region of higher surface potential sits 0.19 nm above the surrounding region. The ≈ 100 mV surface potential step, combined with the positive topographical step from the surrounding region to the feature, leads us to believe that the feature corresponds to a region of IFL plus two bilayer SiC units surrounded by a region of IFL plus SLG. The height difference for this arrangement would nominally be 2×0.25 nm $- 0.335$ nm $= 0.165$ nm, close to the observed 0.19 nm. Given the direction of the surface potential step for the blue box feature, it is reasonable to conclude that this feature and the other surface potential features shown in the larger Figure 34 are regions of IFL or carbon buffer layer.
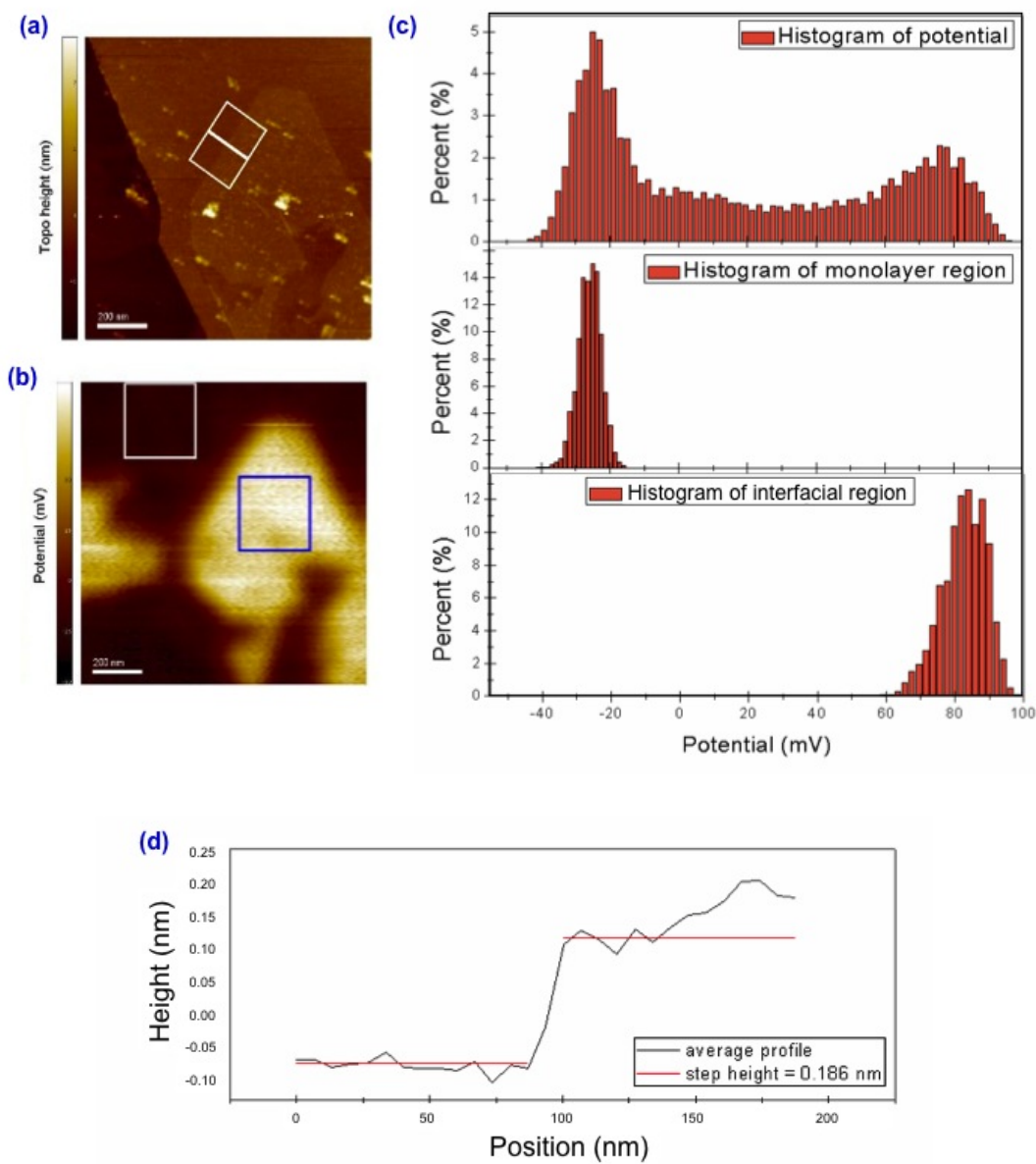
Figure 35: (a) Topography and (b) surface potential data from a zoomed-in region contained in Figure 34. (c) A histogram of the surface potential is shown to be bimodal (top). The middle histogram is taken from the region in the white box in figure (b), and the bottom histogram is generated from the region in the blue box. (d) An average profile of the step marked in (a) is shown to have a height of ≈0.19 nm.

Layer Identification by UHV KPM

Ambient KPM data collected on graphene samples grown in both vacuum and argon environments hint at the possibility of using KPM as a tool for distinguishing monolayer and bilayer graphene and IFL regions. Ambient results have shown clear steps between different graphene thicknesses and regions of exposed IFL, but our ability to draw conclusions about the height of these surface potential steps is hampered by limitations in the ambient technique. In particular, samples measured in air may be covered with adsorbates that affect the doping level, as discussed in Chapter 4.

Performing KPM in UHV provides many advantages to previous ambient measurements. In addition to eliminating the problem of adsorbates, the UHV setup allows for better lateral spatial resolution and potential resolution and improved topographical measurements. The improved lateral resolution is in part due to the purely incidental fact that the MikroMasch Pt/Ir coated Si cantilevers used in the UHV microscope have a smaller tip radius, ≈20 nm, than the Co/Cr coated Si cantilevers used in ambient, ≈20-50 nm. The topographical data, however, is further improved by the simultaneous running of the primary AFM loop and the Kelvin loop. While the topography loop operates at the ≈300 kHz resonance frequency of the tip, the Kelvin loop operates at 450 Hz. This limits scan rate to a speed slow enough to collect accurate surface potential data without attenuating the signal; however, it also ensures that the Kelvin loop is constantly nullifying the electrostatic component of the force on the tip, preventing work function or surface potential variations from

interfering with the accurate collection of topographical data in noncontact mode. This advantage was previously mentioned in Chapter 2.

I performed KPM in UHV on a JEOL combination AFM/STM with an attached scanning electron microscope (SEM). The SEM was used originally to check tip condition and perform simple x-y locating of the tip over the sample. I quickly discovered that at an accelerating voltage of 2.0 kV, the SEM could resolve detail and layer differences on the graphene samples. This result had previously been observed at the Naval Research Laboratory at 2.0 kV on an SEM with an in-lens detector. Our own JEOL XL-30 SEM operating at a typical lithography voltage of 30.0 kV could not resolve this detail. When I discovered the imaging capabilities of the UHV JEOL AFM/STM system, I quickly began correlating SEM contrast levels with Kelvin probe surface potential steps. The JEOL UHV system requires a long working distance SEM due to space constraints within the imaging chamber. Because of this, the images presented here are not as well resolved as SEM data collected at NRL. The Gaskill group at NRL has done further work to correlate their own SEM images with Raman mapping.
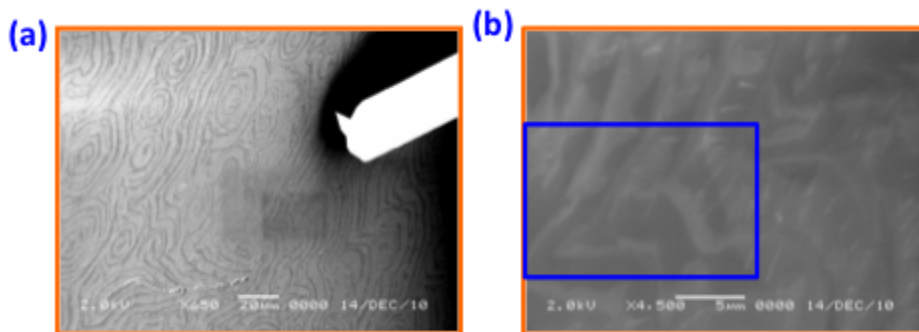
Figure 36: (a) and (b) both show SEM images collected at 2.0 kV with the SEM portion of the UHV JEOL AFM/STM. The image (a) shows charging of zoomed regions similar to that shown in (b). The

99

blue box in (b) shows a rough estimate of the location of the Kelvin probe data collected in Figure 36. The SEM image is tilted due to the angle of the SEM gun. The resolution is best possible for the long working distance of the tool.

Figure 37 shows two sets of AFM and KPM data with topographical and surface potential data taken simultaneously. The UHV KPM data clearly shows surface potential steps distinguishing SLG and BLG regions, as well as steps separating two different insulating layers (see below for evidence that these layers are insulating) that may represent different stages of growth of the IFL. Figure 37(a) and (b) show topographical and surface potential data collected over a small $(2\ \mu m)^2$ region that was later expanded to the $(5\ \mu m)^2$ area shown in Figure 37(c) and (d). While this clearly shows four different surface potentials, the insulating layers are further distinctly different from the graphene layers. The IFL, labeled as the two insulating layers "IL1" and "IL2," displays a unique roughness both in topographical data and surface potential data.
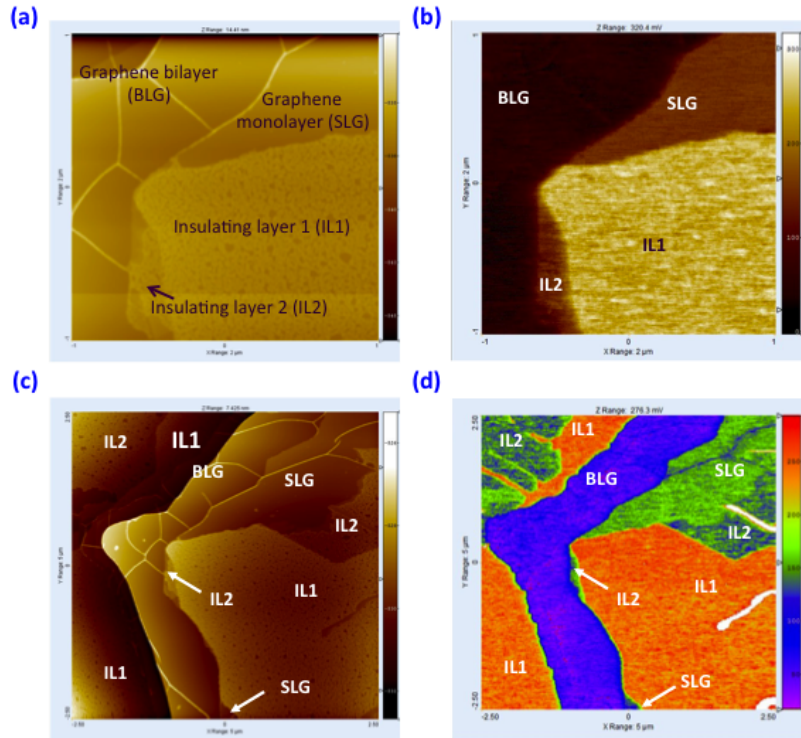
Figure 37: Topographical data (a) and surface potential data (b) collected over a $(2 \ \mu m)^2$ region. The scan region was expanded to the $(5 \ \mu m)^2$ region to show the topographical and surface potential data in (c) and (d). The four distinguishable surfaces are labeled as SLG, BLG, and insulating layer 1 and 2 (IL1 and IL2) that correspond to different surfaces within the interfacial layer.

Filleter et al. report a BLG to SLG contact potential difference of 130 meV, with the BLG having higher work function, i.e. lower surface potential (see Fig. 31; note that the convention for contact potential difference used by Filleter et al. means that the image in Fig. 31 is inverted in sign relative to my data). Figure 38 shows the average step profile across the monolayer and bilayer graphene regions labeled in Figure 37. The step in the white box in Figure 38(a) is displayed as the black line in Figure 38(b). The step height between the two regions is 100 mV, slightly smaller than 130 meV reported in Filleter et al. The discrepancy between the two

measurements is possibly ascribed to differences in doping between the two samples.
If the work function difference between SLG and BLG (120 meV) measured by Yu et
al. is correct, then a surface potential difference of 100-130 meV would correspond to
nearly undoped SLG and BLG, with small differences in doping ($< 10^{12}$ cm^{-2})
perhaps accounting for the difference between our measurement and that of Filleter et
al. I found the 100 mV step height shown in Figure 9 to be common to samples
measured in ambient conditions and in UHV.   Such doping differences could result
from different growth conditions; in Filleter et al. the sample was grown under
atmospheric pressure argon, while our samples were grown in 100 mbar argon.[70]
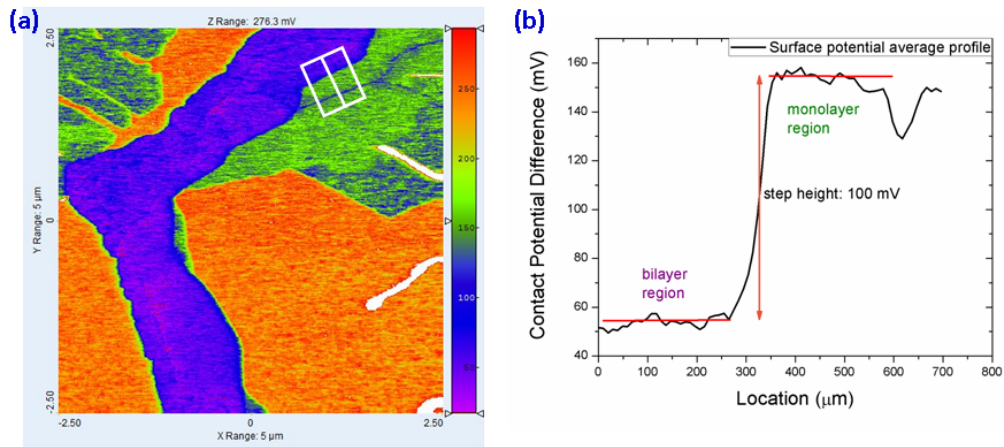
Figure 38: Surface potential data (a) with an SLG to BLG step highlighted in the white box, top right.
The average profile is taken, and the difference between the averages of the left- and right-hand sides
of the step is found to be 100.3 mV. In (b) the right-hand side of the curve is the monolayer, and the
left-hand side is the bilayer.

KPM Surface Potential Steps

Further insight into the $\approx$100 mV surface potential step between the IFL and graphene regions may be gathered from considering the work function difference between graphene and bare SiC. A comparison of the work function of grahene ($\approx$4.6 eV) [74] and the electron affinity for SiC ($\approx$3.7 eV for the 4H polytype) gives a potential drop of almost 1 eV.[76] It has been suggested that the observed shift of graphene's Fermi level by +300-400 meV as reported from ARPES is due to electron transfer from the IFL to graphene of 5.5x 10^{12} cm^{-2} to 1.5 x 10^{13} cm^{-2}.[47], [76], [77] If I consider the IFL/graphene potential step as being due to charge transfer from the IFL, then the potential field between the two layers may be calculated as:

$$\Delta V = \frac{ne^2 d}{\varepsilon_0}$$

(5.7)

where d is the distance between the IFL and the graphene, and n is the carrier concentration. Generally we take d to be 1 nm, putting the charged impurities directly below the graphene layer. For $n = 10^{13}$ cm^{-2}, I find that the potential step measured should be 600 mV.

Our measured 100 mV step corresponds instead to a charge density of $\approx$1.6 x 10^{12} cm^{-2} indicating that if the IFL is the origin of graphene doping, then the doping in our samples must be small. This is consistent with the conclusion drawn from the SLG-BLG step height, which suggests that our graphene grown on semi-insulating SiC may only be lightly doped or undoped, with $n \leq 10^{12}$ cm^{-2}. This is consistent with the conclusions of Chapter 4 where ambient-environment transport and KPM measurements indicated low doping.

The discrepancy between our results and ARPES measurements may come from the doping level of the SiC starting substrate. The large values of E_F (300-400 meV) seen in ARPES were measured on samples grown on n-doped epitaxial SiC layers.[76] It is unclear what substrate was used for the work of Filleter et al.; they reference another paper for the growth procedure which describes growth on both n-type and semi-insulating substrates. Our samples were prepared on semi-insulating SiC with lower Fermi energy. If the doping of graphene results from charge transfer from the SiC substrate, it is reasonable that SiC samples with higher or lower Fermi energy will result in higher or lower n-doping for graphene.

Quantifying UHV KPM Resolution

In the next chapter, I discuss UHV KPM measurements over distinct monolayer and IFL regions, with the aim of better understanding the charge environment under the graphene. To put the following results in the proper framework, I first quantify the lateral resolution of our surface potential measurement. In order to better resolve the fine features of the surface (particularly the IFL), I switched from a sample-biased mode of operation to a tip-biased mode. Sample biasing is the typical mode of operation for most STM systems and was the default configuration of the JEOL tool. However, because the SiC(0001) substrate is semi-insulating and the Kelvin probe measurement relies on an ac signal to measure surface potential variation, sample biasing may not provide the best optimization for performing UHV KPM. I switched to tip biasing so that the ac Kelvin signal would be directly applied to the tip, and thus the surface potential measurement would be a

more accurate surface measurement without smearing or attenuation due to poor conduction through the substrate. Figure 39 shows an image of UHV KPM after reconfiguring the JEOL microscope for tip biasing. The IFL in the right side on of each image shows sharper detail in both topographical and surface potential data. All KPM data presented hereafter was measured by tip biasing.
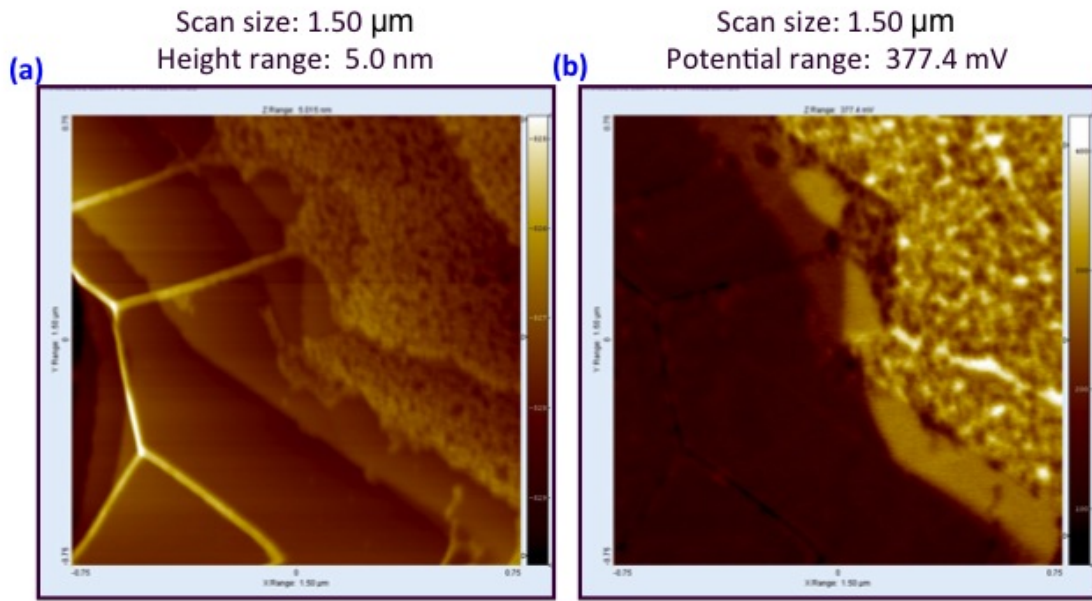
Figure 39: Topographical data (a) and surface potential data (b) taken with the JEOL UHV microscope reconfigured for tip biasing. Both images are $(1.50\ \mu m)^2$. Panel (a) has a z-range of 5 nm and panel (b) has a surface potential range of 377.4 mV.

To further analyze the quality of my UHV KPM data, I considered surface potential steps perpendicular to the fast scan direction of the tip. Figure 40 shows KPM data collected over a region with a surface potential step conveniently positioned parallel to the slow scan axis. An average profile of the step was taken for the region highlighted in the orange box in Figure 40(a). The profile was fit in IDL software to a step function convoluted with a Gaussian. The resulting fit function is

105

shown as the red line in Figure 40(c) superimposed over the average profile of the data, shown in black. The width of the Gaussian is calculated from the IDL fit to be 18.4 nm. This fit was performed for each tip used in the KPM study. All tips used were MikroMasch Ti/Pt-coated Si cantilevers with a calculated lateral resolution of 18-19 nm. I am able to achieve lateral surface potential resolution equal to lateral topographical resolution and comparable to the tip radius because the UHV KPM method allows for simultaneous topographical and surface potential data collection without lifting the tip.
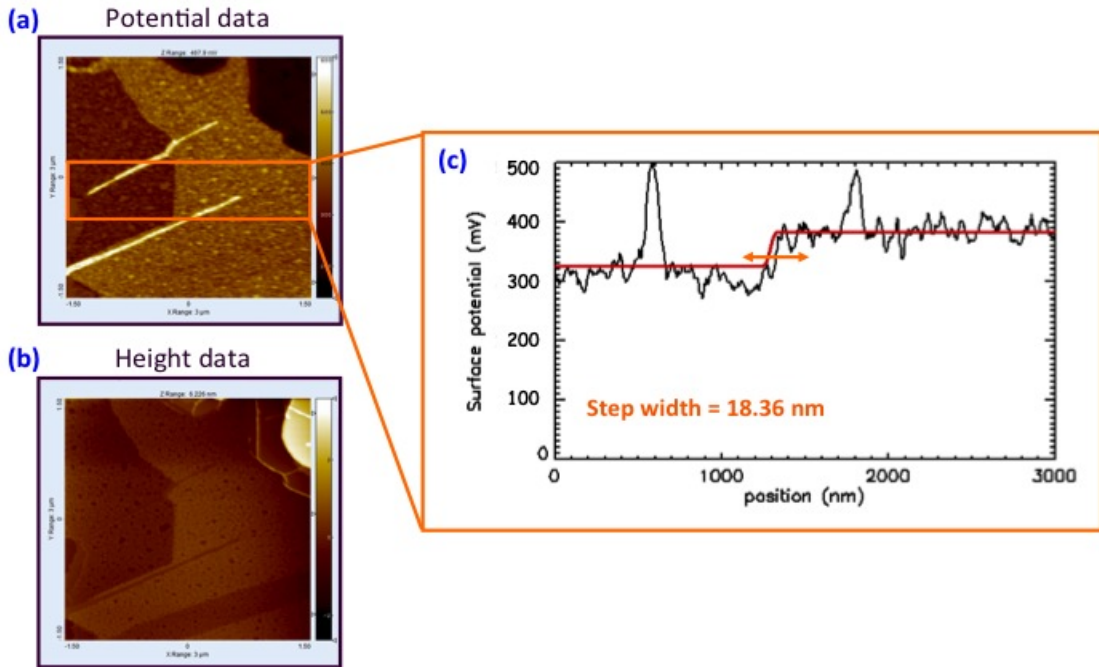
Figure 40: Surface potential data (a) and topographical data (b) collected using a MikroMasch Pt/Ir coated Si cantilever. The region in the orange box in (a) outlines a surface potential step between two distinct IFLs. The surface potential step is then averaged, and the step width of the average profile is shown in (c) to be ≈18.4 nm as calculated by the IDL software. The raised features in the surface potential image are likely bare SiC. They appear as peaks in the average of the potential scan lines, but as they do not occur at the potential step we analyzed, they do not effect the calculation of resolution.

106

The high lateral resolution in surface potential imaging indicates that KPM may be a useful technique for imaging electron-hole puddles in graphene. The correlation length for charge puddles in graphene on SiO_2 have been measured to be on the order of 20-30 nm. A clear measurement of charge puddles in graphene on SiC could provide insight into the nature of transport and charged-impurity scattering for epitaxial graphene on SiC(0001). The following chapter will explore in more detail the fine structure in the surface potential of SLG and IFL regions with the aim of imaging charge puddles and the potential disorder in the underlying carbon layer. The results of these measurements form a picture of charge distribution in epitaxial graphene analogous to the model for charged impurity scattering for exfoliated graphene flakes on SiO_2.

Chapter 6: UHV KPM of Microscopic Charge Inhomogeneity in SLG and IFL on SiC(0001)

Introduction

Chapter 5 presented data showing that UHV KPM could distinguish between SLG, BLG and two IFL surfaces both in surface texture (in the case of the graphene/IFL boundary) and in surface potential steps. I also found that UHV KPM techniques provide improved lateral resolution ($\approx$19 nm) compared to the ambient-environment KPM technique employed in Chapter 4. The spatial resolution is comparable to or lower than the size of electron-hole puddles observed by STM and STS on exfoliated graphene flakes on SiO_2.[3-5] The self-consistent theory for graphene with random charged impurity disorder[2] predicts that the correlation length ξ for the potential in graphene to scale as $\xi \propto \dfrac{\kappa_{av}^{2}}{\sqrt{n_{imp}}}$ where κ_{av} is the average dielectric constant of the substrate and vacuum, and n_{imp} is the impurity density.[78] For SiO_2, $\kappa_{av} = 2.5$, while for SiC, κ_{av} is 5.3, indicating a larger correlation length, i.e. larger electron-hole puddles, might be seen in epitaxial graphene on SiC. In this chapter I explore the microscopic potential inhomogeneity in SLG and IFL, with a focus on attempting to image charge puddles in SLG.

UHV KPM of Monolayer Graphene on SiC(0001)

Figure 41 shows a (500 nm)^2 region of monolayer graphene imaged by UHV KPM. This region was determined to be monolayer by both its dark contrast appearance in SEM relative to IFL regions and by its surface potential relative to neighboring bilayer regions. Figure 41(a) and (b) show the raw topographical and surface potential data respectively. In an attempt to highlight surface potential features in Figure 41(b), I low-pass filtered the data at a length of 60 nm; the result is shown in Figure 41 (c). The filtered image shows that there are persistent features in the potential that have a length scale on order 60 nm or larger. I present the low-pass filtered image for qualitative examination only; below I analyze the raw data using a one-dimensional (line-by line) autocorrelation function to extract the correlation length for the surface potential features.
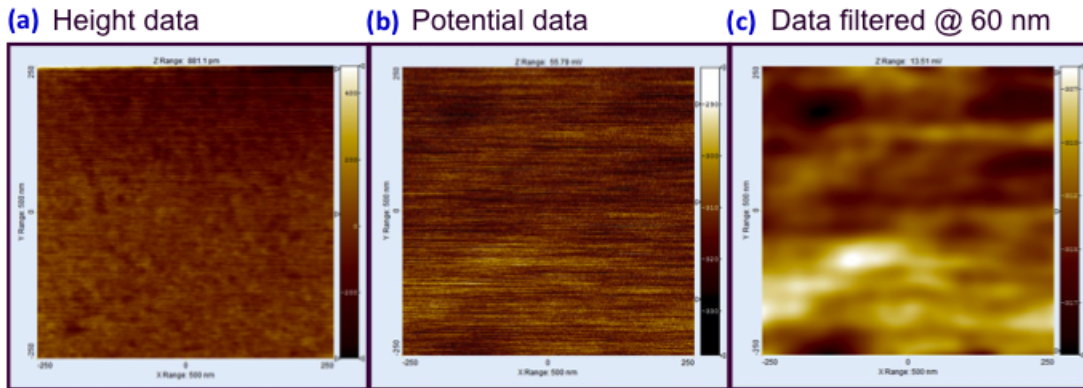
Figure 41: Topographical data (a) and surface potential data (b) for a (500 nm)^2 region of monolayer graphene. In (c) the surface potential data is low-pass filtered at 60 nm. This smoothing is done to enhance the hills and valleys visible in (b).

The autocorrelation function is a standard method for data analysis that is well suited to picking out features from the surface potential images collected by UHV KPM. My choice of a line-by-line autocorrelation function was made to eliminate the influence of the line-to-line rastering of several millivolts observable in Figure 41: (b). Specifically, the autocorrelation function compares the surface potential at a point p_N with the average surface potential of a pair of points a fixed distance r from p_N. This comparison is taken for all points along every line of data. To get the autocorrelation function value $C(R)$ for a line of data averaged at the length scale R, consider

$$V(p_N, r) = \langle V(r = p_N + R) \rangle$$

$$D(p_N, r) = V(p_N) \bullet V(p_N, r).$$

(6.1)

Here $V(p_N, r)$ is the average surface potential of two points in the line a distance R from the point p_N. I then compare the quantity $D(p_N, r)$ to the average potential of the data line to get the final result,

$$C(R) = \langle D(p_N, r) \rangle_N - \langle V(p_N)^2 \rangle_N,$$

(6.2)

where the second term describes the average of the square of the surface potential at every point. For the purposes of implementation and reasoning, another way to present the autocorrelation function is

$$D'(p_N, r) = (V(p_N) - \overline{V})(V(p_N, r) - \overline{V})$$

$$(6.3)$$

$$C(R) = \langle D'(p_N, r) \rangle_N.$$

Now the average surface potential, $\overline{V}$ of the data line is subtracted from both the surface potential at each point $V(p_N)$ and from the point pair average at distance R from p_N.

Averaging all $C(R)$ over a range of radii or length scales gives the full autocorrelation function output $C(r)$ of the data as a function of the radius, or point pair separation. By convention r is taken to be positive. However, below I plot $C(r)$ reflected about the y-axis to present a more intuitive picture of feature size and correlation length. The width of the autocorrelation function corresponds to the correlation length of the data. Figure 42 displays the output of the autocorrelation routine as applied to the data from Figure 41(b). The spike at the center of the curve is likely an artifact due to the pixelation of the image. The length scale limit was chosen based on the number of pixels in the data. For a 512 x 512 pixel image such as this one, the quality of the function output degraded as the distance between points in each pair past 256 pixels. After this limit, there were not enough complete sets of points for averaging. Large radii data is unphysical since correlations across these large distances ($r > 200$ nm or half the image size) are also suspect since there is limited data at large r.
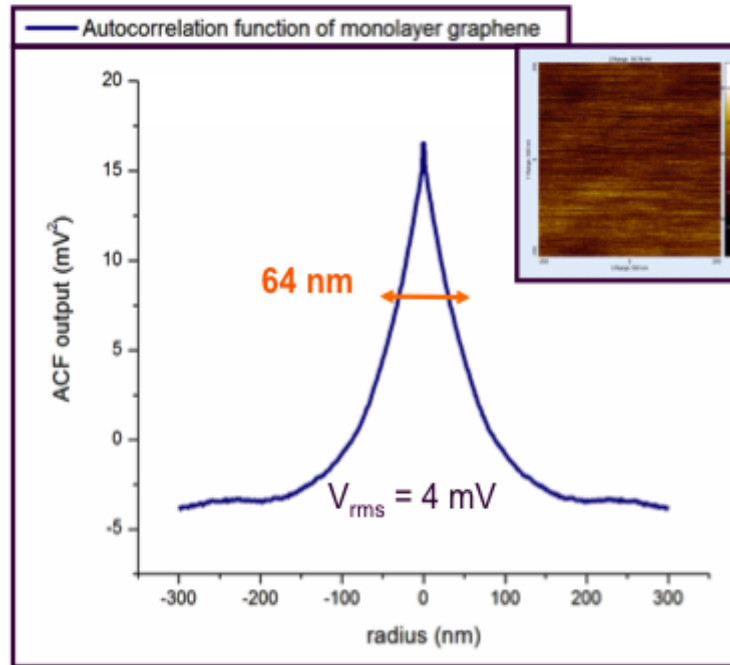
Figure 42: The autocorrelation function of the surface potential from Figure 40(b) (shown in inset). The function output is shown on the positive axis but is reflected onto the negative axis. The width of the autocorrelation function is 64 nm. The height of the function output has units $(mV)^2$ and corresponds to the variance of the voltage. The rms voltage, or surface potential variation is 4 mV.

The height of the autocorrelation function output at $r = 0$ represents the variance of the voltage $(V_{rms})^2$. For the region considered in Figures 40 and 41, V_{rms} is 4 mV. A similar number may be obtained from plotting the surface potential data in a histogram and extracting the width of the fit curve. As discussed earlier in Chapter 4, the rms voltage corresponds to a variation in carrier concentration over the sample surface. The value of 4 mV is even lower than the value measured in ambient (though here the spatial resolution is better), corresponding to an extremely low variation in carrier concentration.

112

The surface potential data for the IFL was measured to be substantially rougher than for the graphene monolayer. Figure 43(a) and (b) show height and surface potential data respectively for a region on the sample containing adjacent graphene (left) and IFL (right) regions. The boxed region in Figure 43(b) is shown magnified in Figure 43(c) and is the region over which the autocorrelation analysis was applied. The result of the analysis in shown in Figure 43(d). The height of the autocorrelation function output for the IFL is higher than for the graphene, giving a V_{rms} of 32 mV.
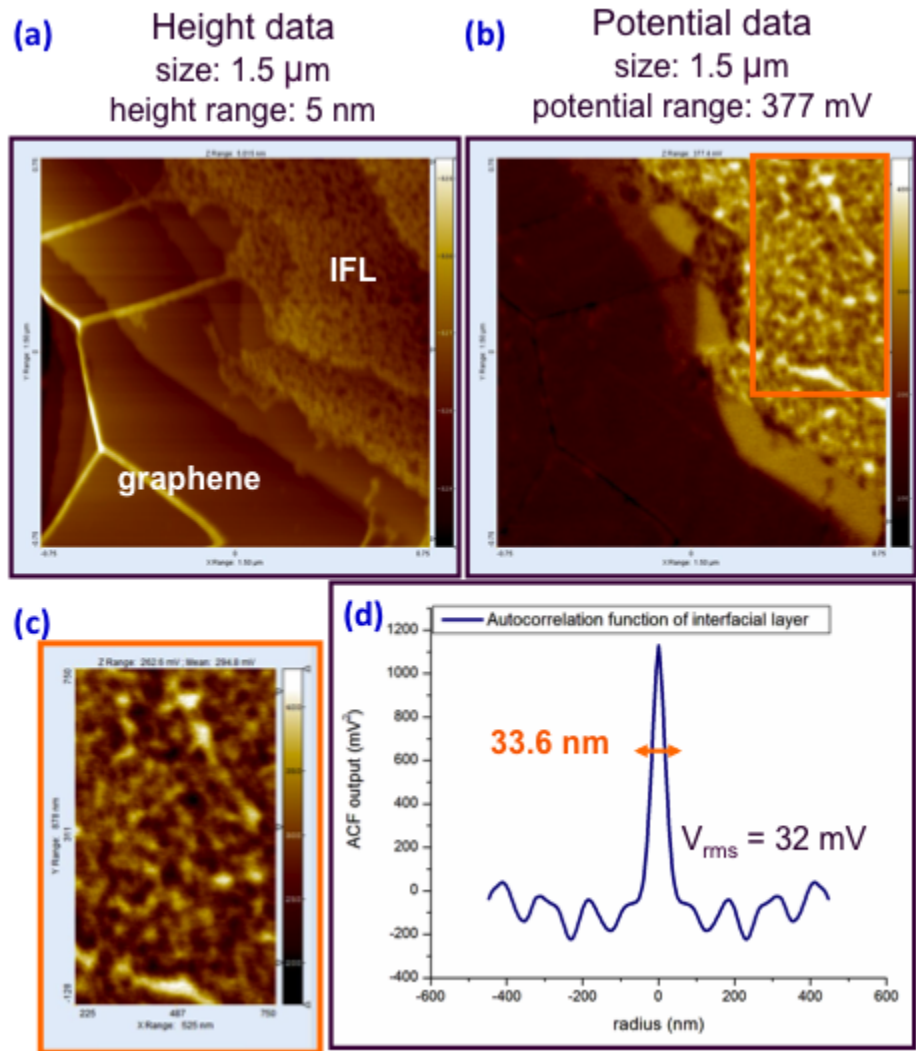
Figure 43: (a) and (b) show height and surface potential data for a region containing both graphene (left) and IFL (right) regions. The boxed region in (b) is shown again in (c) as the region over which the autocorrelation analysis was performed. The result of the autocorrelation function is shown in (d). The height of the autocorrelation function output at $r = 0$ corresponds to a V_{rms} of 32 mV, while the width of the peak gives a correlation length of ≈ 34 nm.

Analysis

To compare the measured C(r) to theory, I used the following expression describing the C(r) for randomly distributed charges located in a plane a distance d from the plane in which the potential is measured.

$$\frac{C(r)}{\left(\dfrac{e}{\kappa_{avg} r_{imp}}\right)^2} = \int_{1/l}^{\infty} \frac{2\pi q\, e^{-2qd}\, J_0(qr)}{\left(q\,\varepsilon(q)\right)^2}\, dq \qquad (6.4)$$

where $r_{imp} = \left(n_{imp}\right)^{-1/2}$, and $\varepsilon(q)$ is the relative dielectric function. For the case of random charges on an insulating substrate such as SiO_2 or the IFL on SiC, $\varepsilon(q) = 1$ (the dielectric effect is subsumed in the κ in the prefactor). In the case of graphene, $\varepsilon(q)$ is the screening function for graphene (see below). The quantity $J_0(qr)$ is the 0th spherical Bessel function and can be substituted as $\dfrac{sin(qr)}{qr}$.

The expression 6.4 has been successfully applied to the analysis of Kelvin probe data on SiO_2. I choose $d = 1$ nm as the distance between the substrate and impurities, an $l = 300$ nm as a long wavelength cutoff which described the cutoff of the 1/r Coulomb potential at long distances due to the presence of a gate electrode (groupnd plane) at a distance of 300 nm from the surface.. The dielectric constant κ is for the insulating substrate. UHV KPM data similar to the data presented here on the IFL was collected by Kristen Burson and Dr. Bill Cullen on SiO_2 substrates. Then C(r) was fit using equation 6.4. The autocorrelation function for SiO_2 is shown in Figure 44(a), and the fit is shown in Figure 44(b). The height of the autocorrelation function fit is scaled by the prefactor $\left(e/\kappa_{avg} r_{imp}\right)^2$.

Writing the amplitude of the fit function in terms of the above prefactor, I calculated n_{imp} to be ≈ 2.12 x 10^{11} cm^{-2}. This impurity concentration would limit the mobility in graphene on SiO$_2$ to ≈ 24000 cm^2/Vs, close to the maximum observed values.[79] The functional form of C(r) is also reasonable, indicating the random charged impurity model provides a good description of potential disorder on the SiO$_2$ substrate.
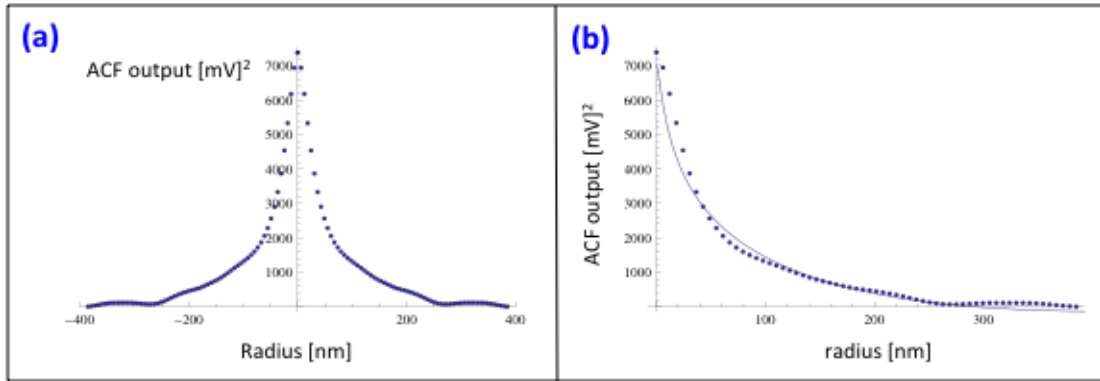
Figure 44: Experimental autocorrelation function (points) for UHV KPM data on SiO$_2$ collected at UMD by Kristen Burson and Dr. Bill Cullen. The line is a fit to equation 6.4.

I now turn to the autocorrelation function C(r) for the insulating IFL. To compare the model to the IFL data, I calculated the C(r) using equation 6.4 using values similar to those for impurities on SiO$_2$; the impurity distance d was kept at 1 nm (physically this would indicate surface charges located in the IFL, and d would reflect the tip-sample distance) and l was extended to 1000 nm to reflect the absence of a gate electrode imposing a long-distance cutoff. The dielectric constant for the IFL case was changed to $\kappa = 5.3$ for SiC. To fix the prefactor at a physically relevant value, n_{imp} was chosen as 1 x 10^{13} cm^{-2} in keeping with values quoted by ARPES for

116

the doping level in epitaxial graphene samples grown on SiC measured in UHV. This

assumes that the doping reported in epitaxial graphene is due to charge in the

substrate or IFL. The computed autocorrelation function curve for the IFL is shown

in Figure 45. The variance of the potential, given by C(r=0), is $\approx$250000 mV^2,

corresponding to a V_{rms} of approximately 500 mV, an order of magnitude larger than

the experimentally obtained value of 32 mV. Conversely, the measured V_{rms}

corresponds to $n_{imp} = 6.4$ x 10^{11} cm^{-2}. The model AC(r) is also significantly wider

than the experimental curve. The result indicates that (1) the impurity density on the

bare IFL is likely significantly (perhaps an order of magnitude) lower than 10^{13} cm^{-2},

and (2) the charges in the IFL are likely highly correlated, as reflected in the much

narrower experimental C(r) compared to the model. However, more work is needed

to quantitatively understand the experimental C(r).
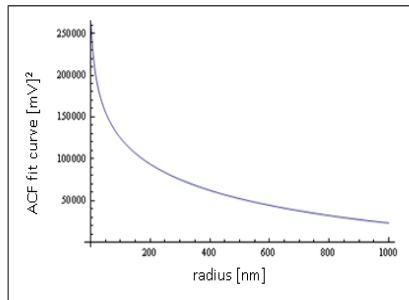
Figure 45: The computed autocorrelation function curve using equation 6.4, with values of $d = 1$ nm, $l = 1000$ nm, $\kappa = 5.3$, and $n_{imp} = 1$ x 10^{13} cm^{-2}.

     To understand the variations in potential seen on graphene on SiC, I consider

two cases. First, if the graphene is undoped, I might expect a variation in carrier

density $n* = 8$ x 10^{11} cm^{-2}, corresponding to $V_{rms} = 105$ mV, for an impurity density

$n_{imp} = 1$ x 10^{13} cm^{-2} as calculated in Chapter 4. The observed V_{rms} is 26 times smaller,

corresponding to $n* \approx 10^9$ cm^{-2}, comparable to values observed in ultra-clean suspended graphene, which I consider unlikely especially considering the low charge carrier mobilities measured in graphene on SiC.

If the graphene is considerably doped, the potential fluctuations will be smaller due to larger screening by the conduction carriers. I calculated this case using Eqn. 3.1, with $\varepsilon(q)$ changed to reflect the screening of the impurity charges by the graphene membrane. I used the RPA result for graphene's dielectric function [2], [80]:

$$\varepsilon(q) \quad = \quad \begin{cases} 1 + \dfrac{4 k_F r_s}{q} & for \quad q < 2k_F \\[2ex] 1 + \dfrac{\pi r_s}{2} & for \quad q > 2k_F \end{cases}$$

(6.5)

Here $r_s = 0.37$ is the fine structure constant for SiC, smaller than the value of 0.81 for SiO$_2$. I assumed a $k_F = 0.398$ nm^{-1} calculated from the Fermi energy of 300 mV for epitaxial graphene. This value of Fermi energy is consistent with the majority ARPES and transport measurements for epitaxial samples.[56], [57], [59], [60], [81] For this highly-doped case, it is reasonable to take k_F as a constant instead of doing a self-consistent calculation for k_F. As discussed in Chapter 4, there was some variation in the reporting of this number, but I consider 300-400 meV to be the most commonly agreed upon figure, corresponding to the widely reported 5 x 10^{12} cm^{-2} to 1 x 10^{13} cm^{-2} n-doping. The integral in equation 3.1 now takes the form:

$$C(r) \quad = \quad \left(\frac{e}{\kappa r_{imp}}\right)^2 \left[\int_{1/l}^{2k} \frac{2\pi q e^{-2qd} J_0(qr)}{\left(1 + \dfrac{4k_F r_s}{q}\right)^2 q^2} dq \quad + \int_{2k}^{\infty} \frac{2\pi q e^{-2qd} J_0(qr)}{\left(1 + \dfrac{\pi r_s}{2}\right)^2 q^2} dq \right]$$

(6.6)

118

In lieu of extracting an analytical form for the autocorrelation function fit curve for graphene over SiC, I instead calculate the magnitude of the curve at $r = 0$. Again I use the values $d = 1$ nm (here corresponding physically to the impurity-graphene spacing), $l = 1000$ nm, $n_{imp} = 10^{13}$ cm^{-2}. I then arrive at $V_{rms} = C(r=0)^{1/2} \approx 125$ mV. This again is much larger than the experimentally measured value of 4 mV. Since for high doping the variance of the potential scales proportionally to n_{imp}, I can identify the measured V_{rms} as corresponding to $n_{imp} = 3.2$ x 10^{11} cm^{-2}. This impurity level would correspond to a charge carrier mobility of 16000 cm^2/Vs, about an order of magnitude higher than observed for similar samples to ours. It would also require a mechanism to produce the high doping without corresponding high impurity level.

Chapter 7: Conclusions

Ambient electronic transport data (Chapter 4), and ambient (Chapter 4) and UHV (Chapter 5) Kelvin probe microscopy indicate that our epitaxial graphene samples grown on SiC(0001) are low-doped, at or near the minimum conductivity regime where electron-hole puddles dominate electronic transport. In Chapter 6 I discussed measurements of the microscopic potential fluctuations on graphene on SiC (as well as the bare carbon-rich interfacial layer of SiC), which should directly measure the potential depth and the spatial correlation of the electron-hole puddles. The autocorrelation functions of the potentials have widths of 32 and 64 nm respectively, and the rms potential variations are 32 and 4 mV respectively, for IFL and monolayer graphene. While the width of the autocorrelation function is plausible for the correlation length for electron-hole puddles in graphene on SiC, the observed small magnitude of the potential variations is difficult to explain.

As discussed in Chapter 6, the potential variations are inconsistent with a model of random charged impurities located in a plane near the surface of the SiC, a model which works well to describe the potential near the SiO_2 surface, and also describes well the electronic transport properties of graphene on the SiO_2. In the previous chapter I compared the surface potential variation measured on both the IFL and graphene to surface potential variations calculated from the expected charged impurity density of $n_{imp} = 10^{13}$ cm^{-2}; the observed potential variations in the IFL and graphene are 10 and 30 times smaller, respectively, than predicted. The results are

truly unanticipated and require a new understanding of potential disorder in substrate-bound graphene.

I can also look at the problem in reverse. Since the ambient KPM measurements and the measured surface potential step between monolayer and bilayer regions in UHV both strongly suggest that our samples are only lightly doped, it may be more meaningful to work from the UHV KPM measurements of the surface potential variations on the IFL and on monolayer graphene regions to estimate n_{imp} and n^* for out samples. The measured rms surface potential variation for the IFL, $V_{rms} = 32$ mV, corresponds to $n_{imp} = 5.7$ x 10^{10} cm^{-2} (here I used equation in 6.4 with $C(0)$ equal to $(V_{rms})^2$, $d = 1$ nm and $l = 1000$ nm). The self-consistent theory from Adam et al. further allows for the calculation of the predicted variation in carrier concentration, n^* from n_{imp} for the IFL.[2] From this, I find $n^* \approx 10^9$ cm^{-2}, which predicts a V_{rms} for the graphene of 16 mV. The experimental number from the graphene surface potential data was reported in the last chapter to be only 4 mV, considerably lower than predicted.

The ambient KPM measurements discussed in Chapter 4 point to the bulk of samples being lightly doped in the minimum conductivity regime with $n^* \approx 8$ x 10^{11} cm^{-2} and a minimum conductivity of 3.8 e^2/h. Other samples with $\mu \approx 1000$ cm^2/Vs have a larger range of measured Hall resistances and suggest a value of n_{imp} of ≈ 8 x 10^{12} cm^{-2}. The surface potential step of 100 mV between monolayer and bilayer graphene discussed in Chapter 5 is in good agreement with the work function difference measured by Yu et al, also supporting the conclusion that the samples are only lightly doped.[74]

There are several possibilities to explain the discrepancies in the observations of Chapters 4 and 5 and Chapter 6. The charged-impurity model relies on assumptions that may be incorrect. One assumption is that the charged impurities are located very near the graphene plane.   The impurities could instead be distributed throughout the SiC substrate. A variety of SiC substrates have been used for graphene growth, ranging from N-doped to semi-insulating. This may account for the wide range of N-doping reported for graphene samples grown on SiC(0001) of 90-500 meV; the doping could be due to donation of charge from bulk traps in the SiC, resulting in a depletion layer. Our samples were grown on semi-insulating samples, while n-doped graphene samples may have been grown on higher doped SiC substrates.

For the case of N-doped SiC substrates, the carrier density is reported to be between 3 x 10^{18} and 9 x 10^{18} cm^{-3}.[72] By considering the SiC/graphene surface potential step of ≈100 meV, I can estimate the depletion width in SiC as $l = \sqrt{\dfrac{2\kappa\varepsilon_0 U}{\rho e^2}}$ ≈ 4 nm, where U is the Schottky barrier height, $\kappa = 9.6$, and $\rho \approx$ 6 x 10^{18} cm^{-3} is the bulk doping. For the semi-insulating substrates used for our samples, the bulk doping is much lower, ≈ 10^8-10^{12} cm^{-3}, producing much longer depletion lengths.[72] While the calculation suggests depletion lengths for semi-insulating substrates ≥1 μm, the physical meaning of this is unclear. Qualitatively, however, longer depletion lengths, corresponding to a deeper distribution of charged impurities in the substrate produce smoother surface potential variations, similar to what is experimentally observed. If I calculate *C(0)* again for epitaxial graphene on SiC replacing *d* with a value of 50 nm, the predicted V_{rms} drops to 4 mV for an impurity concentration of 5 x 10^{12} cm^{-2}; hence

122

remote impurities could easily explain the small potential fluctuations observed on graphene on SiC. Moving the impurities farther from the graphene plane has a small effect on the mobility (at least in the regime where $dn^{1/2} \leq 1$; d is the impurity-graphene separation) but a much larger effect on the electron-hole puddle carrier density.[2]

A second possibility is that the charged impurities are located in a plane near the graphene but are correlated. If the impurities are located in the interfacial layer itself, then the doping is established through electrochemical equilibrium between the IFL charge traps and the graphene. A comparison may be made between the bulk doping necessary and equivalent surface charge density needed to produce the frequently-measured Fermi energy of 400 meV. It has been shown that a surface density of 10^{13} cm^{-2} surface charges at the graphene interface replicates the Fermi energy and band structure of a substrate with a 10^{19} cm^{-3} bulk doping.[82] This alternate explanation allows for the case of doping in graphene being caused by bulk impurities (e.g. nitrogen) buried in the substrates, surface impurities, or some combination of the two. For the surface case, it may be that the Si dangling bond of the substrate at the IFL/substrate interface produces a density of charge traps larger than the impurity density, and the partially-filled charge trap population may be correlated through Coulomb repulsion among the traps. Some theoretical and experimental work has been done on correlated impurities in graphene.[83], [84] The experimental results suggest that the puddles carrier density is significantly reduced by impurity correlations.[83]

A last possibility is that IFL is highly polarizable, leading to a much higher effective dielectric constant for the IFL/SiC substrate than expected. This is consistent with recent experimental work by Walter et al using ARPES to examine plasmarons in graphene on SiC substrates which compared graphene/IFL/SiC(0001) to graphene that was decoupled from the underlying substrate by a variety of intercalation methods.[85] The ARPES spectra collected on graphene/IFL/SiC samples (similar to those used in this work) showed a kink near the Dirac point with small hole-plasmon band separation. From these spectra, Walter et al found a graphene fine structure constant $\alpha \approx 0.1$ and $\kappa = 22$ for graphene on IFL, compared to our assumed value of $\alpha = 0.36$ calculated from a substrate κ of 9.6, or effective $\kappa = 5.3$. This supports the claim of higher dielectric screening due to the high polarizability of the IFL, where the origin of this polarizability again lies with the dangling Si bonds in the IFL. The electron-hole puddle carrier density scales as α^2, so a smaller fine structure constant due to a more-polarizable IFL could explain the smaller electron-hole puddle carrier density.

The above suggestions all point to the IFL as playing a strong role in altering the dielectric environment of epitaxial graphene from the simple case of the film on a bare SiC substrate. Although several explanations have been offered for the observed data, more measurements are needed to precisely determine the doping of graphene grown on semi-insulating SiC(0001). Currently being pursued, STS measurements of graphene could provide a doping value for epitaxial samples by directly measuring the Fermi energy.[86] A better understanding of graphene doping by a direct comparison of samples grown by the same methods on SiC substrates of different N-

doping would greatly illuminate the situation. These samples could be easily

compared again with KPM and STS without device processing. Finally, UHV

transport experiments could also be valuable, both on clean samples to determine

doping, and on K-dosed or otherwise perturbed samples to better understand the

smooth surface potential distribution measured on clean graphene by UHV KPM.

Until further steps have been taken, the lack of puddles in the UHV surface potential

data remains a surprising result in an otherwise cohesive picture of lightly doped

epitaxial graphene samples on SiC(0001).

Bibliography

[1]   A. K. Geim and K. S. Novoselov, "The rise of graphene," *Nat Mater*, vol. 6, no. 3, pp. 183-191, Mar. 2007.

[2]   S. Adam, E. H. Hwang, V. M. Galitski, and S. Das Sarma, "A Self-consistent theory for graphene transport," *PNAS*, vol. 104, no. 47, pp. 18392–18397, 2007.

[3]   A. Deshpande, W. Bao, F. Miao, C. N. Lau, and B. J. LeRoy, "Spatially resolved spectroscopy of monolayer graphene on SiO2," *Physical Review B*, vol. 79, no. 20, May. 2009.

[4]   Y. Zhang, V. W. Brar, C. Girit, A. Zettl, and M. F. Crommie, "Origin of spatial charge inhomogeneity in graphene," *Nat Phys*, vol. 5, no. 10, pp. 722-726, Oct. 2009.

[5]   J. Martin et al., "Observation of electron–hole puddles in graphene using a scanning single-electron transistor," *Nature Physics*, vol. 4, pp. 144-148, 2008.

[6]   P. R. Wallace, "The Band Theory of Graphite," *Physical Review*, vol. 71, no. 9, pp. 622-634, May. 1947.

[7]   T. Ando, T. Nakanishi, and R. Saito, "Berry's Phase and Absence of Back Scattering in Carbon Nanotubes," *Journal of the Physics Society Japan*, vol. 67, no. 8, pp. 2857-2862, Aug. 1998.

[8]   K. Nomura and A. H. MacDonald, "Quantum Transport of Massless Dirac Fermions," *Physical Review Letters*, vol. 98, no. 7, pp. 076602-4, Feb. 2007.

[9]   J. C. Slonczewski and P. R. Weiss, "Band Structure of Graphite," *Physical Review*, vol. 109, no. 2, p. 272, Jan. 1958.

[10] Y. G. Semenov, K. W. Kim, and J. M. Zavada, "Spin field effect transistor with a graphene channel," *Applied Physics Letters*, vol. 91, no. 15, p. 153105, 2007.

[11] Z. H. Ni et al., "Graphene Thickness Determination Using Reflection and Contrast Spectroscopy," *Nano Letters*, vol. 7, no. 9, pp. 2758-2763, 2007.

[12] P. Blake et al., "Making graphene visible," *Applied Physics Letters*, vol. 91, no. 6, p. 063124, 2007.

[13] S. Roddaro, P. Pingue, V. Piazza, V. Pellegrini, and F. Beltram, "The Optical Visibility of Graphene: Interference Colors of Ultrathin Graphite on SiO2," *Nano Letters*, vol. 7, no. 9, pp. 2707-2710, 2007.

[14] J.-H. Chen et al., "Diffusive charge transport in graphene on SiO2," *Solid State Communications*, Feb. 2009.

[15] C. Jang, S. Adam, J.-H. Chen, E. D. Williams, S. Das Sarma, and M. S. Fuhrer, "Tuning the effective fine structure constant in graphene," *Physical Review Letters*, vol. 101, p. 146805, Oct. 2008.

[16] J.-H. Chen, C. Jang, S. Adam, M. Fuhrer, E. D. Williams, and M. Ishigami, "Charged impurity scattering in graphene.pdf," *Nature Physics*, vol. 4, pp. 377-380, May. 2008.

[17] S. Adam, E. H. Hwang, and S. D. Sarma, "Scattering mechanisms and Boltzmann transport in graphene," *0708.0404*, Aug. 2007.

[18] J. A. Robinson et al., "Correlating Raman Spectral Signatures with Carrier Mobility in Epitaxial Graphene: A Guide to Achieving High Mobility on the Wafer Scale," *Nano Letters*, vol. 9, no. 8, pp. 2873-2876, 2009.

[19] S. J. Chae et al., "Synthesis of Large-Area Graphene Layers on Poly-Nickel Substate by Chemical Vapor Deposition: Wrinkle Formation," *Advanced Materials*, vol. 21, pp. 1–6, 2009.

[20] R. Decker et al., "Local Electronic Properties of Graphene on a BN Substrate via Scanning Tunneling Microscopy," *Nano Letters*, vol. 11, no. 6, pp. 2291-2295, Jun. 2011.

[21] J. Xue et al., "Scanning tunnelling microscopy and spectroscopy of ultra-flat graphene on hexagonal boron nitride," *Nat Mater*, vol. 10, no. 4, pp. 282-285, Apr. 2011.

[22] E. Rossi and S. Das Sarma, "Ground State of Graphene in the Presence of Random Charged Impurities," *Physical Review Letters*, vol. 101, no. 16, p. 166803, Oct. 2008.

[23] A. E. Curtin, M. S. Fuhrer, J. L. Tedesco, R. L. Myers-Ward, C. R. Eddy, and D. K. Gaskill, "Kelvin probe microscopy and electronic transport in graphene on SiC(0001) in the minimum conductivity regime," *Applied Physics Letters*, vol. 98, no. 24, p. 243111, 2011.

[24] G. Binnig, C. F. Quate, and C. Gerber, "Atomic Force Microscope," *Physical Review Letters*, vol. 56, no. 9, p. 930, Mar. 1986.

[25] F. J. Giessibl, "Advances in atomic force microscopy," *Reviews of Modern Physics*, vol. 75, no. 3, p. 949, Jul. 2003.

[26] D. Rugar and P. Hansma, "Atomic Force Microscopy," *Physics Today*, vol. 43, no. 10, p. 23, 1990.

[27] Y. Martin, C. C. Williams, and H. K. Wickramasinghe, "Atomic force microscope–force mapping and profiling on a sub 100-A   scale," *Journal of Applied Physics*, vol. 61, no. 10, p. 4723, 1987.

[28] M. Nonnenmacher, M. P. O'Boyle, and H. K. Wickramasinghe, "Kelvin probe force microscopy," *Applied Physics Letters*, vol. 58, no. 25, p. 2921, 1991.

[29] J. M. R. Weaver, "High resolution atomic force microscopy potentiometry," *Journal of Vacuum Science & Technology B: Microelectronics and Nanometer Structures*, vol. 9, no. 3, p. 1559, May. 1991.

[30] V. D. Wheeler, L. O. Nyakiti, and D. K. Gaskill, "private communications 4/2010 - 3/2011." .

[31] C. Oshima and A. Nagashima, "Ultra-thin epitaxial films of graphite and hexagonal boron nitride on solid surfaces," *Journal of Physics: Condensed Matter*, vol. 9, no. 1, pp. 1-20, 1997.

[32] X. Wang, Y. Ouyang, X. Li, H. Wang, J. Guo, and H. Dai, "Room Temperature All Semiconducting sub-10nm Graphene Nanoribbon Field-Effect Transistors," *arXiv:0803.3464v2[cond-mat.mes-hall]*, Mar. 2008.

[33] X. Li, X. Wang, L. Zhang, S. Lee, and H. Dai, "Chemically Derived, Ultrasmooth Graphene Nanoribbon Semiconductors," *Science*, vol. 319, no. 5867, pp. 1229-1232, Feb. 2008.

[34] Y. Hernandez et al., "High yield production of graphene by liquid phase exfoliation of graphite," *arXiv:0805.2850v1[cond-mat.mtrl.sci]*, May. 2008.

[35] Q. Yu, L. Jie, S. Siriponglert, H. Li, Y. P. Chen, and S.-S. Pei, "Graphene segregated on Ni surfaces and transferred to insulators," *Applied Physics Letters*, vol. 93, no. 113103, 2008.

[36] A. Reina et al., "Large-Area, Few-Layer Graphene Films on Arbitrary Substrates by Chemical Vapor Deposition," *Nano Letters*, vol. 9, no. 1, pp. 30–35, 2009.

[37] A. N. Obraztsov, "Making graphene on a large scale," *Nature Nanotechnology*, vol. 4, pp. 212–213, Apr. 2009.

[38] X. Li et al., "Large-Area Synthesis of High-Quality and Uniform Graphene Films on Copper Foils," *Science*, vol. 324, no. 5932, p. 1312, 2009.

[39] L. M. Malard, M. A. Pimenta, G. Dresselhaus, and M. S. Dresselhaus, "Raman spectroscopy in graphene," *Physics Reports*, vol. 473, no. 5-6, pp. 51-87, Apr. 2009.

[40] D. V. Badami, "Graphitization of [alpha]-Silicon Carbide," *Nature*, vol. 193, no. 4815, pp. 569-570, Feb. 1962.

[41] A. Charrier et al., "Solid-state decomposition of silicon carbide for growing ultra-thin heteroepitaxial graphite films," *Journal of Applied Physics*, vol. 92, no. 5, p. 2479, 2002.

[42] C. Berger et al., "Ultrathin Epitaxial Graphite: 2D Electron Gas Properties and a Route toward Graphene-based Nanoelectronics," *The Journal of Physical Chemistry B*, vol. 108, no. 52, pp. 19912-19916, Dec. 2004.

[43] P. N. First, W. A. de Heer, T. Seyller, C. Berger, J. A. Stroscio, and J.-S. Moon, "Epitaxial Graphenes on Silicon Carbide," *MRS Bulletin*, vol. 35, pp. 296-305, Apr. 2010.

[44] Z. H. Ni et al., "Raman spectroscopy of epitaxial graphene on a SiC substrate," *Physical Review B*, vol. 77, no. 115416, 2008.

[45] B. L. VanMil et al., "Graphene Formation on SiC Substrates," *Materials Science Forum*, vol. 615-617, pp. 211-214, 2009.

[46] K. V. Emtsev et al., "Initial stages of the graphite-SiC(0001) interface formation studied by photoelectron spectroscopy," in *6th European Conference on Silicon Carbide and Related Materials*, Newcastle upon Tyne ,UK, 2006.

[47] F. Varchon et al., "Electronic Structure of Epitaxial Graphene Layers on SiC: Effect of the Substrate," *Physical Review Letters*, vol. 99, no. 12, p. 126805, 2007.

[48] M. Sprinkle et al., "First Direct Observation of a Nearly Ideal Graphene Band Structure," *Physical Review Letters*, vol. 103, no. 22, p. 226803, Nov. 2009.

[49] D. L. Miller et al., "Observing the Quantization of Zero Mass Carriers in Graphene," *Science*, vol. 324, no. 5929, pp. 924-927, May. 2009.

[50] M. Orlita et al., "Approaching the Dirac Point in High-Mobility Multilayer Epitaxial Graphene," *Physical Review Letters*, vol. 101, no. 26, p. 267601, Dec. 2008.

[51] J. K. Hite et al., "Epitaxial Graphene Nucleation on C-Face Silicon Carbide," *Nano Letters*, vol. 11, no. 3, pp. 1190-1194, Mar. 2011.

[52] T. Ohta, N. C. Bartelt, S. Nie, K. Thürmer, and G. L. Kellogg, "Role of carbon surface diffusion on the growth of epitaxial graphene on SiC," *Physical Review B*, vol. 81, no. 12, p. 121411, Mar. 2010.

[53]   P. Sutter, "Epitaxial graphene: How silicon leaves the scene," *Nat Mater*, vol. 8, no. 3, pp. 171-172, Mar. 2009.

[54]   H. C. Schniepp et al., "Functionalized Single Graphene Sheets Derived from Splitting Graphite Oxide," *The Journal of PHysical Chemistry B*, vol. 110, pp. 8535-8539, Apr. 2006.

[55]   C. Dimitrakopoulos et al., "Wafer-scale epitaxial graphene growth on the Si-face of hexagonal SiC (0001) for high frequency transistors," *Journal of Vacuum Science & Technology B: Microelectronics and Nanometer Structures*, vol. 28, no. 5, p. 985, 2010.

[56]   A. Bostwick, T. Ohta, T. Seyller, K. Horn, and E. Rotenberg, "Quasiparticle dynamics in graphene," *Nat Phys*, vol. 3, no. 1, pp. 36-40, Jan. 2007.

[57]   T. Ohta, A. Bostwick, J. L. McChesney, T. Seyller, K. Horn, and E. Rotenberg, "Interlayer Interaction and Electronic Screening in Multilayer Graphene Investigated with Angle-Resolved Photoemission Spectroscopy," *Physical Review Letters*, vol. 98, no. 20, p. 206802, May. 2007.

[58]   G. M. Rutter et al., "Imaging the interface of epitaxial graphene with silicon carbide via scanning tunneling microscopy," *Physical Review B*, vol. 76, no. 23, p. 235416, Dec. 2007.

[59]   J. Jobst et al., "Quantum oscillations and quantum Hall effect in epitaxial graphene," *Physical Review B*, vol. 81, no. 19, p. 195434, May. 2010.

[60]   A. Tzalenchuk et al., "Towards a quantum resistance standard based on epitaxial graphene," *Nat Nano*, vol. 5, no. 3, pp. 186-189, Mar. 2010.

[61]   C. Faugeras, A. Nerriere, and M. Potemski, "Few-layer graphene on SiC, pyrolytic graphite, and graphene: A Raman scattering study," *Applied Physics Letters*, vol. 92, no. 11914, 2008.

[62]   X. Wu et al., "Half integer quantum Hall effect in high mobility single layer epitaxial graphene," *Applied Physics Letters*, vol. 95, no. 22, p. 223108, 2009.

[63]   T. Shen et al., "Observation of quantum-Hall effect in gated epitaxial graphene grown on SiC (0001)," *Applied Physics Letters*, vol. 95, no. 17, pp. 172105-3, Oct. 2009.

[64]   J. L. Tedesco et al., "Hall effect mobility of epitaxial graphene grown on silicon carbide," *Applied Physics Letters*, vol. 95, no. 12, p. 122102, 2009.

[65]   T. Ohta et al., "Morphology of graphene thin film growth on SiC(0001)," *New Journal of Physics*, vol. 10, no. 2, p. 023034, Feb. 2008.

[66]   E. Rollings et al., "Synthesis and characterization of atomically thin graphite films on a silicon carbide substrate," *Journal of Physics and Chemistry of Solids*, vol. 67, no. 9-10, pp. 2172-2177, Sep. 2006.

[67]   J. L. Tedesco et al., "Improvement of Morphology and Free Carrier Mobility through Argon-Assisted Growth of Epitaxial Graphene on Silicon Carbide," in *ECS Transactions*, San Francisco, CA, 2009, pp. 137-150.

[68]   K. V. Emtsev et al., "Towards wafer-size graphene layers by atmospheric pressure graphitization of silicon carbide," *Nat Mater*, vol. 8, no. 3, pp. 203-207, Mar. 2009.

[69]   N. Ferralis, R. Maboudian, and C. Carraro, "Evidence of Structural Strain in Epitaxial Graphene Layers on 6H-SiC(0001)," *Physical Review Letters*, vol. 101, p. 156801, 2008.

[70] T. Filleter, K. V. Emtsev, T. Seyller, and R. Bennewitz, "Local work function measurements of epitaxial graphene," *Applied Physics Letters*, vol. 93, no. 13, p. 133117, 2008.

[71] K. S. Novoselov et al., "Two-dimensional gas of massless Dirac fermions in graphene," *Nature*, vol. 438, no. 7065, pp. 197-200, Nov. 2005.

[72] D. K. Gaskill, M. S. Fuhrer, and A. E. Curtin, "private communications 2011." .

[73] N. J. Lee et al., "The interlayer screening effect of graphene sheets investigated by Kelvin probe force microscopy," *Applied Physics Letters*, vol. 95, no. 22, p. 222107, 2009.

[74] Y.-J. Yu, Y. Zhao, S. Ryu, L. E. Brus, K. S. Kim, and P. Kim, "Tuning the Graphene Work Function by Electric Field Effect," *Nano Letters*, vol. 9, no. 10, pp. 3430-3434, Oct. 2009.

[75] E. McCann, D. S. L. Abergel, and V. I. Fal'ko, "The low energy electronic band structure of bilayer graphene," *The European Physical Journal - Special Topics*, vol. 148, no. 1, pp. 91-103, 2007.

[76] S. Sonde et al., "Electrical properties of the graphene/ 4H-SiC (0001) interface probed by scanning current spectroscopy," *Physical Review B*, vol. 80, no. 24, p. 241406, Dec. 2009.

[77] T. J. B. M. Janssen et al., "Anomalously strong pinning of the filling factor nu =2 in epitaxial graphene," *Physical Review B*, vol. 83, no. 23, p. 233402, Jun. 2011.

[78] S. Adam and M. S. Fuhrer, "private communications 2011." .

[79] S. Das Sarma, S. Adam, E. H. Hwang, and E. Rossi, "Electronic transport in two-dimensional graphene," *Reviews of Modern Physics*, vol. 83, no. 2, p. 407, May. 2011.

[80] E. H. Hwang and S. Das Sarma, "Dielectric function, screening, and plasmons in two-dimensional graphene," *Physical Review B*, vol. 75, no. 20, p. 205418, May. 2007.

[81] G. M. Rutter, J. N. Crain, N. P. Guisinger, T. Li, P. N. First, and J. A. Stroscio, "Scattering and Interference in Epitaxial Graphene," *Science*, vol. 317, no. 5835, pp. 219-222, Jul. 2007.

[82] S. Kopylov, A. Tzalenchuk, S. Kubatkin, and V. I. Fal'ko, "Charge transfer between epitaxial graphene and silicon carbide," *Applied Physics Letters*, vol. 97, no. 11, p. 112109, 2010.

[83] J. Yan and M. S. Fuhrer, "Correlated charged impurity scattering in graphene," *arXiv:1106.4835 [cond-mat.mes-hall]*, Jun. 2011.

[84] Q. Li, E. H. Hwang, E. Rossi, and S. D. Sarma, "Theory of 2D transport in graphene for correlated disorder," *arXiv:1104.0667 [cond-mat.mes-hall]*, Apr. 2011.

[85] A. L. Walter et al., "Effective screening and the plasmaron bands in Graphene," *arXiV:1107.4398 [cond-mat.str-el]*, Jul. 2011.

[86] A. Luican, G. Li, and E. Y. Andrei, "Quantized Landau level spectrum and its density dependence in graphene," *Physical Review B*, vol. 83, no. 4, p. 041405, Jan. 2011.